LEVEL

(42)

AFGL-TR-79-0001

A SOURCE MODEL FOR THE 1975 POCATELLO VALLEY EARTHQUAKE

S. M. DAY
T. C. BACHE
T. G. BARKER
J. T. CHERRY

SYSTEMS, SCIENCE AND SOFTWARE
P. O. BOX 1620
LA JOLLA, CALIFORNIA 92038

DDC

MAY 15 1979

C

SCIENTIFIC REPORT NO. 1

28 DECEMBER 1978

APPROVED FOR PUBLIC RELEASE; DISTRIBUTION UNLIMITED.

AIR FORCE GEOPHYSICS LABORATORY
AIR FORCE SYSTEMS COMMAND
UNITED STATES AIR FORCE
HANSCOM AFB, MASSACHUSETTS 01731

79 05 14 004

SECURITY CLASSIFICATION OF THIS PAGE (When Data Entered)

REPORT DOCUMENTATION PAGE	READ INSTRUCTIONS BEFORE COMPLETING FORM

1. REPORT NUMBER	2. GOVT ACCESSION NO.	3. RECIPIENT'S CATALOG NUMBER
AFGL-TR-79-0001		

4. TITLE (and Subtitle)	5. TYPE OF REPORT & PERIOD COVERED
A SOURCE MODEL FOR THE 1975 POCATELLO VALLEY EARTHQUAKE	SCIENTIFIC
	6. PERFORMING ORG. REPORT NUMBER
	SSS-R-79-3893

7. AUTHOR(s)	8. CONTRACT OR GRANT NUMBER(s)
S. M. Day, T. C. Bache, T. G. Barker and J. T. Cherry	F19628-77-C-0004

9. PERFORMING ORGANIZATION NAME AND ADDRESS	10. PROGRAM ELEMENT, PROJECT, TASK AREA & WORK UNIT NUMBERS
Systems, Science and Software, P.O. Box 1620 La Jolla, California 92038	61102F 2309G1AC

11. CONTROLLING OFFICE NAME AND ADDRESS	12. REPORT DATE
Air Force Geophysics Laboratory Hanscom AFB, Massachusetts 01731 Monitor/Henry Ossing/LWH	8 December 1978
	13. NUMBER OF PAGES
	109

14. MONITORING AGENCY NAME & ADDRESS(if different from Controlling Office)	15. SECURITY CLASS. (of this report)
	UNCLASSIFIED
	15a. DECLASSIFICATION/DOWNGRADING SCHEDULE

16. DISTRIBUTION STATEMENT (of this Report)

Approved for public release; distribution unlimited

17. DISTRIBUTION STATEMENT (of the abstract entered in Block 20, if different from Report)

18. SUPPLEMENTARY NOTES

19. KEY WORDS (Continue on reverse side if necessary and identify by block number)

Earthquakes
Synthetic Seismograms
Seismic Source Theory

20. ABSTRACT (Continue on reverse side if necessary and identify by block number)

A source model is determined for the 1975 Pocatello Valley earthquake by fitting synthetic seismograms to the observations of long and short period P waves. The focal plane is constrained by a focal mechanism solution from P wave first motion observations and by the aftershock locations. The event is characterized by normal faulting on a plane dipping 39° to the west with a large left-lateral strike-slip component.

(continued)

DD FORM 1473 EDITION OF 1 NOV 65 IS OBSOLETE

4

Con't

Two source models were used for the synthetic seismogram computations. Parameter variations to fit the observations were done with the analytical model of Archambeau and Minster. Two three-dimensional finite difference simulations of earthquake faulting were done on the ILLIAC IV computer. Comparing the results to the analytical model, we interpret the derived parameters in terms of the physics of faulting. We conclude that variable rupture velocity/variable stress drop effects are required to simultaneously fit the long and short period data. Source directivity effects are important with unilateral rupture toward the free surface being required to fit the data.

One finite difference calculation allowed plastic yielding near the fault plane while the other was for a linearly elastic medium. The main effect of the plasticity was less abrupt stopping of the rupture which reduces the radiation of high frequency energy. Plastic flow outside the fault plane increases the seismic moment.

ACCESSION for

NTIS	White Section	✓
DDC	Buff Section	☐
UNANNOUNCED		☐
JUSTIFICATION		

BY
DISTRIBUTION/AVAILABILITY CODES

Dist.	SPECIAL
A	

TABLE OF CONTENTS

TABLE OF CONTENTS
(continued)

LIST OF ILLUSTRATIONS

LIST OF ILLUSTRATIONS
(continued)

LIST OF TABLES

I. INTRODUCTION AND SUMMARY

1.1 INTRODUCTION

The objectives of this contract may be summarized as follows:

1. Determine a source model for the 1975 Pocatello Valley earthquake.

2. Compute the likely ground motion at the Wing V Minuteman site due to the Pocatello Valley event and determine those features of the source or propagation path that may have caused this ground motion to be peculiar or untypical of western U. S. earthquakes.

3. Using synthetic seismograms for typical western U. S. earthquakes and earth structure, determine the important characteristics of the ground motions at regional distances within 200 km of these events.

4. Provide initial estimates of the similarities and differences between the strong ground motions generated by earthquakes and large surface nuclear explosions.

In this report we will be concerned with the first objective and that portion of the second objective which compares the source model of the Pocatello Valley earthquake with other western U. S. earthquakes. A companion report (Rodi, et al., 1979) addresses the remaining objectives with special emphasis on the ground motion at Wing V from both the Pocatello Valley earthquake and the 1975 Yellowstone earthquake.

A variety of techniques were used in order to carefully delineate the source mechanism for the initial faulting of the

1975 Pocatello Valley earthquake. The data include after-
shock locations and observations of long period and short
period P waves. We use analytical models and a three-dimen-
sional finite difference earthquake model to compute synthetic
seismograms to match these data. We find that the Pocatello
Valley earthquake is characterized by normal faulting on a
plane dipping 39° to the west with a large left-lateral
strike slip component. This event turns out to be quite
similar in most respects to the 1971 San Fernando earthquake
in Southern California.

1.2   SUMMARY

The technical discussion in this report is divided in-
to three sections. In Section II we use analytical models to
infer a fault model for the Pocatello Valley earthquake. As
part of this contract, ILLIAC IV computer time was provided
in order that a three-dimensional finite difference model of
faulting could be exercised. Section III is devoted to a dis-
cussion of that work and its implications for the physics of
earthquake faulting. In Section IV the results of the analy-
tical modeling of the Pocatello Valley earthquake and the
finite difference calculations are compared and combined to
complete our source model for the Pocatello Valley event.
Important conclusions about the nature of earthquake fault-
ing in general are also drawn.

The techniques applied in Section II to infer the
source parameters of the Pocatello Valley earthquake include
the following:

- A focal mechanisms solution is constructed from
  observations of P wave first motion.

- Results from a study of the aftershock sequence
  by Arabasz, et al. (1975b) were examined for
  indications of the fault plane orientation.

2

- Using the Archambeau/Minster earthquake source model (Archambeau, 1968; Minster, 1973) and methods for computing synthetic seismograms in layered earth models (Bache and Harkrider, 1976), synthetic seismograms were computed for comparison to long and short period P wave observations.

- The model parameters were varied to obtain estimates for the source dimension, rupture velocity and stress drop as well as confirming the orientation. The main diagnostic features of the observations are the waveform and frequency content of the P and pP phases, their time delay and their relative amplitudes.

An important conclusion of Section III is that no uniform stress drop, uniform rupture velocity model can simultaneously fit the long and short period data. If the long period level (moment) is large enough, the synthetic short period records are much too large -- by a factor of 3 to 5. We were led to the same conclusion in an earlier study of the 1971 San Fernando earthquake (Bache and Barker, 1978).

To improve the fit to the data over a broad frequency range, variable stress drop and variable rupture velocity effects were introduced into the analytical source model. This is done in a rather ad hoc fashion and the results are far from unique. However, we claim that they are qualitatively correct. The new source model gives a reasonably good fit to the long and short period data for the first 5 to 8 seconds of faulting.

The approach in Section III is entirely different. In this section our main attention is to the physics of earthquake faulting for events like the Pocatello Valley earthquake. Two three-dimensional finite difference calculations were done to simulate faulting in a uniform whole space. The calculations were done on the ILLIAC IV computer using the TRES computer program (Cherry, 1977). The first calculation was for a linearly elastic medium while the second allowed

3

elastic-plastic material behavior near the fault plane.
Using the method of Bache and Harkrider (1976), the results
of both calculations were expressed in a form compatible with
the programs for computing synthetic seismograms. The far-
field displacements and displacement spectra were studied.
The accuracy of the finite difference method was verified
by comparing the results to analytical and numerical solutions
of crack problems. We find that main effect of the simple
plasticity admitted to the second calculation was less
abrupt stopping of the rupture at the edge of the fault plane.
This reduces the radiation of high frequency energy. Plastic
flow outside the fault plane increases the seismic moment.

In Section II we develop a model for the Pocatello
Valley earthquake in terms of an analytical model for which
parameter variations are convenient. However, interpreta-
tion of the derived parameters in terms of earthquake physics
is difficult for any analytical model and is especially so
for the Archambeau/Minster model which is cast in terms of
an unrealistic spherical geometry. On the other hand, the
ILLIAC calculations of Section III are close to the most
detailed and realistic models of earthquake faulting that
are currently available. Taken together, the two can be
used to define the source with considerable confidence. This
is our objective in Section IV.

Comparison of the finite difference and analytical
models by means of synthetic seismograms appropriate for
stations observing the Pocatello Valley event support our
conclusions about earthquake faulting reached with the
analytical models. That is, we cannot simultaneously match
the long and short period data with a single rupture veloc-
ity/single stress drop source model.

Another interesting facet of the comparison is that
source directivity effects can be seen in that data. The

4

finite difference simulations are bilateral and give poorer
agreement with the short period data than the unilateral
analytical model.

Finally, we conclude that the variable rupture veloc-
ity analytical model derived in Section II is a good model
for the initial few seconds of rupture of the Pocatello
Vally earthquake. The long and short period teleseismic
records show that the source is more complex and has longer
duration. The later faulting is, however, considerably
smaller as a source of seismic waves so our Model II should
give a reasonable estimate for the peak ground motions at
the regional ranges of ultimate interest.

1.3   CONTRIBUTING SCIENTISTS

The authors of this report, Drs. S. M. Day, T. C.
Bache, T. G. Barker and J. T. Cherry, are responsible for
all material presented. A number of other Systems, Science
and Software (S^3) scientists contributed to the work on which
this report is based. The principal scientists for the work
described in each section of this report are listed below
along with others who made substantial contributions.

SECTION II - AN ANALYTICAL SOURCE MODEL FOR THE POCATELLO
             VALLEY EARTHQUAKE

    Principal Scientists: T. B. Barker and T. C. Bache
    Contributing Scientists: D. G. Lambert and B. F. Mason

SECTION III - FINITE DIFFERENCE MODELING OF EARTHQUAKE
              FAULTING

    Principal Scientists: S. M. Day and J. T. Cherry
    Contributing Scientists: J. F. Masso and E. J. Halda

SECTION IV - COMPARISON OF ANALYTICAL AND FINITE DIFFERENCE
             MODELS

    Principal Scientist: T. C. Bache
    Contributing Scientists: S. M. Day and B. F. Mason

The ILLIAC IV calculations were carried out with the assistance of the Institute of Advanced Computation and this is gratefully acknowledged in Section V.

6

II. AN ANALYTICAL SOURCE MODEL FOR THE POCATELLO VALLEY EARTHQUAKE

2.1 INTRODUCTION

The March 28, 1975 Pocatello Valley earthquake was an m_b 6.1 event occurring near the Idaho-Utah border. Our procedure for deducing the ground motions of interest involves two steps. First, we use available data to infer a detailed source model for the event. Then we use this source model together with estimates for the earth structure to theoretically compute the ground motions of interest. This section describes our first step; inference of the source from analytical models.

Previous work on the Pocatello Valley event has included a thorough study of the aftershock sequence (Arabasz, et al., 1975b). Fault plane solutions were constructed by A. Rogers (USGS, private communication) from the first motion P wave observations and by Battis and Hill (1977) from far-field surface wave spectra. We take advantage of this work in our more detailed study.

The details of our source model are largely determined by a comparison of synthetic and observed short period seismograms at teleseismic distances; that is, at ranges greater than 30'. These data constrain the source in the frequency range from 0.5 to 2.0 Hz. Of course, the accuracy with which we can constrain the source in this frequency band depends on our ability to account for path effects. Unfortunately, there are only a few good teleseismic recordings of this event and this increases the range of uncertainty.

The source model we use for our synthetic seismogram computations is the analytical relaxation model of Archambeau (1968) and Minster (1973). This model has previously been used to model the 1971 San Fernando earthquake (Bache and

7

Barker, 1978). The analytical form is convenient for varying the source parameters. In Section III we will describe a detailed finite difference fault model for earthquake faulting that reproduces the fault physics with much greater accuracy. Then in Section IV we will compare the results of the finite difference calculations with our analytical model and discuss the implications for the Pocatello Valley event and other western U.S. earthquakes.

2.2 FOCAL MECHANISM DETERMINATION FROM P WAVE POLARITY

Within weeks of the event, Rogers (1975) determined a focal mechanism solution from immediately available P wave first-motion readings. Another solution was obtained by Battis and Hill (1977) who used surface wave spectra to estimate the fault plane orientation. Arabasz, et al. (1975b) reported on a detailed study of the aftershock sequence and used this information to deduce the fault parameters. These three solutions are summarized in Table 1.

Looking at the previous focal mechanism solutions and how they were obtained, we decided to verify them by repeating the P wave first-motion solution, adding data unavailable to Rogers. For this purpose, first-motion readings were obtained from the U.S. Geological Survey (USGS) (Rogers, private communication) and from the California Institute of Technology (Stewart, private communication), who also computed the lower hemisphere location for the ray to each station. A summary of station location, first motion, amplitude and magnitude data is given in Table 2.

The P wave polarity data are plotted in a lower hemisphere display in Figure 1. A rather well-constrained focal mechanism is determined from the data. The orientation of the two orthogonal best-fitting solutions is indicated on the figure. One of these solutions is for normal faulting on a

8

TABLE 1

SOURCE PARAMETERS FOR THE POCATELLO EARTHQUAKE FROM PREVIOUS STUDIES

Source of Data	Strike (Deg.)	Dip (Deg.)	Slip (Deg.)	M_o (dyne-cm)	$\Delta\sigma$ (bars)	Depth (km)
Arabasz, et al. (1975a)	N10°E		−90	1×10^{25}	4-5	5.0
Battis and Hill (1977), Surface Waves	N15°E	60°E	−90	7.21×10^{24}		5.0
Rodgers (1977), Body Waves	N13°E	45°E	−90			

TABLE 2

POCATELLO EARTHQUAKE, MARCH 28, 1975

Station Code	Epi-Sta Azimuth	Distance	Instrument	Phase	First Motion	Period (Sec.)	Maximum A/T	m_b	M_s	Marshall and Basham, M_s
LON	308°	8.1°	SPZ	Pn	+	1.1	279.0	6.45		
			LPZ	Pn	+					
			LPZ	LR		8.0	14,920		5.80	5.42
COR	292°	8.2°	SPZ	Pn	(+)	1.1	158.0	6.20		
			LPZ	Pn	+	(3.0)	(41,604)			
				Sn	+	(5.5)	(15,084)			
				LR	-	8.0	16,285		5.85	5.47
			LPN	Sn		2.8	31,897			
				LQ		10.0	11,918			
BKS	244°	8.5°	SPZ	Pn	(+)	1.0	236.6	6.37		
			LPZ	Pn	+	(5.5)	(2,838)			
				Sn	+	(5.8)	(2,598)			
ALQ	144°	8.6°	SPZ	Pn	(-)	(0.8)	(41.9)	5.62		
			LPZ	Pn	+					
EDM	356°	11.2°	LPZ	P	-	5.0	4,750			
			LRE	S	+	4.0	6,985			
				S	+	7.0	2,605			
PHC	315°	13.5°	SPZ	P	+	0.8	155.0	5.99		
			LPZ	P	+	6.0	6,328			
FFC	269°	14.7°	SPZ	P	-	(0.8)	(318.0)	6.00		
			LPZ	P	-	7.7	732.6			
JCT	134°	15.4°	SPZ	P	+	1.0	433.0	5.94		
			LPZ	P	+	9.5	4,738			
				S	+	(13.0)	(953.7)			
				LR		(12.0)	(4,074)		5.70	5.54
FCC	27°	20.0°	LPZ	P	-	6.0	4,043			
			LPN	S	+	12.0	1,200			
			LRN	S	-	12.0	520.0			
			LRE	S	+	12.0	484.0			

TABLE 2

POCATELLO EARTHQUAKE, MARCH 28, 1975 (continued)

Station Code	Epi-Sta Azimuth	Distance	Instrument	Phase	First Motion	Period (Sec.)	Maximum A/T	m_b	M_s	Marshall and Basham, N_s
BLA	90°	25.1°	SPZ	P	(+)	(4.0)	(3,289)			
			LPZ	P	+	(8.0)	(4,945)			
				S	+	11.0	6,044			
			LPN	LR	+	5.5	10,733		6.23	5.79
				IQ		9.0	39,517			
YKC	358°	26.5°	SPZ	P	−	0.8	275.0	5.89		
			LPZ	P	−	8.8	2,749			
				S	+	13.5	1,497			
			LPE	LR	−	(12.0)	(4,493)		6.11	5.79
				S	−	7.0	5,292			
MHT	70°	28.2°	LPZ	P	(+)	(14.0)	(158.7)			
				S	(+)	(10.5)	(1,940)		6.22	5.83
				LR		(11.7)	(4,893)			
INK	344°	28.6°	LPZ	P	−	7.6	671.0			
				S	−	12.6	967.0			
			LPN	S	+	(13.0)	(960.0)			
			LPE	S	−	(13.0)	(968.0)			
SFA	66°	30.3°	LPZ	P	+	(5.9)	(1,337)			
				S	−	10.0	984.0			
			LPN	LR	(−)	13.7	2,341		5.95	5.76
				IQ	(|)	11.7	391.0			
			LPE	S		11.7	2,888			
						17.5	726.0			
FBC	29°	31.4°	LPZ	P	−	6.0	294.0			
			LPE	LQ		(17.0)	(992.0)			
RES	9°	33.4°	SPZ	P	−	1.3	172.3	5.94		
			LPZ	P	−	6.5	821.0			
MBC	357°	34.4°	LPZ	P	−	6.0	2,437			
			LPN	S	−	6.0	2,462			
			LPE	S	−					

11

TABLE 2

POCATELLO EARTHQUAKE, MARCH 28, 1975 (continued)

| Station Code	Epi-Sta Azimuth	Distance	Instrument	Phase	First Motion	Period (Sec.)	Maximum A/T	m_b	M_s	Marshall and Basham, M_s
STJ	61°	42.1°	SPZ	P	(-)	(2.0)	(110.0)	5.54		
			LPZ	P	(-)	(11.0)	(282.0)		6.45	5.91
			LPN	LR	(+)	(11.0)	(4,260)			
				S		12.0	3,693			
			LPE	LQ	(-)					
				S						
ALE	8°	43.5°	SPZ	P	-	(1.4)	(56.7)	5.25		
			LPZ	P	-	6.0	815.0		6.43	5.77
				LR		10.0	3,920			
			LPE	LQ		12.0	1,704			
DAG	17°	50.3°	SPZ	P	(-)	(1.4)	(323.0)	6.21		
KTG	26°	52.1°	SPZ	P	(-)	1.4	359.0	6.26		
			LPZ	P	-				5.96	5.78
			LPZ	LR		14.5	981.9			
KBS	11°	55.0°	SPZ	P	(+)	(1.4)	(259.5)	6.21		
			LPZ	P	-				5.79	5.55
			LPZ	LR		14.0	608.0			
			LPE	LQ		19.0	545.1			
BOG	133°	56.6°	SPZ	P	(+)	1.4	445.0	6.45		
			LPZ	(S)	(+)				6.08	6.69
				LR		27.0	1,120			
			LPE	LQ		33.0	1,346			
KEV	15°	64.6°	SPZ	P	(-)	(1.4)	(122.3)	6.09		
			LPZ	P	-				5.60	5.60
			LPZ	LR		(16.0)	(298.4)			
KON	29°	68.1°	SPZ	P	(-)	(1.4)	(122.3)	6.09		
			LPZ	P	-				5.93	5.76
			LPZ	LR		14.5	586.2			
NUR	21°	72.0°	SPZ	P	(-)	Gain Unknown				
			LPZ	P	-				5.62	5.39
			LPZ	LR		14.0	261.5			

TABLE 2

POCATELLO EARTHQUAKE, MARCH 28, 1975 (Concluded)

Station Code	Epi-Sta Azimuth	Distance	Instrument	Phase	First Motion	Period (Sec.)	Maximum A/T	m_b	M_s	Marshall and Basham, M_s
PTO	50°	72.4°	SPZ	P	(-)	(1.4)	(201.4)	6.20	5.72	5.84
			LPZ	LR		19.0	324.0			
			LPN	LQ		19.0	221.1			
SPU	35°	76.0°	SPZ	P	(-)	(1.4)	(79.1)	5.80		
DAV	280°	118.8°	LPZ	LR		20.0	170.5		5.80	
BUL	69°	139.7°	SPZ	PKP	(+)	(1.0)	(9.8)		5.99	
			LPZ	LR		21.0	203.6			
								6.05	5.96	5.74
								n=19	n=18	n=16
								σ=±0.33	σ=±0.26	σ=±0.32

+   Compressional first motion.   For Z Components

-   Dilitational first motion.

( ) Questionable values.

+   First motion of phase "up" for N and E horizontal components.

-   First motion of phase "down" for N and E horizontal components.

A/T Amplitude in mµ/sec.

13
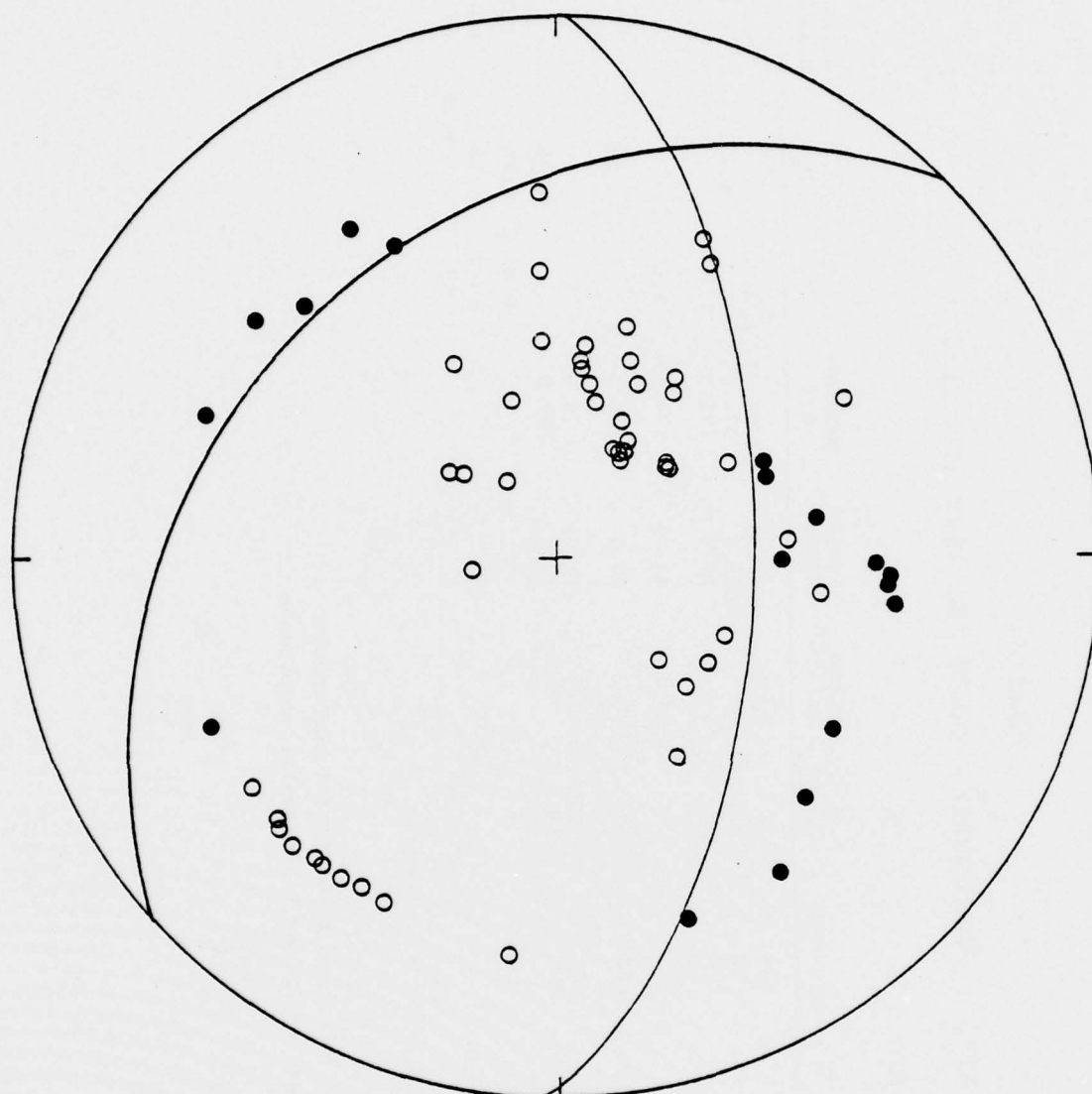
O   DILITATIONAL FIRST MOTION

●   COMPRESSIONAL FIRST MOTION

Solution 1	Solution 2
Strike = N1°E	Strike = N 45°E
Dip = 60°E	Dip = 39°W
Slip = Up 64 °N	Slip = Up 53 °N
Normal Faulting	Normal Faulting

Figure 1.   The lower hemisphere fault plane solution is shown
             for the Pocatello Valley, Idaho earthquake of
             28 March 1975.

14

fault plane dipping 60° to the east with some right-lateral
strike-slip component. The second solution is for normal
faulting on a plane dipping 39° to the west with a large
left-lateral strike-slip component. Choice between the two
must be based upon other information.

2.3   GEOLOGICAL EVIDENCE

Arabasz, et al. (1975b) reported on a detailed study
of the aftershocks associated with this event. More than
400 aftershocks were accurately located and are mapped in
Figures 2 through 5. The focal mechanisms are predominantly
for normal faulting with some strike-slip component. The
depth distribution of the aftershocks is indicated in the
cross-sections plotted in Figures 3 through 5.

The conventional wisdom in seismology is that the
aftershock distribution can be used to indicate the location
of the fault plane. We have plotted the main shock hypo-
center in Figures 3 and 4 using the epicenter location of
Arabasz, et al. (1975b) from Figure 2. The depth of 8.7 km
was deduced in the synthetic seismogram studies to be des-
cribed in later sections. It is not greatly different from
the preliminary depth determination of 5.0 km given by
Arab sz, et al. (1975a). There may be errors in both the
depth and epicenter determinations, but the aftershock dis-
tributions on Figures 2-4 certainly support the chosen
locations. Section 2 in Figure 2 turns out to be exactly
aligned with the westerly dipping focal mechanism solution
we have called Solution 2 in Figure 1. The depth distribution
of aftershocks in this section (Figure 4) is remarkably con-
sistent with the 39°W dip of the focal mechanism solution.
The aftershock distribution can also be used to help define
the fault dimensions.

15
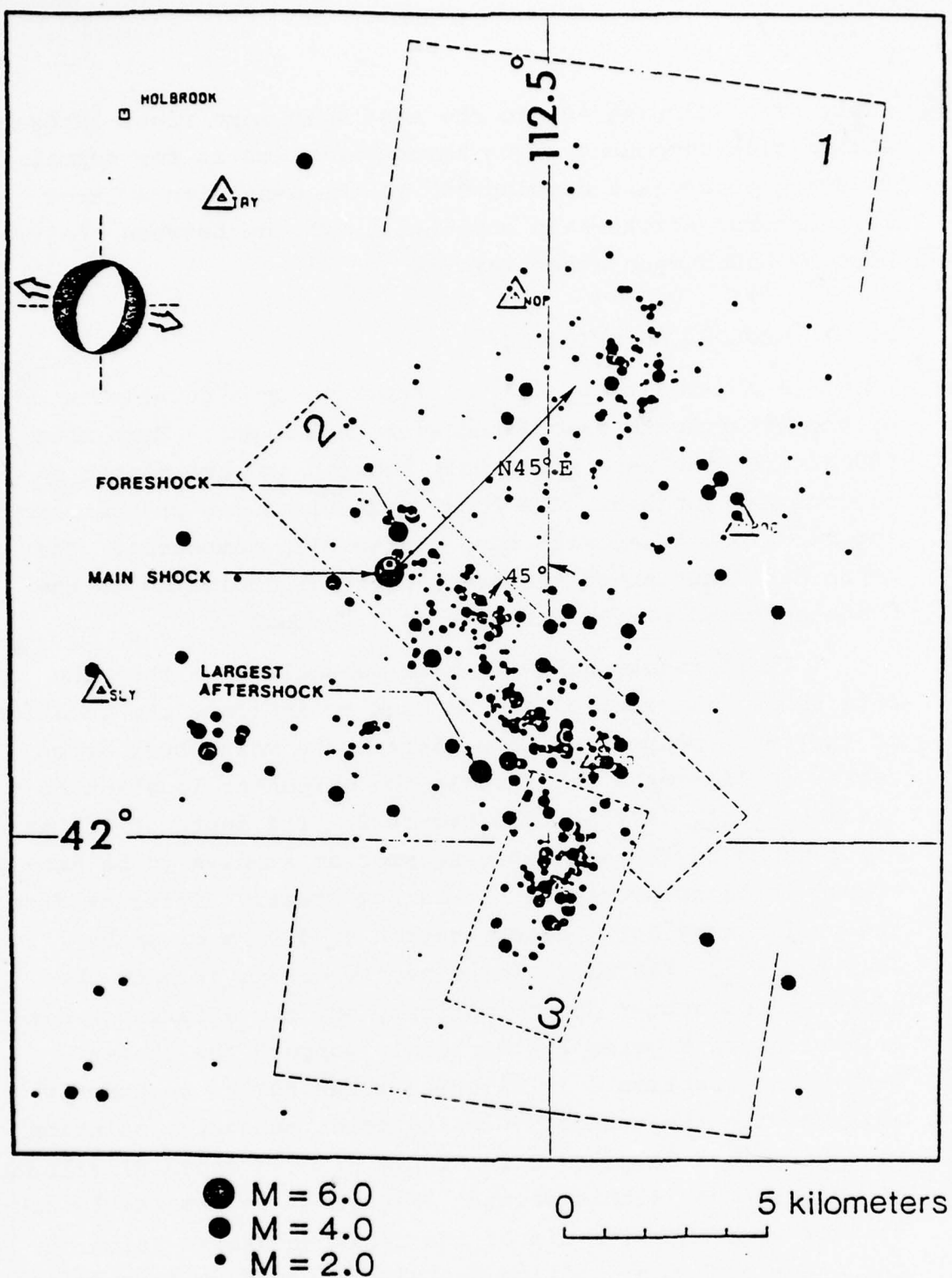
Figure 2. The locations are plotted for the Pocatello Valley earthquake and more than 400 fore and aftershocks (reproduced from Arabasz, et al., 1975b). The strike for Solution 2 from Figure 1 is indicated.

16
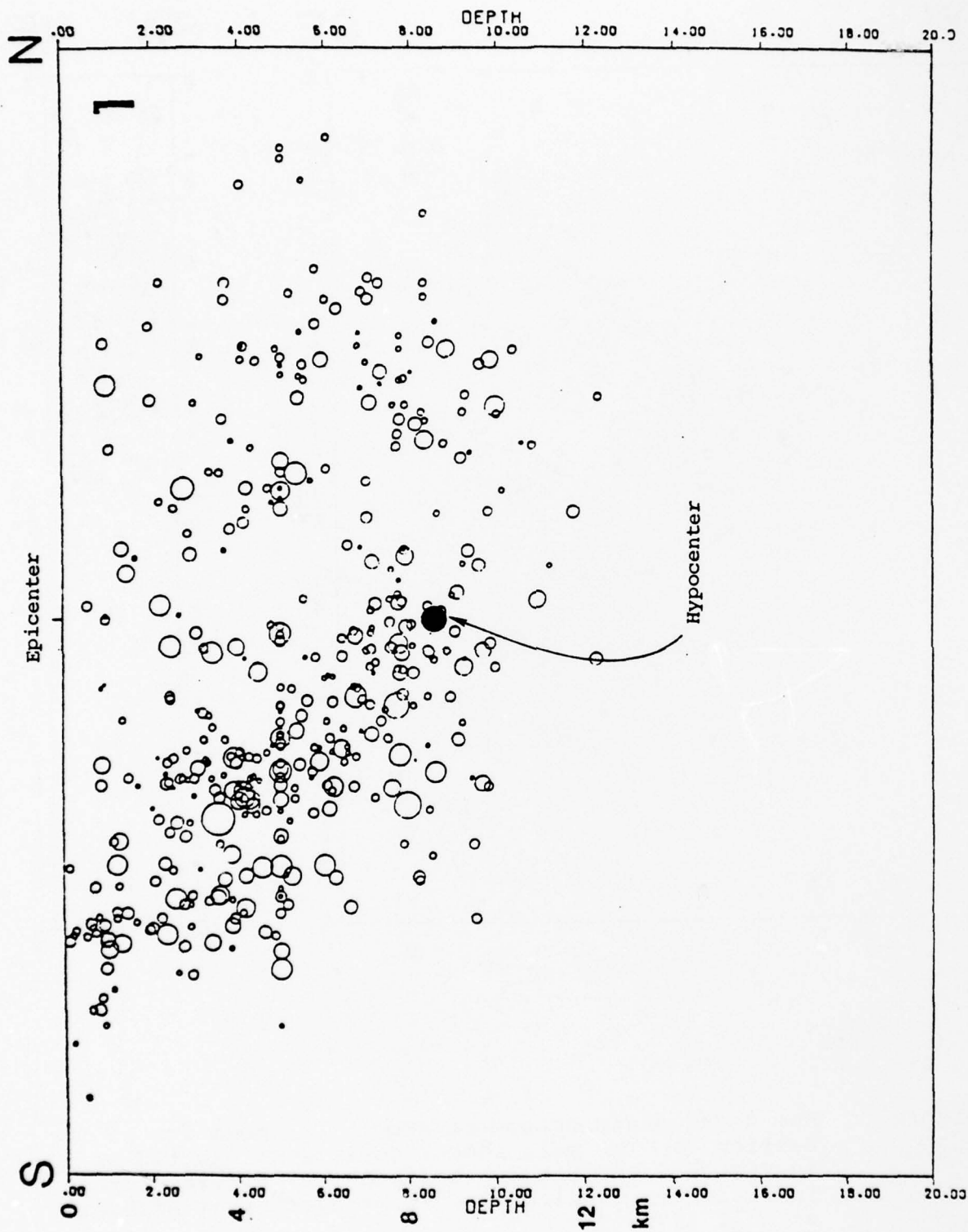
Figure 3. The distribution of earthquake hypocenters is plotted versus depth for the section denoted as 1 in Figure 2. The main shock epicenter is scaled from Figure 2. The depth is that inferred in our synthetic seismogram studies (reproduced from Arabasz, et al., 1975b).
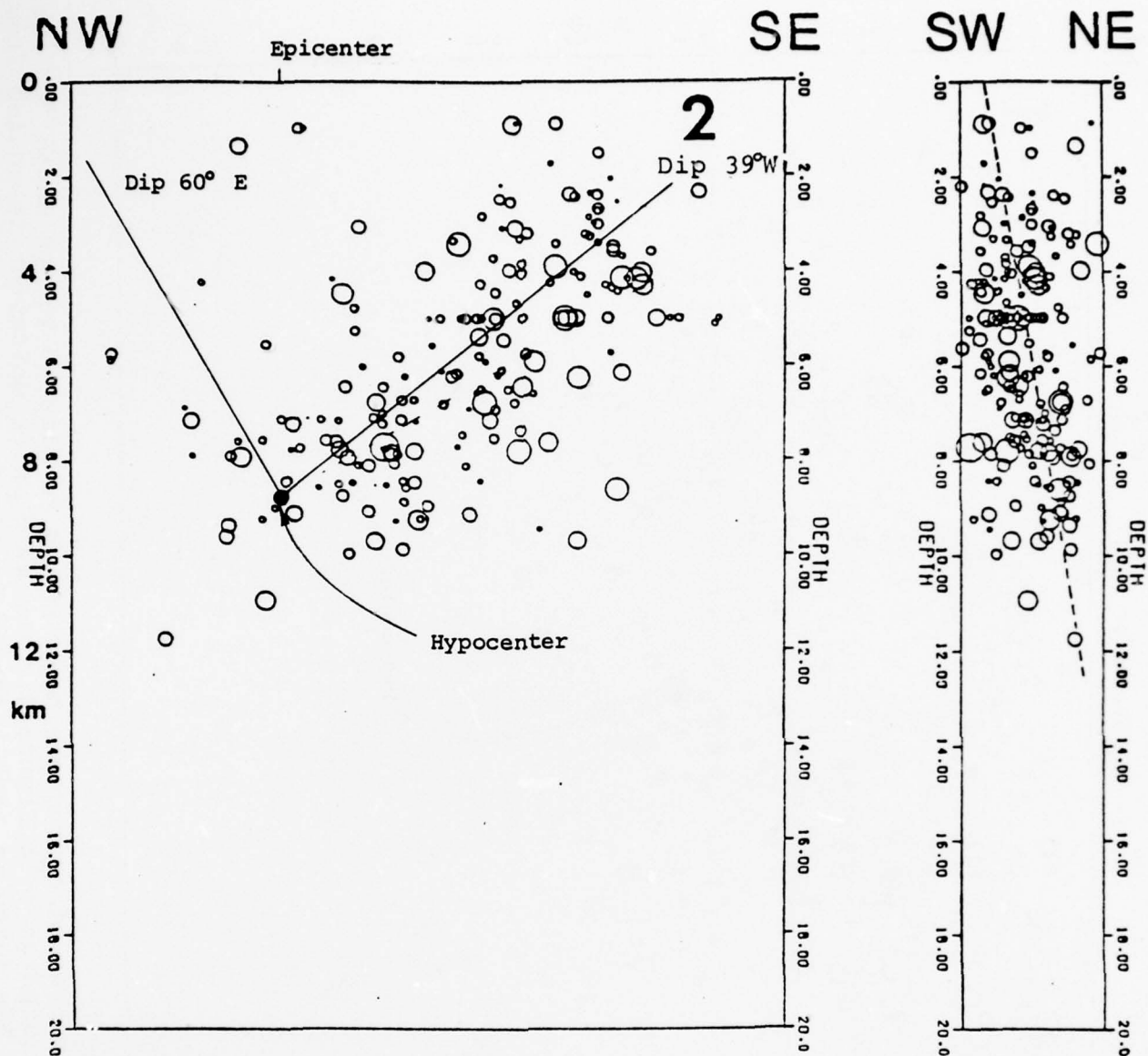
Figure 4.   The depth distribution of events is shown for
Section 2.   The main shock location is plotted as
in Figure 3 and the dip solutions of Figure 1 are
indicated by a solid line (reproduced from Arabasz,
et al., 1975b).
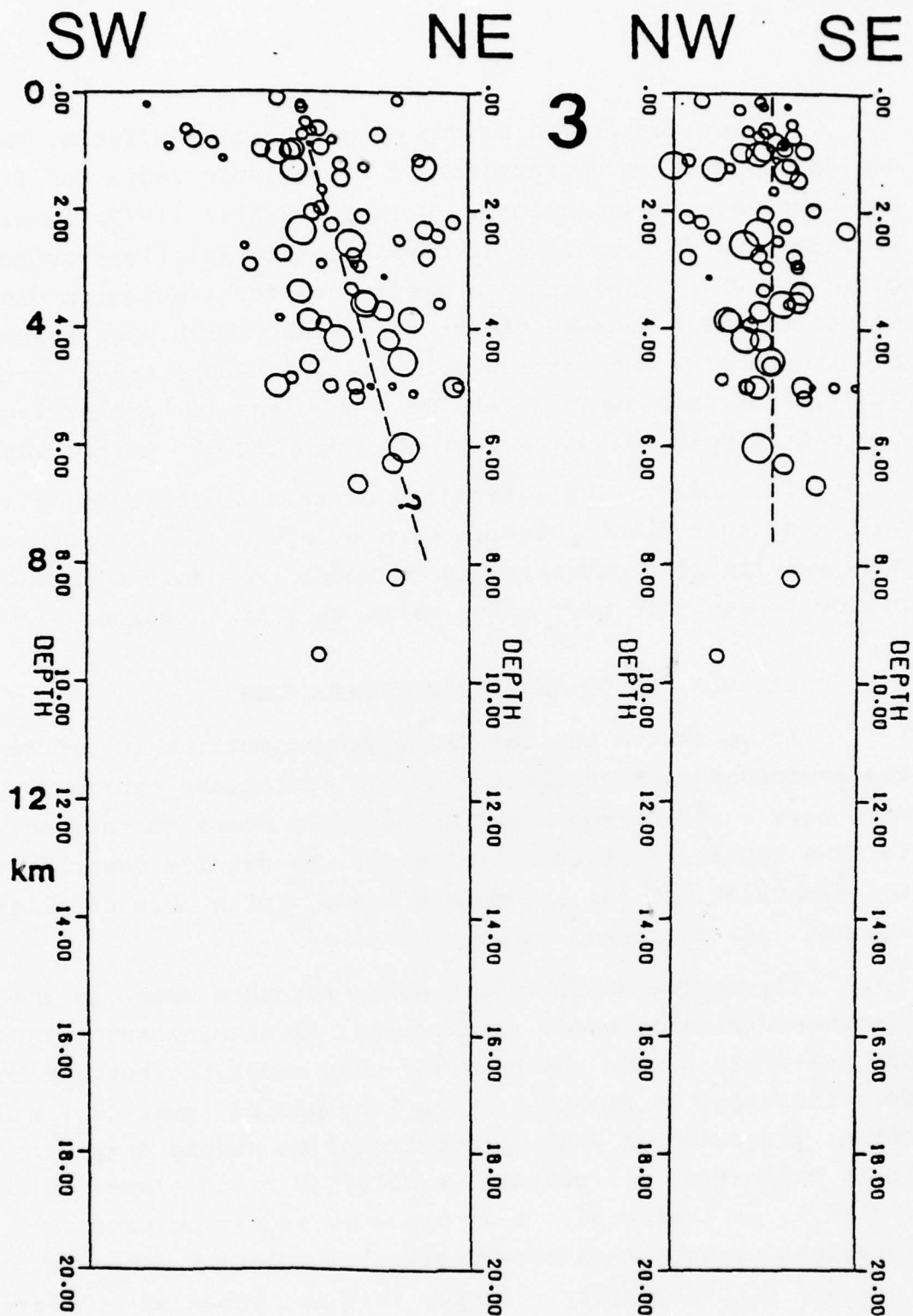
Figure 5.   The depth distribution of events is shown for
            Section 3 (reproduced from Arabasz, <u>et al</u>.,
            1975b).

Except for finite source directionality effects, there are, of course, no differences in the seismic radiation from the complementary solutions. Battis and Hill (1977) inverted surface wave spectra to find complementary solutions quite close to ours. They state a preference for a solution dipping 60° to the east because of its consistency with past seismicity in the area and particularly the 1962 Cache Creek earthquake. But this seems a very weak argument for preferring the east dipping solution over that dipping 39° to the west.

In summary, the aftershock distributions strongly support the fault plane solution with a 39°W dip. We will later show results from our attempts to model the short and long period teleseismic body waves using this orientation.

2.4   CALCULATION OF SYNTHETIC SEISMOGRAMS

If we are to use far-field ground motions to deduce the important characteristics of the earthquake source, we must have a source model and an accurate means for accounting for the source-receiver travel path. We briefly describe the the numerical methods and models used. For a more detailed account, see Bache and Barker (1978).

The source model we are using for this event is the Archambeau/Minster model (Archambeau, 1968; Minster, 1973). The far-field P wave spectrum for this model has roughly the form indicated in Figure 6. The long period level ($\hat{u}_o$) and corner frequency (f_c) are proportional to stress drop ($\Delta\sigma$), fault dimension (L), rupture velocity (V_r) and P wave velocity (α_s), as indicated. They are also radiation pattern dependent, though much more weakly. The source model also includes directionality effects; that is, enhanced high-frequency energy in the direction of rupture propagation.

20

Amplitude

$$\hat{u}_0 = \Delta\sigma \cdot L^3$$

$$f_c \propto \left(\frac{V_R \, \alpha_s^2}{L^3}\right)^{1/3}$$

$$\omega^{-\gamma}, \; \gamma \geq 3$$
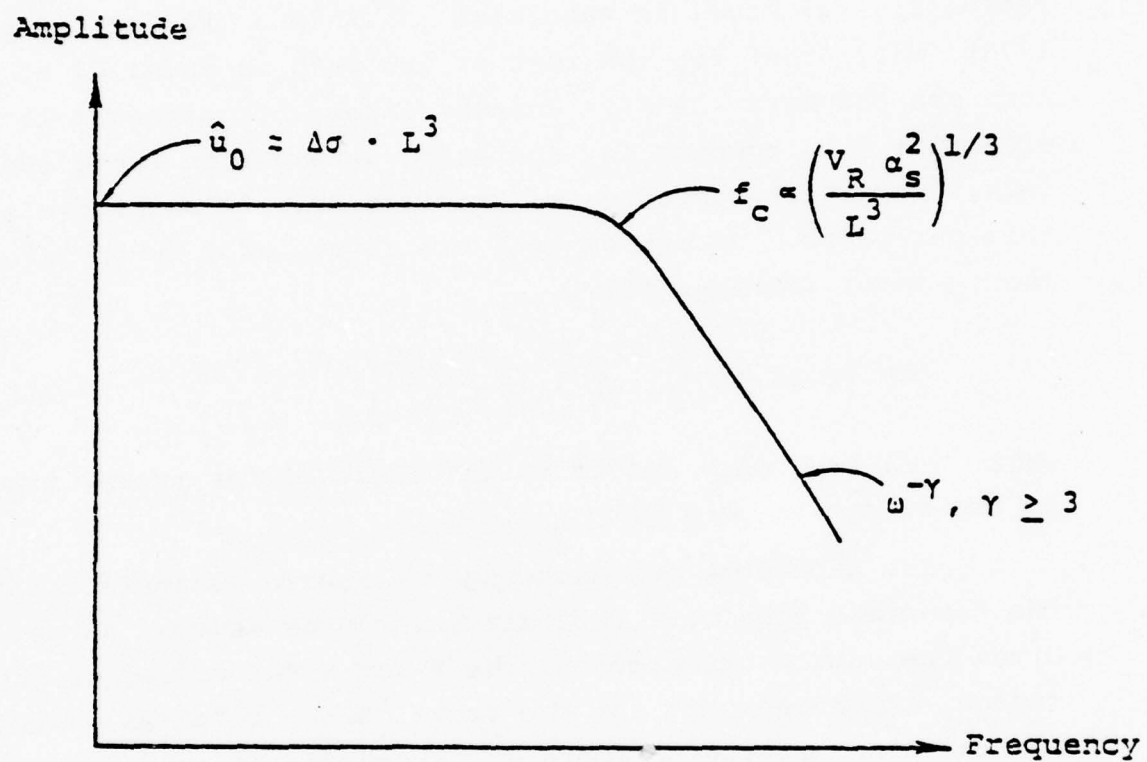
Frequency

Figure 6.   A typical far-field amplitude spectrum is plotted
            for the direct P wave radiated by an earthquake.

21

For determining the amplitude of the source spectrum we must account for elastic and nonelastic attenuation in the earth. Synthetic seismograms are computed with the method of Bache and Harkrider (1976) for embedding a complex source representation in a plane-layered earth model. The source region crustal model is tabulated in Table 3 (Keller, et al., 1975), while that for the rest of the path is Model C2 of Anderson and Hart (1976). Another important parameter is the effective Q to account for anelastic attenuation along the path. The short period waves are particularly sensitive to this parameter. We approximate the effect of Q by applying the operator (Strick, 1970)

$$\exp \left\{ - \pi f \ t^* \left[1 - \frac{2}{\pi} \ i \ \ell n \ \frac{1000}{f} \right] \right\} \tag{1}$$

where f is frequency and t* is the ratio of the travel time to the effective path Q.

The procedure for deducing the source parameters from the far-field body wave recordings includes several steps. Given the source orientation, the P and S velocities in the source region and a t* for the travel path, we guess values for the other source parameters. Synthetic seismograms are then computed and compared to the observations. The free source parameters ($\Delta\sigma$, V_R, L, depth) are then adjusted to optimize the agreement.

Because of the nature of the source model, the parameters that are actually fixed by the procedure are Poisson's ratio (ν), $\Delta\sigma$ and the ratios L/V_R, V_R/β. That is, events with the same ν, L/V_R, V_R/β and $\Delta\sigma$ are indistinguishable. In the sequel we will assume ν is known.

2.5   COMPARISON OF SYNTHETIC AND OBSERVED SEISMOGRAMS

Comparing synthetic and observed seismograms, we have constructed a model of the Pocatello Valley earthquake. The

TABLE 3

NORTHERN WASATCH (Keller, et al., 1975)

Layer	Depth	Thickness	α_s	β_s	ρ_s
1	1.4	1.4	3.4	2.0	2.25
2	15.5	14.1	5.9	3.4	2.73
3	20.0	4.5	6.0	3.5	2.80
4	25.0	5.0	6.0	3.5	2.80

model parameters were selected by trial and error to fit the data, beginning with the geological information we have discussed.

We first consider the long period body waves. For an event of this size the source corner frequency is well outside the bandpass of the long period instrument. That is, these data are mainly sensitive to the source orientation, depth and moment. Finite source effects such as the source dimension and rupture velocity do not play a role.

We begin with a simple model including constant rupture velocity and stress drop. This model (referred to as Model I) is characterized by the following parameters.

MODEL I

Fault Length, L: 3 km

Rupture Velocity, V_R: 3 km/sec

(Unilateral fault propagation toward the surface)

Stress Drop, $\Delta\sigma$:   257 bars

Orientation: Strike N45°
                       Dip 39°W
                       Slip Up 53°N

Of course, L and V_R have no significance other than the fact that they give the correct moment. The stress drop is selected to bring the amplitudes of observed and synthetic records into agreement, as we shall see. For the Archambeau/Minster model the moment is (Minster and Suteau, 1977)

$$M_O = 1.024 \ L^3 \ \Delta\sigma \ . \tag{2}$$

The observed and synthetic long period body wave seismograms are compared in Figure 7 for four WWSSN stations and the Canadian seismic network station RES. The agreement

24

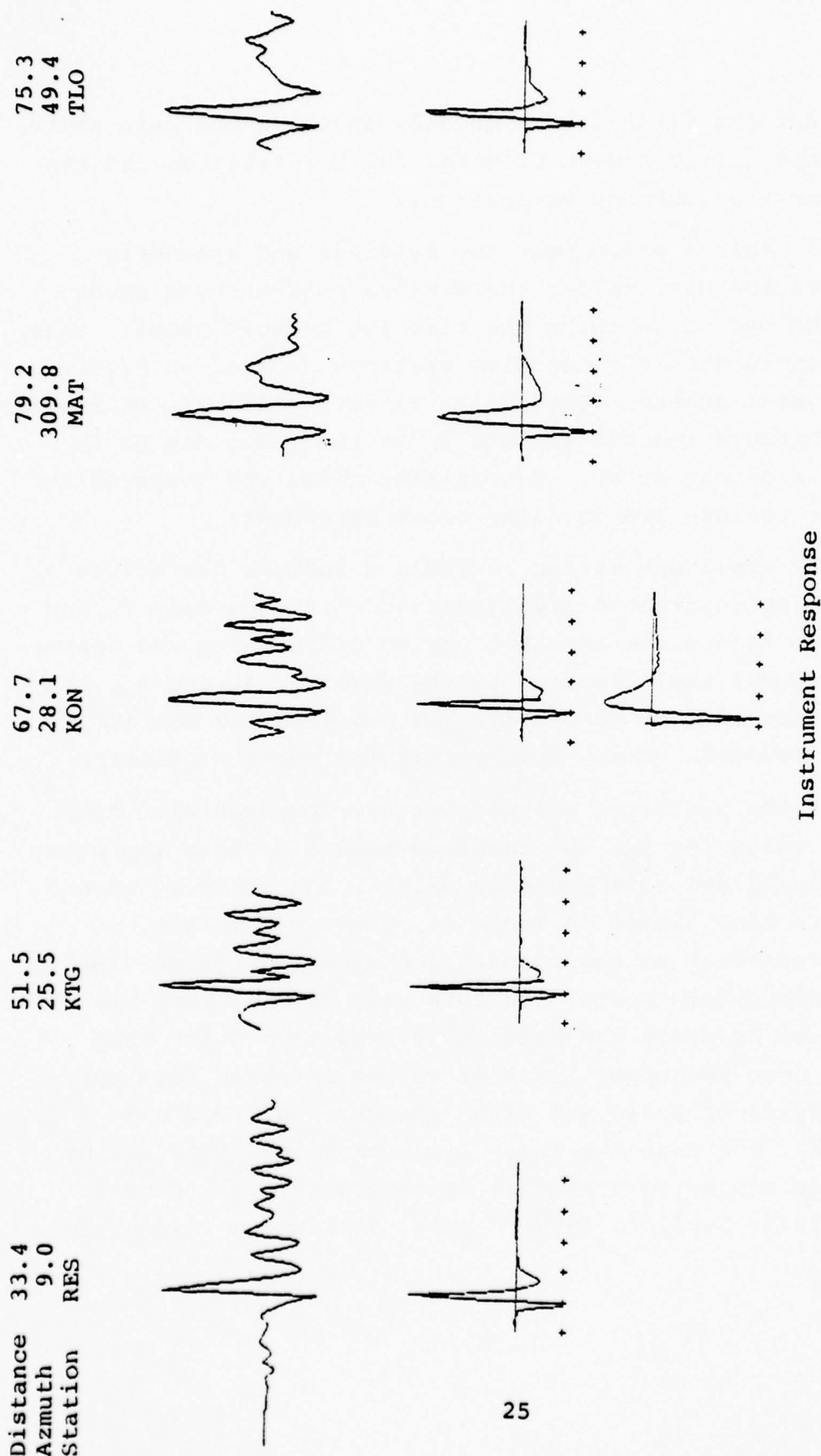| Distance | 33.4 | 51.5 | 67.7 | 79.2 | 75.3 |
| Azmuth | 9.0 | 25.5 | 28.1 | 309.8 | 49.4 |
| Station | RES | KTG | KON | MAT | TLO |

Instrument Response

Figure 7. Observed long period seismograms (top) are compared with synthetic seismograms using Model I (bottom) for five WWSSN stations. The time scale is marked at 10 second intervals. Also shown is the negative impulse response of the long period (15-100) WWSSN seismometer.

25

is good for the first 5 to 8 seconds in which the main arrivals are the direct P wave from the fault initiation and the associated free surface reflections.

In Table 4 we compare the observed and synthetic amplitudes and periods for the maximum peak-to-peak excursion. The period is twice the time lag between peaks. This comparison is done for the five stations plotted in Figure 7 and several others. The period is very difficult to measure on the observed records and the T_O in the table may be in error by a second or so. Recognizing this, the observed and synthetic periods are in quite close agreement.

The amplitude ratios in Table 4 include the effect of differing instrument amplification at the periods T_O and T_S. If we ignore the apparent period differences and assume the instrument amplification is the same for A_O and A_S, the mean is increased by 10 percent and the standard deviation is slightly reduced. These differences are not significant.

If the synthetic seismograms are computed with some standard value for M_O, the inferred moment is then the product of A_O/A_S and this standard value. The inferred moment values are also listed in Table 4. These values are, of course, dependent on the elastic and anelastic properties of the path model chosen. In this case we are using the model C2 of Anderson and Hart (1976) and $t* = 0.8$. This value is near the upper limit of values inferred from spectral analysis of Basin and Range events (e.g., Der and McElfresh), but near the lower limit of values obtained by an analysis employing synthetic seismograms (e.g., Bache, et al., 1975; Burdick, 1978). Thus, it seems a reasonable choice.

26

TABLE 4

AMPLITUDE AND PERIOD COMPARISONS
FOR LONG-PERIOD SEISMOGRAMS FOR MODEL I

Station	Azimuth (E from N)	Distance (degrees)	Amplitude Ratio A_o/A_s	Periods T_o/T_s	Inferred M_o ($\times 10^{24}$ dyne-cm)
RES	9.0	33.4	0.91	4.4/4.9	6.4
KTG	25.5	51.5	1.13	5.6/4.7	7.9
KON	28.1	67.7	0.67	6.0/4.9	4.7
STJ	61.2	42.1	1.11	5.5/5.0	7.8
KBS	14.1	56.8	0.71	6.0/4.9	5.0
KEV	14.8	64.4	C.94	5.0/5.0	6.6
NUR	21.1	71.7	1.26	5.0/5.0	8.8
MAT	309.8	79.2	1.42	6.0/5.0	9.9
TLO	49.4	75.3	1.08	5.6/4.9	7.6
Logarithmic mean			1.00		7.0
standard deviation			28%		28%
With period dependent-instrument amplication ignored:					
Logarithmic mean			1.10		7.7
standard deviation			25%		25%

The moment values inferred from the nine stations in Table 4 are remarkably consistent; the standard deviation is only 28 percent of the mean, or less if we ignore the frequency dependent instrument correction. The mean value is 7.1×10^{24} dyne-cm. This is near the preliminary moment estimate given by Arabasz, et al. (1975a) and is almost the same as the value obtained by Battis and Hill (1977) from surface waves (see Table 1). The stress drop for Model I is $\Delta\sigma = 253$ bars, which scales the moment of this value.

Now let us direct our attention to the short period records. These data are sensitive to rather fine details of the source. Since the teleseismic short period records are often quite complicated and are influenced by both path and source details, they have not often been used to infer source characteristics. However, we were successful in modeling the short period records for the San Fernando earthquake (Bache and Barker, 1978) and were anxious to see how well other events could be modeled.

Synthetic short period records from Model I are compared to the observed records at five teleseismic stations in Figure 8. Synthetic seismograms also are shown for a model we call Model II, but we will discuss these a bit later. There are few stations where the records are clear enough to digitize and those shown are the best of them. The main arrivals on the synthetic are P and pP. The sP phase is rather small for this source orientation.

Comparison of the synthetic and observed records allows us to identify the largest phase as pP. The P wave is small and characterized by low signal-to-noise. It is not easy to identify and measure on the observations.

The main diagnostic features of the comparison include the waveform and frequency content of P and pP and the

28

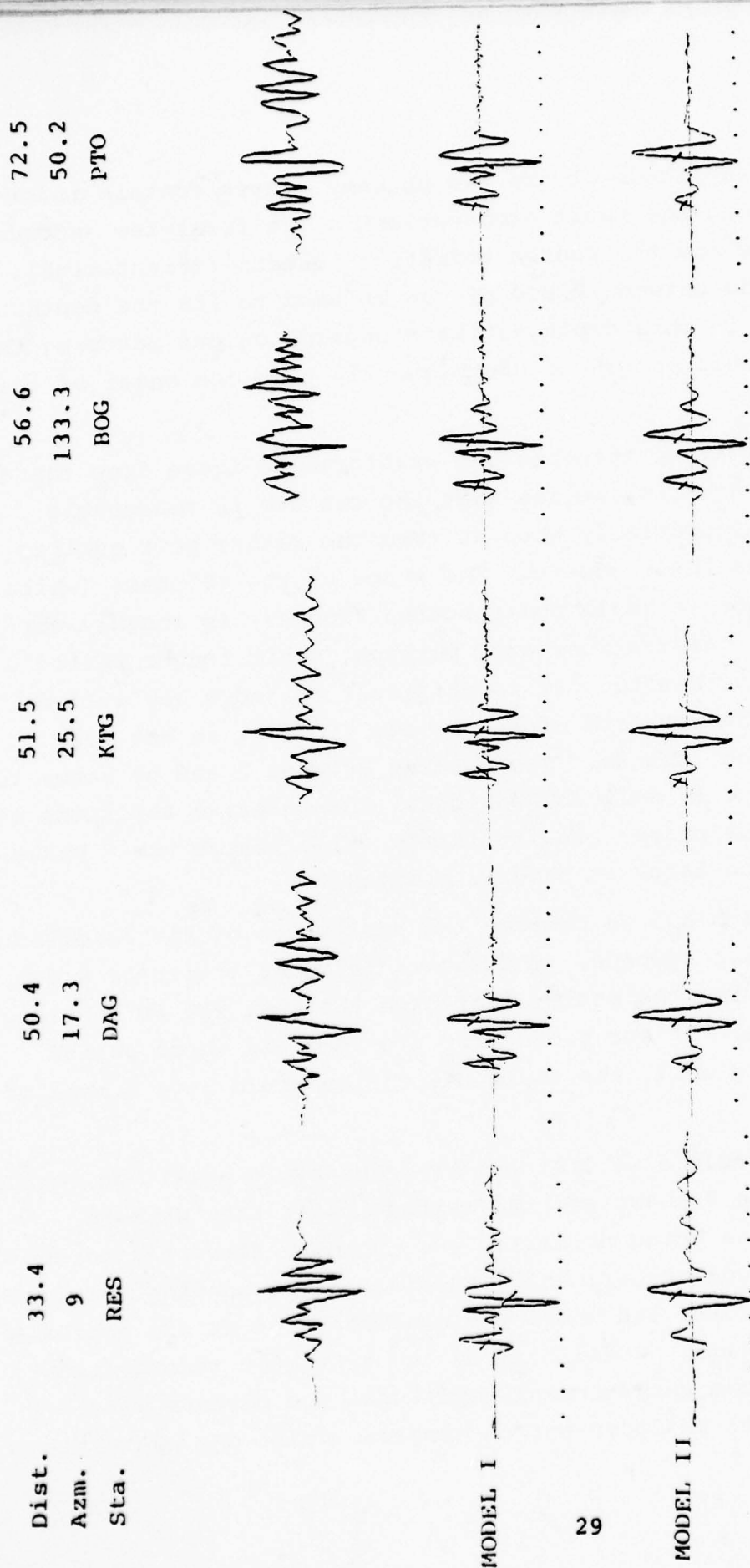| Dist. | 33.4 | 50.4 | 51.5 | 56.6 | 72.5 |
| Azm. | 9 | 17.3 | 25.5 | 133.3 | 50.2 |
| Sta. | RES | DAG | KTG | BOG | PTO |

MODEL I

MODEL II

Figure 8. Observed and synthetic seismograms are compared at five WWSSN stations for Models I and II. Tick marks are at 1 second intervals.

relative amplitude of the two phases. These contain infor-
mation about the fault propagation in the first few seconds
of rupture and the source radiation pattern (orientation).
The spacing between P and pP can be used to fix the depth.
Precision in this depth estimate depends on our matching the
waveform well enough to unambiguously pick the onset of the
two phases.

Comparing the observed waveforms to those from the
Model I synthetic, we see that the two are in reasonable
agreement, especially when we take the rather poor quality
of the data into account. The shape of the pP phase (which
also includes a small contribution from sP) is roughly cor-
rect. The observations are, perhaps, a bit longer period
than the synthetics. It is difficult to judge how well we
have fit the waveform of the P wave since it is not very
clear on the records. The spacing between P and pP seems to
be fit about as well as possible. The relative amplitude of
the P and pP phases are fit fairly well, though the P phase
is a bit too large at several stations.

In Table 5 we compare the amplitudes of the observed
and synthetic records. The source is Model I with $\Delta\sigma$ = 253
bars; that is, the source that gave the best fit to the long
period data. If our source fit the long and short period
data equally well, the amplitude ratios would have a mean of
unity.

In Table 5 we list observed/synthetic amplitude ratios
for both the P phase and the maximum phase that we have
identified as being primarily pP. We have attempted to com-
pare amplitude measurements made from corresponding portions
of the waveforms and where the measured periods are approxi-
mately the same. Small bars on the synthetic records indi-
cate where the peak-to-peak amplitudes and periods were
measured. It is important to compare amplitudes where the

30

TABLE 5

AMPLITUDE AND PERIOD COMPARISONS
FOR SHORT PERIOD SEISMOGRAMS FOR MODEL I

STATIONS	P PHASE		MAXIMUM AMPLITUDE	
	Amplitude Ratio A_O/A_s	Periods T_O/T_s	Amplitude Ratio A_O/A_s	Periods T_O/T_s
RES	0.097	1.2/1.2	0.16	1.3/1.0
DAG	0.08	1.1/1.2	0.21	1.3/1.2
KTG	0.18	1.2/1.2	0.32	1.3/1.2
BOG	0.37	1.4/1.2	0.33	1.2/1.2
PTO	0.19	1.4/1.3	.27	1.7/1.3
Logarithmic Mean standard deviation	0.16 82%		0.25 36%	

apparent frequency content is about the same to avoid having to make a large correction for the frequency-dependent instrument response. This instrument correction is a rough approximation at best, and we try to minimize its effect.

The P wave amplitude ratios in Table 4 have a mean of 0.16 while the amplitude ratios for the maximum amplitude have a mean of 0.25. For the former the scatter is very large with the standard deviation being 83 percent of the mean for this small population. The maximum phase data have much less scatter, which is probably due to this phase being much better defined.

The data in Table 4 force us to the conclusion that Model I cannot simultaneously fit the long and short period data. When we adjust the model to have the correct moment, the synthetic short period body waves are too large by a factor of 4 to 6. Yet we have matched the frequency content of the short period records reasonably well.

The only difference between the long and short period synthetic records is in the instrument response. Both use the same source and earth models. The discrepancy between short and long period sources could be reduced a bit by supposing a large t*, but this could only account for a relatively minor adjustment.

To match the data, we need a source that has the same long period level as Model I, but 4 to 6 times smaller amplitudes in the 0.5 to 2.0 Hz range sampled by the short period instrument. Since the frequency content of Model I is about right, we cannot do this by merely supposing a larger source dimension (with lower stress drop) to reduce the corner frequency.

In our study of the San Fernando earthquake (Bache and Barker, 1978) we found the same kind of difficulty in simultaneously matching long and short period data. We

32

concluded that this discrepancy could only be resolved by constructing a variable stress drop/variable rupture velocity model for the faulting. We believe the same conclusion is warranged here.

We construct a second model for the Pocatello Valley earthquake, Model II. Our hypothesis is that the earthquake must have included regions of faulting with relatively low stress drop and rupture velocity that are important for the long period radiation, but are only weak radiators of the high frequency radiation seen on the short-period recordings. Many combinations of fault parameters were tried. The "best" of these will be described. The solution is, of course, far from unique.

The faulting for Model II includes two regions. In the first region the source parameters are constant and not unlike the values for Model I. The remainder of the faulting is characterized by a rupture velocity that decays to zero, linearly with rupture time. In this region the stress drop decays to zero, but with a cubic dependence on rupture velocity. This rapid decay of stress drop was chosen to compensate for the cubic dependence of amplitude on source dimension that is peculiar to the Archambeau/Minster model. A less rapid decay of stress drop generated too much long period energy in the short period synthetics. In summary, we have the following:

<u>MODEL II</u>

Fault Length, L: 7 km

Rupture Velocity, V_R: 3 km/sec, $0 \leq L \leq 4$

$(21-3L)^{1/2}$ km/sec, $4 \leq L \leq 7$

Stress Drop, $\Delta\sigma$: 46 bars, $0 \leq L \leq 4$

$1.7 (21-3L)^{3/2}$ bars, $4 \leq L \leq 7$

(unilateral fault propagation toward the surface)

33

Depth, H: 8.7 km

Orientation: Strike N45°, Dip 39°W
                           Slip Up 53°N

The dependence of V_R and $\Delta\sigma$ on position along the fault is plotted in Figure 9.

As far as the long period records are concerned, Models I and II are essentially the same. The short period synthetics for both models appear in Figure 8. The Model II records are clearly longer period and are missing some of the high frequency detail exhibited in the Model I records. As far as the major phases are concerned, the P and pP, the Model II records seem preferable at some stations while at others no advantage is apparent with either model. Another attractive feature of Model II is that its dimension is more consistent with the size of the region defined by the aftershock locations (Figures 2 through 4). Perhaps a better model could be found somewhere between the two; they seem to span a range of desirable models.

The amplitude data for Model II are tabulated in Table 6 in the same format as the Model I data in Table 5. We see that the amplitude ratios are 2 to 3 times larger for Model II than they were for Model I. While this model has the correct long period level, the synthetic short period records are still, on the average, about a factor of two, larger than the observations. It may be that this is as close as it is reasonable to get, given the many errors inherent in the procedure and the relatively poor quality of the data.

Attempts to improve the agreement must focus on constructing a source that has an even larger region that contributes to the long period energy without substantially altering the short periods. This is difficult because the long period level is constrained by data at periods that are not all that long; five or six seconds. Also, the short period waveforms for Model II are already too long period.

34

TABLE 6

AMPLITUDE AND PERIOD COMPARISONS
FOR SHORT PERIOD SEISMOGRAMS FOR MODEL II

Station	P PHASE		MAXIMUM AMPLITUDE	
	Amplitude Ratio A_O/A_S	Periods T_O/T_S	Amplitude Ratio A_O/A_S	Periods T_O/T_S
RES	0.16	1.2/1.9	0.14	1.3/2.0
DAG	0.56	1.8/2.0	0.38	13/1.6
KTG	0.92	1.7/1.8	0.52	1.3/1.6
BOG	0.52	1.4/2.0	0.89	1.2/1.5
PTO	0.33	1.4/1.9	0.43	1.7/1.7
Logarithmic mean*	0.55		0.52	
Standard deviation	51%		45%	

*RES is not included in the mean determination because the period differences are too large for meaningful amplitude comparisons.
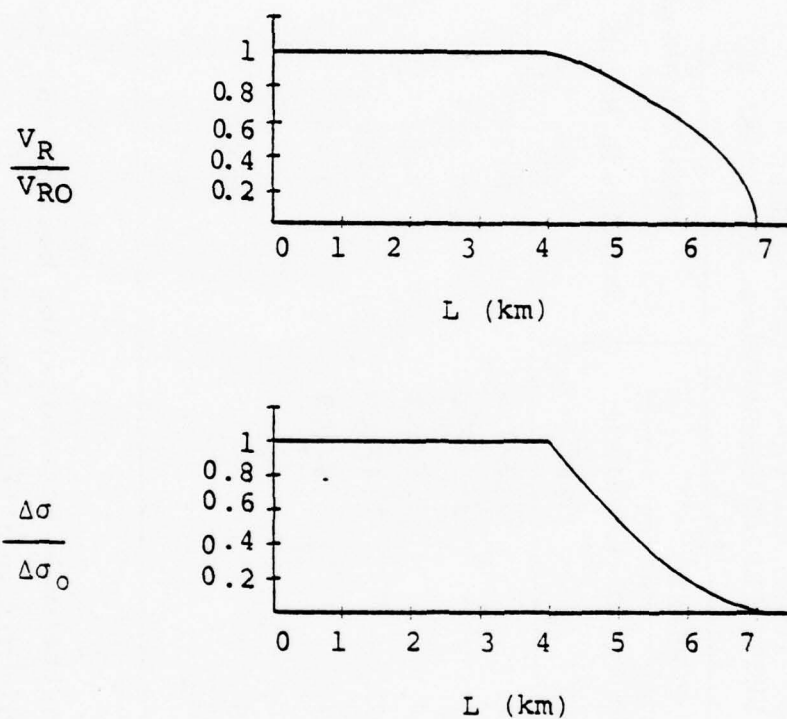
Figure 9. Rupture Velocity V_R and stress drop $\Delta\sigma$ versus position on the fault for Model II are shown. Values are normalized to their initial values, $V_{RO}=3$ km/sec and $\Delta\sigma_O = 46$ bars.

Another interesting and potentially important aspect of these data is that they show evidence of a small precursor event a second or so before the main event. On the original Develocorder records for each of the five stations studied there is a small arrival just before the main P arrival. Unfortunately, our digitization is too poor to see this very clearly in the Figure 8 plots, though it can be discerned on the RES, DAG and PTO playouts. The sharp break in the waveform between the major P and pP arrivals is consistent in amplitude and time with a pP from such a precursor event at roughly the same depth and orientation as the main event. This event appears to be about 20 percent as large as the main event at 1 to 2 Hz and to be at approximately the same depth and orientation. The time lag of from 1 to 1.5 seconds could be a result of both spatial and temporal separation.

2.6   CONCLUSIONS

We first summarize the way we have developed our model for the 1975 Pocatello Valley earthquake. We have a rather well-constrained focal mechanism solution for the event. Choice between the two original solutions was made on the basis of the depth distribution of aftershock locations determined by Arabasz, et al. (1975b). Thus, we began our synthetic seismogram studies with considerable confidence in our knowledge of the fault orientation, strike, dip and slip.

The long period P waves are sensitive to the fault orientation, focal depth and moment. The orientation and depth control the waveform while the moment controls the amplitude. Our model fits the first 5 to 8 seconds of the long period observations (Figure 7). The moment we infer is essentially the same as that obtained by independent investigation using other data. Later phases on the long period records are evidence for the complexity of the faulting after the first several seconds.

37

The main phases on the short period observations are
the direct P from fault initiation and the associated pP.
The sP phase is small for this fault orientation. These
data are not of good quality and it is difficult to make
detailed comparisons between observed and synthetic records.
The main diagnostic features are the waveform and frequency
content of the P and pP phases, their spacing and their
relative amplitudes.

We construct Model I, a single rupture velocity,
single stress drop model for the earthquake that gives a
good qualitative fit to the observations (Figure 8). One
discrepancy is that the synthetics appear to be a bit too
short period. However, if this source is to have the right
moment (inferred from the long period data), the synthetic
short period records are much too large--a factor of 3 to 5.
We see no way to resolve this discrepancy except to suppose
that the event includes regions that contribute to the long
period level without substantially adding to the short period
radiation. That is, we need a variable stress drop, variable
rupture velocity, model.

We construct Model II which begins like Model I, then
moves into a region where the stress drop and rupture veloc-
ity decay to zero. This model substantially reduces the
discrepancy between the source amplitudes inferred from the
long and short period data. The main problem with Model II
is that in decreasing the short period amplitude, we have
made the synthetic seismograms too long period. That is, the
variable rupture velocity, variable stress drop effects are
still not strong enough to give an ideal fit to the data.
However, given the rather large errors inherent in the proce-
dure, especially in comparing amplitudes at periods where the
frequency-dependent instrument response is rapidly changing,
Model II can be said to give a reasonably good fit to both

the long and short period data. The fit could, probably, be improved but an improved model must have roughly the same variable stress drop, variable rupture velocity character as our Model II.

The stress drop at initiation of Model II is 45 bars. This compares to the value of 206 bars found with the same methods for the 1971 San Fernando earthquake (Bache and Barker, 1978). In our discussion of that event we point out that the Archambeau/Minster source model consistently under-estimates the stress drop by a factor of about 3.6. Thus, we prefer to estimate the actual stress drop for the initial faulting to be about 162 bars. In any case, this is a factor of 4-1/2 smaller than the San Fernando stress drop estimate.

The meaning of this stress drop difference is diffi-cult to assess and requires further thought. It is fair to say that all stress drop estimates are "average" estimates in some sense. It may be that the Pocatello Valley event includes smaller regions with substantially higher stress drop that are not resolvable with the data at hand. Still, we feel confident that the difference is qualitatively cor-rect and that the Pocatello Valley earthquake was a lower stress drop event.

In the next section we discuss an entirely different method for computing the earthquake source. This is by three-dimensional finite difference modeling of stress relaxation on a fault plane.

III. THREE-DIMENSIONAL FINITE DIFFERENCE EARTHQUAKE MODEL

3.1 INTRODUCTION

A three-dimensional finite difference model (TRES) for earthquake faulting (Cherry, 1977) has been made operational on the parallel processing ILLIAC IV computer. As part of this contract, ILLIAC IV computer time was provided to model earthquake faulting with particular attention to the Pocatello Valley event. In this section we present the results of our earthquake modeling with the ILLIAC program.

While the TRES algorithm is quite flexible in the allowed specification of geometry and material behavior, the version currently operational on the ILLIAC is quite restricted. (The allowed fault plane geometry is shown in Figure 11.) The faulting must be bilateral; in fact, it must nucleate from a point and propagate with circular symmetry until reaching the edges of a rectangular fault plane. There are no material boundaries other than the fault plane; that is, the calculations are done in a whole space.

The material behavior is linearly elastic except in the vicinity of the fault plane where plastic yielding is permitted. Including this rather elementary form of inelastic material behavior represents an important first step toward developing realistic models for the true physics of earthquake faulting.

Two full calculations were carried out and the results will be described in this section. For both calculations the material properties and geometry are close to those inferred for the Pocatello Valley earthquake in the previous section. The difference between the two is that the elastoplastic behavior near the fault plane was allowed in one case and not in the other.

40

In this section we describe the finite difference modeling in detail and present the results as they apply to earthquakes in general. In later sections we will relate these results to the Pocatello Valley earthquake and discuss the implications for western U.S. earthquakes in more general terms.

Section 3.2 describes the problem formulation, and Section 3.3 gives the fault and material parameters employed in the two finite difference calculations. In Section 3.4, we discuss methods for continuing the numerical solutions to distances beyond the calculational mesh. In Section 3.5, we compare our numerical solution for the purely elastic case to available analytical and numerical results for similar problems, in order to verify the accuracy of the numerical method. Section 3.6 presents the results for the near source stress and velocity fields for both finite difference calculations. The far-field radiation for both calculations is discussed in Section 3.7.

3.2 PROBLEM FORMULATION

We treat faulting as a propagating stress relaxation due to shear failure on a planar surface. Ideally, we would like to specify the relevant physical properties of the medium and its initial conditions, and allow a mathematical model of failure to determine the subsequent evolution of the fault plane. However, this study does not address the physical mechanism of failure. Instead, we prescribe the propagation of the fault surface. Boundary conditions on the fault surface are governed by a simple Coulomb friction law.

We will specify: (i) the initial state of the medium and its constitutive properties, (ii) the evolution of the fault plane, and (iii) the boundary conditions to be satisfied on the fault plane. The mathematical model of faulting

41

is then solved using a three-dimensional finite difference method (Cherry, 1977).

3.2.1 Initial Conditions and Constitutive Properties

For time t less than zero we assume that an equilibrium state of stress exists, with displacement and velocity everywhere zero. The equilibrium configuration is such that the prospective fault plane experiences a shear stress σ_T and a compressional normal stress σ_N.

Average stress changes associated with faulting are modest -- on the order of a few hundred bars. Furthermore, faulting represents a relaxation of stress, except near the fault edges. Linear elasticity is thus probably an adequate model of material behavior outside the immediate zone of faulting. However, large strains do occur at the edges of the fault ahead of the rupture. Some model of rock strength must be incorporated to prevent large stress concentrations from accruing immediately ahead of the fault.

For this study, a simple model of plastic yield was utilized in the region adjacent to the fault. The plastic flow model is as described in Cherry, et al. (1976). If $\underset{\sim}{\underline{\sigma}}'$ is the deviatoric stress tensor, calculated assuming that the strain rate is elastic, then the actual stress deviator $\underline{\sigma}'$ is given by

$$\underline{\sigma}' = \begin{cases} \underset{\sim}{\underline{\sigma}}' \dfrac{Y}{\sqrt{3J_2}} & \text{for} \quad J_2 > \dfrac{Y^2}{3}, \\[4mm] \underset{\sim}{\underline{\sigma}}' & \text{for} \quad J_2 \le \dfrac{Y^2}{3}, \end{cases} \tag{3}$$

where J_2 is the second deviatoric invariant defined by

$$J_2 = \frac{1}{2} \underline{\underline{\tilde{\sigma}}}' : \underline{\underline{\tilde{\sigma}}}'$$

and Y is a material constant representing yield strength. The stress adjustment described by Equation (3) is permitted only within a specified zone near the fault. Elsewhere, linear elasticity is presumed to hold.

3.2.2 Evolution of the Fault Plane

For this study, we specify the geometry of the fault surface as a function of time, rather than deriving the fault surface from the model as a consequence of a failure mechanism. This is viewed as a first step toward more fully deterministic calculations.

The rupture surface is assumed to be planar, to nucleate from a point, and to expand symmetrically at a constant prescribed rupture velocity (V_R), until it reaches prescribed boundaries. $\Sigma(t)$ denotes the fault surface. If r and θ are polar coordinates in the fault plane, with r being the hypocentral distance, and if the edge of $\Sigma(\infty)$ is defined by the curve

$$r = B(\theta),$$

then $\Sigma(t)$ consists of all points r, θ such that

$$r < \min [V_R t, B(\theta)] \, H(t) \ .$$

Two significant features of this model of rupture are (i) the rupture velocity accelerates instantaneously to its final velocity, and (ii) the rupture advance terminates abruptly, i.e., the rupture velocity decelerates instantaneously to zero at some prescribed boundary. The former assumption may be quite reasonable. There is both theoretical (Cherry, et al., 1976; Das and Aki, 1977) and experimental

43

(Archuleta and Brune, 1975) evidence that ruptures accelerate rapidly to their terminal velocity, with the rupture velocity essentially constant over most of the fault. The latter assumption, that stopping of the rupture is abrupt, is probably an unrealistic model for many earthquakes. For example, Bache and Barker (1977) infer a fault model for the San Fernando earthquake in which the rupture velocity decelerates smoothly to zero. On the other hand, if the rupture termination is controlled by a fracture energy barrier, abrupt stopping may be appropriate (Husseini, et al., 1975).

3.2.3 Boundary Conditions on the Fault

On $\Sigma(t)$ we permit a tangential displacement discontinuity $\underline{s}(\underline{x},t)$, and require continuity of the normal displacement:

$$\underline{s}(\underline{x},t) \equiv \lim_{\varepsilon \to 0} [\underline{u}(\underline{x} + \varepsilon\hat{\underline{n}}) - \underline{u}(\underline{x} - \varepsilon\hat{\underline{n}})], \ \underline{x} \text{ on } \Sigma,$$

$$\hat{\underline{n}} \cdot \underline{s} = 0,$$

(4)

with $\varepsilon > 0$. The $\hat{\underline{n}}$ is a unit vector normal to Σ and $\underline{u}$ is the displacement vector. We also require continuity of traction.

The tangential traction on Σ is assumed to obey a simple Coulomb friction law. Let $\underline{\tau}$ denote the tangential traction vector, defined in terms of the stress tensor $\underline{\sigma}$ by

$$\underline{\tau} \equiv - \hat{\underline{n}} \cdot \underline{\sigma} \cdot (\underline{I} - \hat{\underline{n}}\hat{\underline{n}}) \ ,$$

(5)

where $\underline{I}$ is the indentity tensor. Then define $\underline{\tau}_f$ to be a sliding frictional traction which opposes the slip velocity $\dot{\underline{s}}$ and is proportional to the normal stress:

$$\underline{\tau}_f \equiv \begin{cases} - \sigma_f \, \dfrac{\underline{\dot{s}}}{|\underline{\dot{s}}|} & \text{for} \quad |\underline{\dot{s}}| > 0, \\[4mm] 0 & \text{for} \quad |\underline{\dot{s}}| = 0 \end{cases} \tag{6}$$

where σ_f is $-\mu_K \, \hat{\underline{n}} \cdot \underline{\sigma} \cdot \hat{n}$, the product of the normal stress and the coefficient of dynamic friction (σ_f is presumed to be positive). Finally, define $\underline{\tau}_c$ as the tangential traction on Σ which would be required to enforce continuity of velocity.

We wish to set the tangential traction $\underline{\tau}$ equal to $\underline{\tau}_f$ whenever the slip velocity $\underline{\dot{s}}$ is non-zero. At the instant when $\underline{\dot{s}}$ becomes zero at a given point, $\underline{\tau}$ equals $\underline{\tau}_c$, by definition. If further slip is permitted at that point, $\underline{\tau}$ reverse to $\underline{\tau}_f$.

However, there is a condition under which further slip is inconsistent with the equation of motion. To see this, we write the equation of motion (in the absence of body forces) as

$$\rho \underline{\ddot{u}} = \underline{\nabla} \cdot \underline{\sigma} . \tag{7}$$

Letting the fault be the plane $z = 0$, we consider a small sphere surrounding the point x on the fault. Figure 10 illustrates this. S^+ and S^- denote the surface of the hemisphere in the $+z$ and $-z$ halfspaces, respectively. Taking the scalar product of Equation (7), first with $\hat{\underline{x}}$ sgn (z), then with $\hat{\underline{y}}$ sgn (z), integrating over the volume of the sphere, and applying the divergence theorem, we get the pair of equations:

$$\Delta \ddot{u}_x = \frac{2A_\Sigma}{M} \, (\Delta \tilde{f}_x + \tilde{\tau}_x) ,$$

$$\Delta \ddot{u}_y = \frac{2A_\Sigma}{M} \, (\Delta \tilde{f}_y + \tilde{\tau}_y) . \tag{8}$$
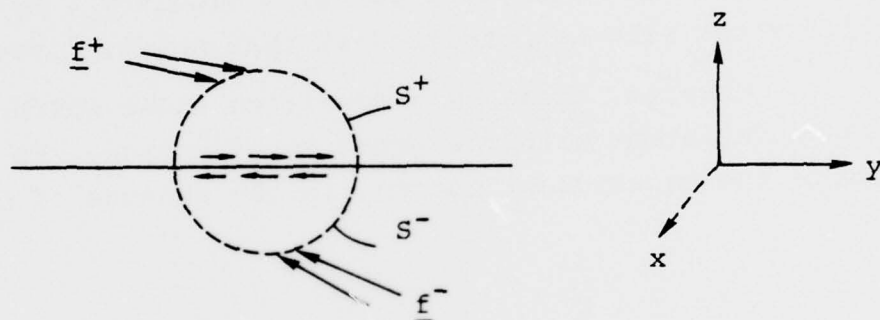
45

Figure 10. Tractions on the exterior of a fictitious spherical
surface centered on a point on the fault plane Σ.
$\underline{f}^+$ and $\underline{f}^-$ are tractions on the hemispheres S^+ and
$\overline{S}^-$, respectively.

A_Σ is the area of the fault plane encompassed by the sphere; M is the mass of each hemisphere; $\Delta\ddot{u}_x$ and $\Delta\ddot{u}_y$ are the x and y components, respectively, of the average acceleration in the +z hemisphere minus the average acceleration in the −z hemisphere; $\Delta\tilde{f}_x$ and $\Delta\tilde{f}_y$ are the x and y components, respectively, of the average traction on the exterior of S^+ minus the average traction on the exterior of S^-; $\tilde{\tau}_x$ and $\tilde{\tau}_y$ are the components, respectively, of $\underline{\tau}$, averaged over A_Σ. As the radius of the sphere is reduced, $\Delta\ddot{u}_x$ and $\Delta\ddot{u}_y$ approach $\ddot{s}_x$ and $\ddot{s}_y$, respectively; and $\tilde{\tau}_x$ and $\tilde{\tau}_y$ approach

$$-\sigma_f \frac{\dot{s}_x}{\left(\dot{s}_x^2 + \dot{s}_y^2\right)^{1/2}} \quad \text{and} \quad -\sigma_f \frac{\dot{s}_y}{\left(\dot{s}_x^2 + \dot{s}_y^2\right)^{1/2}}$$

respectively, if slippage is occurring. Thus, Equation (9) takes the form

$$\ddot{s}_x = \frac{2A_\Sigma}{M}\left[\Delta\tilde{f}_x - \sigma_f \frac{\dot{s}_x}{(\dot{s}_x^2 + \dot{s}_y^2)^{1/2}}\right],$$

$$\ddot{s}_y = \frac{2A_\Sigma}{M}\left[\Delta\tilde{f}_y - \sigma_f \frac{\dot{s}_y}{\left(\dot{s}_x^2 + \dot{s}_y^2\right)^{1/2}}\right]. \tag{9}$$

If slip is to recommence after going to zero at $t = t_o$, $\underline{\dot{s}}(t_o^+)$ will have the same direction as $\underline{\ddot{s}}(t_o^+)$, so the equations at t_o^+ can be written

$$\ddot{s}_x = \frac{2A_\Sigma}{M}\left[\Delta\tilde{f}_x - \sigma_f \frac{\ddot{s}_x}{\left(\ddot{s}_x^2 + \ddot{s}_y^2\right)^{1/2}}\right] \tag{10a}$$

$$\ddot{s}_y = \frac{2A_\Sigma}{M}\left[\Delta\tilde{f}_y - \sigma_f \frac{\ddot{s}_y}{\left(\ddot{s}_x^2 + \ddot{s}_y^2\right)^{1/2}}\right]. \tag{10b}$$

This pair of non-linear equations in two unknowns has the solution (Day, 1977, Appendix IV)

$$\ddot{s}_x = \frac{2A_\Sigma}{M}\left[\Delta\tilde{f}_x - \sigma_f \frac{\text{sgn }(\ddot{s}_x)}{\left(1 + \frac{\Delta\tilde{f}_y^2}{\Delta\tilde{f}_x^2}\right)^{1/2}}\right] \qquad (11a)$$

$$\ddot{s}_y = \frac{2A_\Sigma}{M}\left[\Delta\tilde{f}_y - \sigma_f \frac{\text{sgn }(\ddot{s}_y)}{\left(1 + \frac{\Delta\tilde{f}_x^2}{\Delta\tilde{f}_y^2}\right)^{1/2}}\right]. \qquad (11b)$$

This solution would always exist if the coefficient of the signum function, σ_f, were negative. Note, however, that this coefficient is necessarily positive, by virtue of the fact that friction always opposes the slip velocity. As a result, there exists a condition under which no solution exists to the system given in Equation (10). The condition for no solution is

$$\left(\Delta\tilde{f}_x^2 + \Delta\tilde{f}_y^2\right)^{1/2} < \sigma_f. \qquad (12)$$

This is just the condition that σ_f exceeds $|\underline{\tau}_c|$, in which case we see that further slip is precluded. This leads to the following statement of the boundary conditions on Σ governing $\underline{\tau}$:

$$\underline{\tau} = \begin{cases} \underline{\tau}_f', & \text{if} \quad |\underline{\tau}| > \sigma_f \\ \\ \underline{\tau}_c, & \text{if} \quad |\underline{\tau}_c| \leq \sigma_f \end{cases}. \qquad (13)$$

Thus, healing of the fault is not arbitrarily enforced, but results when the equations of motion will not admit a solution with a velocity discontinuity.

48

3.3 FAULT AND MATERIAL PARAMETERS

We performed two three-dimensional finite difference calculations for this study. The two calculations differed only in the yield strength Y assigned the material. Both calculations were for a square fault plane in a uniform whole space, with rupture initiated at the center of the square fault (Figure 11). The following parameters were employed for both calculations:

P wave velocity	α	$= 5.93$ km/sec
S wave velocity	β	$= 3.42$ km/sec
Density	ρ	$= 2.74$ gm/cm
Rupture velocity	V_R	$= 3.08$ km/sec
Tectonic shear stress	σ_T	$= 1$ kbar
Frictional stress	σ_f	$= 0.82$ kbars
Fault dimensions	$2a \times 2a$	$= 3$ km $\times$ 3 km

For the first finite difference calculation, the "elastic" model, the yield strength Y was set to infinity, so the constitutive model was linearly elastic. For the second finite difference calculation, the "plastic" model, Y was set to $\sqrt{3\sigma_T}$, so that the fault zone was initially stressed to the failure surface. With this choice of Y, plastic flow ensues when the deviatoric invariant increases above ıts initial value. This dissipates any dynamic shear stress concentration ahead of the crack tip. Plastic yield was permitted only within 0.2 km of the fault plane; elsewhere linear elasticity was employed.

For both the elastic and the plastic fault problems, the medium was represented by cubic finite difference zones 0.1 km on a side. The numerical grid was large enough that no reflection from the exterior grid boundary returned to the fault zone during the calculation.
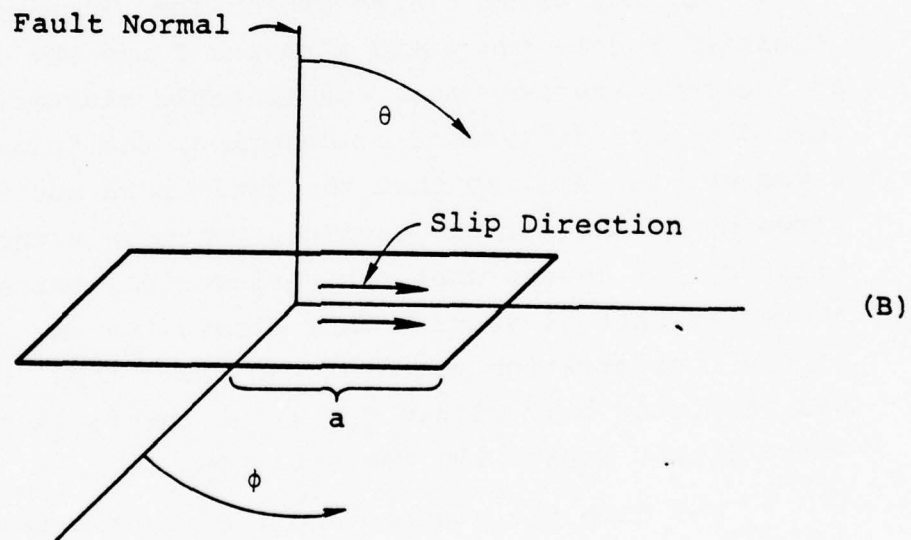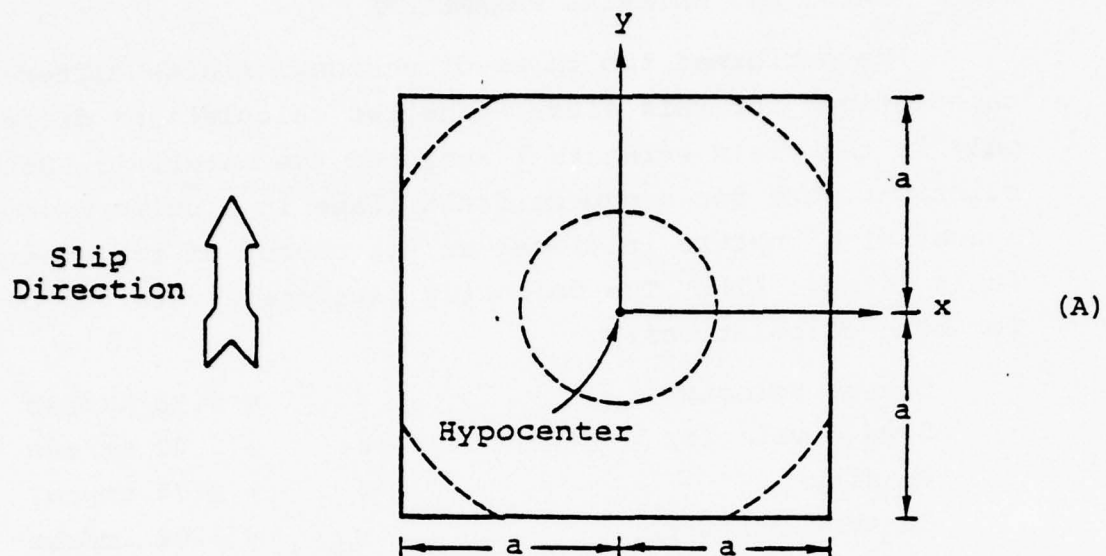
Figure 11. (A) The fault configuration for the finite
difference simulation, and (B) the coordinate
system for describing the radiated field.

50

The formulation of Section 3.2 was simplified somewhat for
these finite difference calculations by prohibiting fault
slip in the direction normal to the prestress direction.
This restriction should not have a significant effect on the
solution. It is known, for example, that for the self-similar,
expanding elliptical crack, the slip is everywhere parallel
to the prestress. Furthermore, Madariaga (1976) has shown
that the perpendicular component of slip is very small for
the case of a finite circular crack.

3.4   CONTINUATION OF THE ELASTIC FIELD

The computing cost for three-dimensional finite dif-
ference calculations increases rapidly with the distance over
which waves must be propagated through the numerical grid.
Since we are interested in simulating earthquake ground motion
at a variety of distances, it is important to be able to link
the numerically computed wave fields to analytic wave propaga-
tion methods. A very general method for doing so is provided
by an elastodynamic integral representation given by, for
example, Burridge and Knopoff (1964). The approach is approp-
riate in both the near-field and far-field. Two elements are
necessary for this analytic continuation: (i) Time histories
of the stress vector $\underline{\tau}$ $(\underline{x}_o, t)$ and the displacement vector
$\underline{u}$ $(\underline{x}_o, t)$ are required on a surface Σ surrounding the source
(and enclosing any inelastic region). These are available from
the finite difference source calculation. (ii) The Green's
(tensor-valued) function $\underline{g}$ $(\underline{x}, \underline{x}_o; t-t_o)$ and its spatial
derivatives are needed for the elastic medium representing the
propagation path to the observation point of interest $\underline{x}$. For
a horizontally layered earth structure, these can be readily
computed by wave propagation techniques.

When (i) and (ii) are evaluated, the solution for mo-
tion at a given site is obtained via spatial integrals over

51

the surface surrounding the source. The general form of the integral representation (assuming isotropy) is:

$$\underline{u}\ (\underline{x},t) = \int_{-\infty}^{\infty} dt \int_{\Sigma} dS\ [\underline{\underline{g}}\ (\underline{x},\underline{x}_o;\ t-t_o) \cdot \underline{\tau}\ (\underline{x}_o,t_o)$$

$$- \underline{\underline{g}}\ \underline{\nabla}\ (\underline{x},\underline{x}_o;\ t-t_o) : \underline{\underline{M}}\ (\underline{x}_o,t_o)] \qquad (14)$$

where

$$\underline{\underline{M}}\ (\underline{x}_o,t_o) \equiv \lambda \underline{\underline{I}}\hat{\underline{n}} \cdot \underline{u}\ (x_o,t_o) + \mu\ [\hat{\underline{n}}\underline{u}\ (x_o,t_o)$$

$$+ \underline{u}\ (\underline{x}_o,t_o)\ \hat{\underline{n}}]\ ,$$

$\underline{x}$ and t are receiver position and time,

λ and μ are elastic constants,

$\hat{\underline{n}}$ is the normal to Σ, directed into the source volume,

$\underline{u}$ is the displacement vector,

$\underline{\tau}$ is the stress vector on Σ,

$\underline{\underline{g}}$ is the Green's tensor solution,

$\underline{\underline{I}}$ is the identity tensor.

In the special case in which inelasticity near the fault is negligible, the surface can be reduced to the fault plane. In this case, the continuation method reduces to the so-called dislocation method (see, for example, Haskell, 1964; Aki, 1968) -- only the displacement discontinuity at the fault need be monitored in order to propagate the source disturbance.

Two special cases of the representation are particularly useful for isolating the far-field radiation. The first method applies to any spherical source region embedded in a uniform elastic whole space. The second applies to a planar failure surface embedded in a uniform whole space.

52

We designate these the "multipolar expansion" method and the "angular spectrum" method, respectively. We will apply these methods in subsequent sections to obtain the radiated seismic field from the finite difference solutions.

3.4.1 Multipolar Expansion Method

When the source region is embedded in a homogeneous whole space, we can simplify the representation of the exterior seismic field. This is accomplished by choosing the integration surface to be a sphere, writing the displacements and Green's functions in terms of scalar and vector potentials (divergence and curl) and expanding the scalar potentials as spherical harmonic series. The approach applies equally well to the elastic and elastoplastic cases in this study, provided the integration sphere surrounds the region of non-linearity. Bache and Harkrider (1976) and Bache, et al. (1975) give details of the formulation. The following is a brief outline of the method.

The Fourier transformed equations of motion in a homogeneous, isotropic, linear elastic medium may be written

$$\underline{u} = - \left(\frac{1}{k_\alpha^2}\right) \nabla \chi^{(4)} + \left(\frac{2}{k_\beta^2}\right) \nabla \times \underline{\chi} \tag{15}$$

where $\underline{u}$ is displacement and k_α and k_β are the compressional and shear wave numbers. The Cartesian potentials $\chi^{(4)}$ and $\underline{\chi}$ are defined by

$$\chi^{(4)} = \nabla \cdot \underline{u} , \tag{16}$$

$$\underline{\chi} = \frac{1}{2} \nabla \times \underline{u} .$$

The potentials can be shown to satisfy wave equations and therefore can be expanded in spherical eigenfunctions as follows:

$$\chi^{(j)}(\underline{x},\omega) = \sum_{\ell=0}^{\infty} h_\ell^{(2)}(k_j r) \sum_{m=0}^{\ell} \left[A_{\ell m}^{(j)}(\omega) \cos m\phi \right.$$

$$\left. + B_{\ell m}^{(j)}(\omega) \sin m\phi \right] P_\ell^m(\cos\theta), \quad j = 1,2,3,4 \qquad (17)$$

where $k_4 \equiv k_\alpha = \omega/\alpha$ and $k_i \equiv k_\beta = \omega/\beta$ for $i = 1,2,3$. The $h^{(2)}$ are spherical Hankel functions of the second kind and the P_ℓ^m are associated Legendre functions. $\underline{x}$ is the position vector, and r,θ,ϕ are spherical coordinates such that $\underline{x}$ is given in terms of Cartesian unit vectors $\hat{\underline{x}}$, $\hat{\underline{y}}$, $\hat{\underline{z}}$ by

$$\underline{x} = \hat{\underline{x}} \, r \sin\theta \cos\phi + \hat{\underline{y}} \, r \sin\theta \sin\phi + \hat{\underline{z}} \, r \cos\theta.$$

The multipole coefficients $A_{\ell m}^{(j)}(\omega)$, $B_{\ell m}^{(j)}(\omega)$, $j = 1,\ldots,$ 4, are determined from the observed divergence and curl of the displacement, obtained from the finite difference solution. Using the orthogonality of the spherical harmonics, the multi-pole coefficients are given by the expression

$$\begin{Bmatrix} A_{\ell m}^{(j)}(\omega) \\[2ex] B_{\ell m}^{(j)}(\omega) \end{Bmatrix} = \frac{C_{\ell m}}{h_\ell^{(2)}(k_\alpha R)} \int_0^{2\pi} \int_0^{\pi} \chi^{(j)}(\underline{x},\omega) \, P_\ell^m(\cos\theta) \begin{Bmatrix} \cos m\phi \\[2ex] \sin m\phi \end{Bmatrix} \sin\theta \, d\theta \, d\phi, \qquad (18)$$

where

$$C_{\ell m} = \frac{(2\ell+1)(\ell-m)!}{2\pi(\ell+m)} \, , \quad m \neq 0$$

$$C_{\ell 0} = (2\ell+1)/4\pi,$$

and R is the radius of the spherical surface on which the integral is to be computed.

The multipole coefficients $A_{\ell m}^{(j)}(\omega)$, $B_{\ell m}^{(j)}(\omega)$, $j = 1,\ldots,$ 4 specify the displacement field (through Equations 15 and 17)

54

everywhere exterior to the (spherical) source region. This is a convenient form for studying whole space radiation properties. Separation into near- and far-field components is simple, since the r dependence is isolated in the spherical Hankel functions. Also, radiation patterns are easily exhibited, since the angular dependence is isolated in the spherical harmonics.

One significant drawback to this approach is the necessity to compute the full transient finite difference solution on the spherical surface. This requires considerably more computation time than is required to complete the transient solution on the fault plane. A second difficulty is that there is some uncertainty in the number of terms which must be retained in the expansion in order to obtain convergence at a given frequency. Finally, the expansion is poorly convergent when the distance from the origin to the observation point is comparable to the source dimension.

3.4.2 Angular Spectrum Method

When non-elastic behavior can be neglected, the integration surface can be collapsed to the fault plane. For this case, Kostrov (1968) and Dahlen (1974) review the resulting simplification of Equation (14) for finding the far-field, whole space radiation. The first term in Equation (14) vanishes, due to the continuity of traction at the fault plane. Further simplification results from employing the far-field approximation to the whole space Green's tensor, the point-source approximation (source dimension much less than source-receiver distance), and from assuming a planar fault surface with uni-directional slip tangential to the fault plane. This leads to Dahlen's (1974) Equations (13) to (16) for the Fourier transformed P and S wave displacements $\underline{u}^{\alpha}$ and $\underline{u}^{\beta}$, which can be written as

55

$$\underline{u}^\alpha (r,\theta,\phi,\omega) = \frac{\hat{\underline{r}}\,\beta^2 e^{-i\,\omega r/\alpha}}{4\pi\,\alpha^3 r}\, R_p(\theta,\phi)\,\Omega_p(\theta,\phi,\omega),$$

$$\underline{u}^\beta (r,\theta,\phi,\omega) = \frac{e^{-i\,\omega r/\beta}}{4\pi\,\beta r}\,[\hat{\underline{\theta}}R_{s\theta}(\theta,\phi) \tag{19}$$

$$+\ \hat{\underline{\phi}}R_{s\phi}(\theta,\phi)]\,\Omega_s(\theta,\phi,\omega),$$

where R_p, $R_{s\theta}$, and $R_{s\phi}$ are the double couple radiation pattern components. They are given in terms of $\hat{\underline{n}}$, $\hat{\underline{e}}$ and $\hat{\underline{r}}$, the unit vectors in the directions of the fault normal, slip direction, and source-receiver direction, respectively, by

$$R_p = \hat{\underline{r}}\,\hat{\underline{r}} : (\hat{\underline{n}}\,\hat{\underline{e}} + \hat{\underline{e}}\,\hat{\underline{n}}),$$

$$R_{s\theta} = \hat{\underline{\theta}}\,\hat{\underline{r}} : (\hat{\underline{n}}\,\hat{\underline{e}} + \hat{\underline{e}}\,\hat{\underline{n}}), \tag{20}$$

$$R_{s\phi} = \hat{\underline{\phi}}\,\hat{\underline{r}} : (\hat{\underline{n}}\,\hat{\underline{e}} + \hat{\underline{e}}\,\hat{\underline{n}}) .$$

For the problem geometry of Figure 11, these factors are

$$R_p = \sin 2\theta\,\sin\phi,$$

$$R_{s\theta} = \cos 2\theta\,\sin\phi, \tag{21}$$

$$R_{s\phi} = \cos\theta\,\cos\phi .$$

The Ω_p and Ω_s are obtained directly from a three-dimensional Fourier transform (the "angular spectrum" (Bracewell, 1965)) of the slip velocity function. Taking x_o, y_o to be Cartesian coordinates describing the fault plane, and denoting the velocity discontinuity across the fault by $\hat{e}\,\dot{s}\,(x_o,y_o,t)$, Ω_p and Ω_s are given by

56

$$\Omega_p(\theta,\phi,\omega) = \int\!\!\!\int\!\!\!\int_{-\infty}^{\infty} dx_o dy_o dt\; \dot{s}(x_o,y_o,t)e^{i(K_x x_o + K_y y_o - \omega t)}\left|\begin{array}{l} K_x = \dfrac{\omega}{\alpha}\sin\theta\,\cos\phi \\[2mm] K_y = \dfrac{\omega}{\alpha}\sin\theta\,\sin\phi \end{array}\right.$$

$$(22a)$$

$$\Omega_s(\theta,\phi,\omega) = \int\!\!\!\int\!\!\!\int_{-\infty}^{\infty} dx_o dy_o dt\; \dot{s}(x_o,y_o,t)e^{i(K_x x_o + K_y y_o - \omega t)}\left|\begin{array}{l} K_x = \dfrac{\omega}{\beta}\sin\theta\,\cos\phi \\[2mm] K_y = \dfrac{\omega}{\beta}\sin\theta\,\sin\phi \end{array}\right.$$

$$(22b)$$

Equations (22a) and (22b) contain all the dependence
of the radiation on the finite difference solution. Thus, it
is only necessary to store the computed slip velocity at all
nodes on the fault plane, and it is only necessary to com-
pute the finite difference solution until the fault has every-
where healed. Given this slip velocity function, Equations
(22a) and (22b) require a single three-dimensional Fourier
transform be performed. Then Ω_p (or Ω_s) as a function of ω,
for any given θ,ϕ, is obtained by assembling the Fourier
transform values along a line through K_x, K_y, ω space.
Equation (19) then gives the P and S wave spectra.

Since $\dot{s}$ is known from the finite difference solution
at discrete points, it is natural to employ an FFT algorithm
to execute the three-dimensional transform. The application
is entirely straightforward and efficient. The only note
of caution concerns interpolation of the discrete transform.
For a given ω, determining Ω requires interpolating the K_x,
K_y dependence of the discrete transform. The finite difference
solution provides the series $s_{i,j,k}$, $i = 1,\ldots I$, $j = 1,\ldots J$,
$k = 1,\ldots K$, where I and J are the number of nodes in the x
and y directions, respectively, at which slip is non-zero,
and K is the number of time steps in the solution. Since the

57

function $\dot{s}$ is zero outside this interval, the appropriate K_x, K_y interpolation of the discrete transform is via convolution of the transform with a two-dimensional sinc function. This is, of course, best accomplished by extending the series $\dot{s}$ by adding zeros in the i and j directions. In practice it appears sufficient to add enough zeros to double the series length in these directions. For the applications presented in subsequent sections, the series were padded to four times their original length in both directions. Further interpolation in K_x, K_y can be done linearly without distortion of the solution.

3.5 VERIFICATION OF THE METHOD AND COMPARISON TO PREVIOUS WORK

The numerical procedures involved in solving the non-linear boundary value problem (Sections 3.2 and 3.3) and analytically continuing the resultant seismic field (Section 3.4) are sufficiently complex that a careful evaluation of their accuracy is warranted. The ideal verification approach would be to treat a simple case for which an exact analytic solution is available, then compare the analytic solution to the numerical solution. Unfortunately, no analytic solution exists for a three-dimensional problem in which a stress drop is specified on a propagating fault surface which ultimately stops growing and heals. In this section we compare our numerical solution for the elastic fault problem to a variety of available analytic and numerical results for similar problems. Then we check the internal consistency of the method by comparing the far-field pulses obtained from Fourier analysis of the slip function with those obtained from the spherical harmonic expansion of the outgoing elastic field.

3.5.1 Kostrov's Analytical Solution

Kostrov (1964) obtained an analytical solution for the problem of a circular crack which nucleates at a point in a

58

homogeneous, unbounded elastic medium and expands at a constant rupture velocity without stopping. His solution for the displacement discontinuity across the crack is

$$s = C \, \frac{\sigma_e}{\mu} \, \beta \sqrt{t^2 - \frac{r^2}{V_R^2}} \quad H \left(t - \frac{r}{V_R} \right) , \qquad (23)$$

where C is a constant which depends on rupture velocity (see Dahlen, 1974), σ_e is the excess of the prestress over the kinetic frictional stress, μ is the shear modulus, β is the shear wave speed, r is distance from the hypocenter, and V_R is the rupture propagation velocity. This problem corresponds exactly to the condition of the elastic model considered in this study, until time a/V_R, where a is the half-length of the square fault. In this case a = 1.5 km and V_R is 3.08 km/sec (0.9β), for which C equals approximately 0.81. We shall compare the initial fault slip, obtained numerically, to Kostrov's analytic solution. Once the rupture front reaches the edge of the square fault plane and stops growing, we expect the numerical solution to begin to deviate significantly from Kostrov's solution.

Figure 12 shows the slip obtained at several points in the fault plane. The dashed curves are the finite difference solution and the solid curves are the analytic solution. The vertical bars indicate the arrival times of edge effects due to stopping of the rupture at its outer boundary. The two solutions display the anticipated agreement at each point prior to the arrival of the edge effects. The small deviation of the numerical solution from the analytic solution at early time results, at least partially, from imprecise weighting of the stress drop to account for the fractional rupture of a finite difference zone by the circular rupture front. Archuleta and Frazier (1978) achieved somewhat better agreement with Kostrov's solution by incorporating fractional rupture into their finite element scheme.
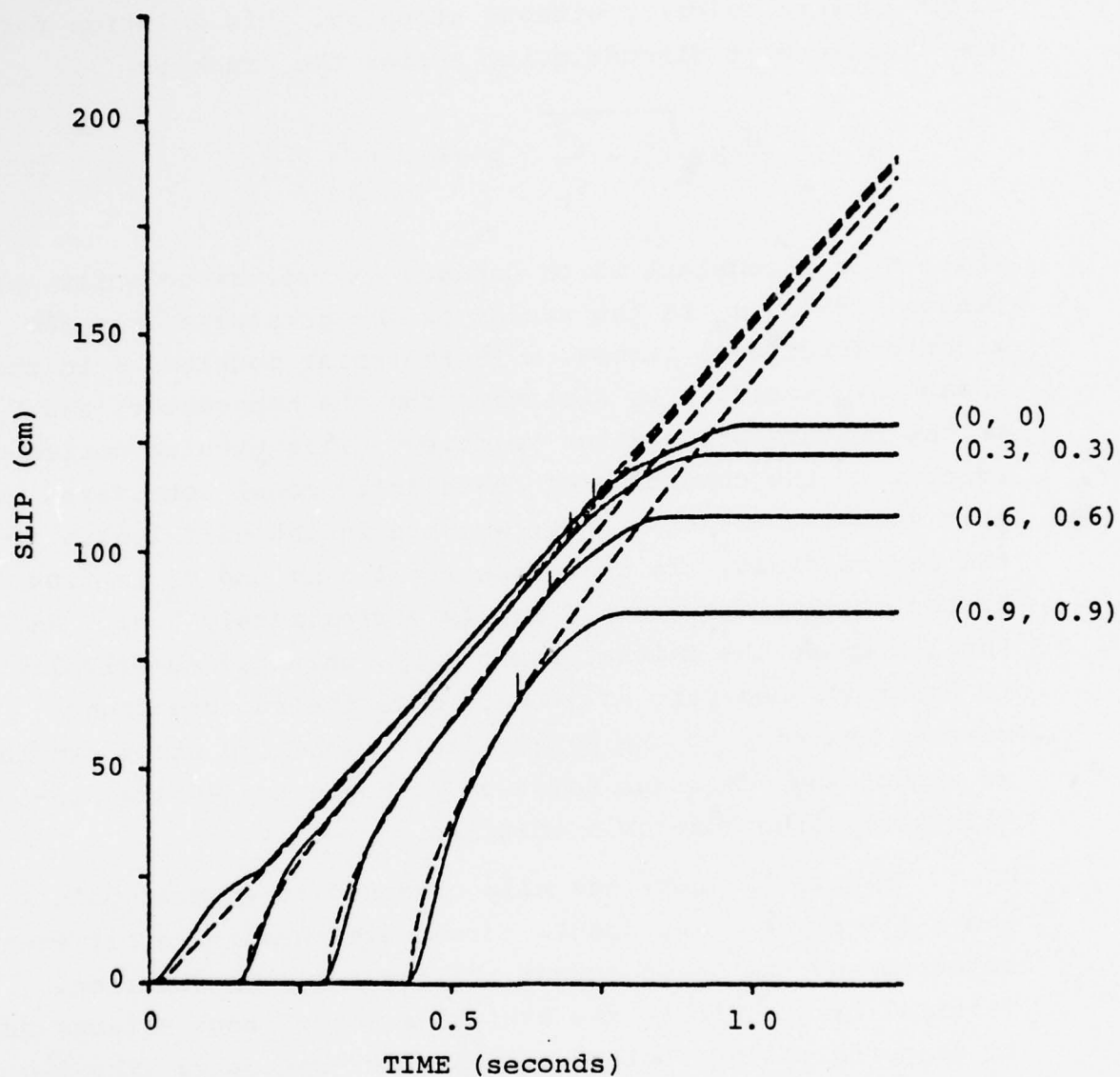
59

Figure 12. Relative displacement on the fault for the elastic case. The dashed curves are Kostrov's analytic solution; the solid curves are the finite difference results. x,y coordinates in kilometers are given in parenthesis. Vertical lines indicate the arrival times of edge effects due to fault finiteness.

3.5.2 The Stopping Phase

Once edge effects occur, we have to rely on other numerical solutions for comparison. The problem of a finite circular fault has been solved by Madariaga (1976) using a finite difference method. There are several features characterizing his solution. When the fault stops growing, slip velocity at a given point on the fault begins to deviate from Kostrov's solution at a time corresponding to the P travel time to that point from the nearest edge of the fault. Thus, a stopping phase propagates radially inward at the P wave speed. The subsequent arrest of slip also initiates at the outer edge and propagates radially inward. The velocity of this healing "wave" is not constant, but its average is near the shear wave velocity.

Although we are dealing with a square fault edge, similar behavior is expected since rupture growth is circular and our final fault geometry is similar. Figure 12 shows the stopping phase for points on the square fault. The stopping behavior is very similar to that of the circular fault, in spite of the reduced symmetry in the problem (the circular fault stops everywhere on its perimeter simultaneously, whereas the square fault does not). We also note that t e displacement curve for the point at the hypocenter differs from those for other points in the fault plane in that it has two distinct breaks in slope associated with stopping. This feature has been observed in several numerical studies of circular shear cracks (Archuleta, 1976; Madariaga, 1976; Day, 1977).

3.5.3 Static Configuration

Neuber (1937) solved the static problem of the displacement of an elastic whole space due to a uniform shear stress drop on a circular crack and obtained the slip distribution

61

$$s(r) = \frac{24}{7\pi} \frac{\Delta\sigma}{\mu} b \sqrt{1 - \frac{r^2}{b^2}} \, , \tag{24}$$

where s is the relative displacement on the fault, $\Delta\sigma$ is the stress drop, μ the shear modulus, b the fault radius and r distance from the fault center. From Equation (24) we find that the average slip $\bar{s}$ is 2/3 the slip at the center of the fault. However, numerical solutions to the corresponding dynamic problem give a maximum and average static slip approximately 25 percent greater than Equation (24), for the case in which rupture velocity is 0.9 (interpreting $\Delta\sigma$ as the difference between prestress and kinetic frictional stress). For example, Madariaga (1976) found a slip function 20 percent in excess of Equation (24), and Archuleta (1976) and Day (1977) found a 27 percent overshoot. The failure of the dynamic solutions to approach the static solution is, of course, a consequence of the non-linearity of the boundary conditions (i.e., the healing of the fault).

From the square fault, we obtained a maximum residual slip of 129 cm, which occurred at the center of the fault. If we reinterpret b in Equation (24) as $\sqrt{A/\pi}$, where A is the fault area, then 129 cm exceeds the prediction of Equation (24) by a factor of 1.24, in good agreement with numerical results for the circular fault. The average slip for the square fault was 79 cm, which is 0.61 times the value of the center. The seismic moment obtained from this average slip was 2.28×10^{24} dyne-cm. This value is 14 percent greater than the prediction obtained by combining the static crack formula, Equation (24), with the expression for seismic moment, $M_o = \mu A \bar{s}$.

3.5.4 Computation of the Radiated Field

As a check on the internal consistency of the analysis procedure, we compute far-field displacement spectra and pulses

for the elastic problem by two different methods. Spectra and pulses obtained from the angular spectrum of the slip function are compared to those obtained from spherical harmonic expansions of the divergence and the Cartesian components of the curl, evaluated on a sphere of 2.7 km radius. Of particular interest is the convergence rate of the spherical harmonic expansion, since we will rely on this technique alone to obtain the radiation for the plastic crack problem.

Figure 13 compares four determinations of the far-field S wave spectrum and time pulses for the elastic fault model, observed at $\theta = 0°$. The dashed curves represent the spectrum and pulse obtained by Fourier analysis of the slip function. The other three sets of curves were obtained by truncating the spherical harmonic series at $\ell = 4, 6$, and 8, respectively. The curves have been normalized by the zero-frequency level $M_o (4\pi\rho\beta^3 r)^{-1}$, where M_o is the seismic moment obtained from the average static slip $\bar{s}$:

$$M_o = \mu A \bar{s} . \tag{25}$$

As the figure indicates, the spherical harmonic expansion converges rapidly at low frequency. For frequencies above 1 to 2 Hz, however, the truncated series can be significantly in error. For example, at 3 Hz the spectrum obtained by truncating the series at $\ell = 6$ is in error (relative to the spectrum obtained from the slip function) by a factor of 4. Including terms up to $\ell = 8$ reduces the error to a factor of 1.5 (the maximum frequency for which the finite difference solution is reliable is approximately 4 to 5 Hz).

Figure 14 compares far-field pulses and spectra at 3 azimuths; the dashed curves were obtained from the slip function, the solid curves from the expansion in spherical harmonics up to order 8. For computing far-field solutions in the range 0-3 Hz, the spherical harmonic expansion, truncated at $\ell = 8$ appears to be satisfactory.
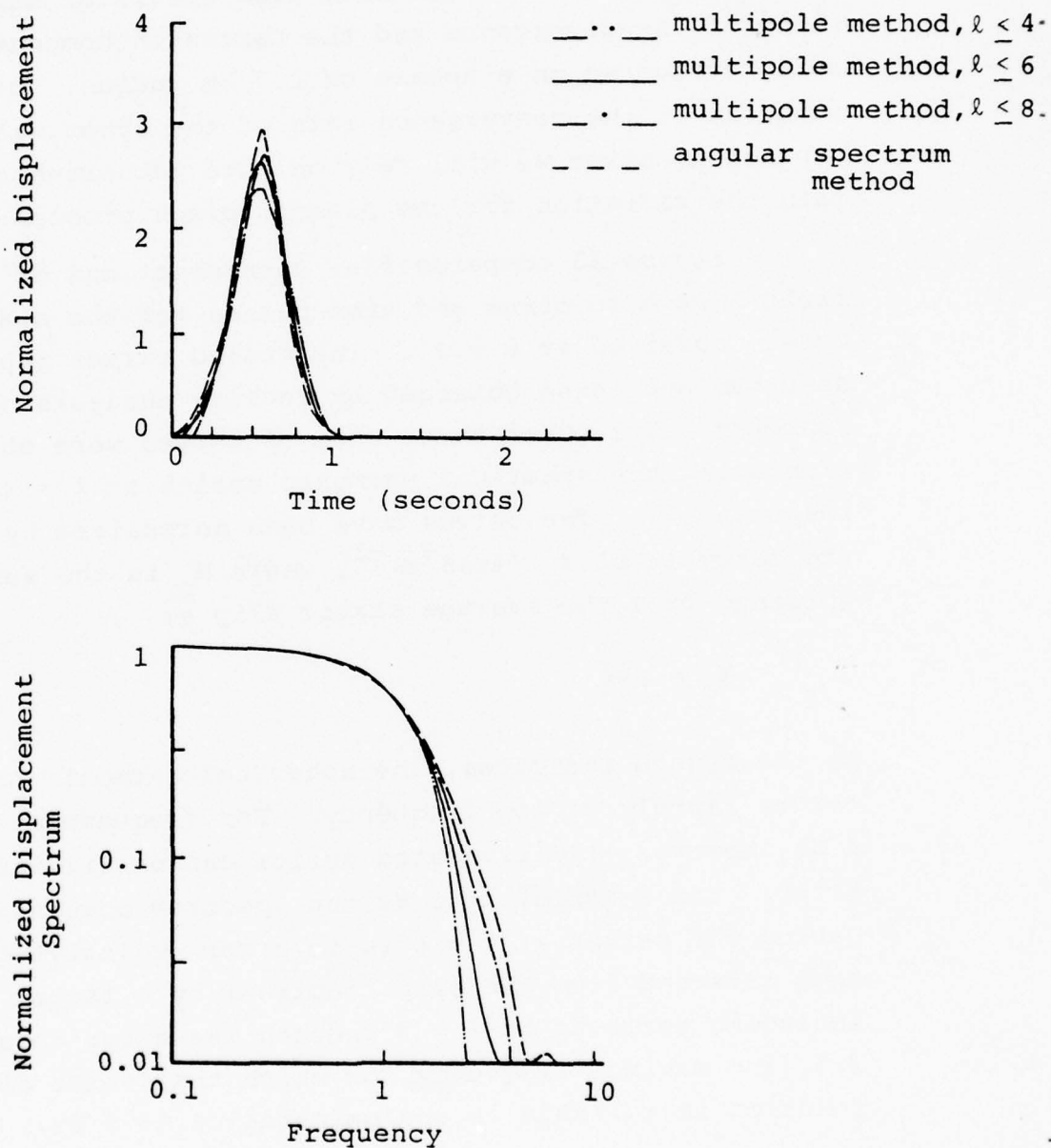
63

Figure 13. Comparison of four determinations of the far-field
S wave spectrum and time history, for the elastic
fault model, observed at $\theta = 0$. The normalization
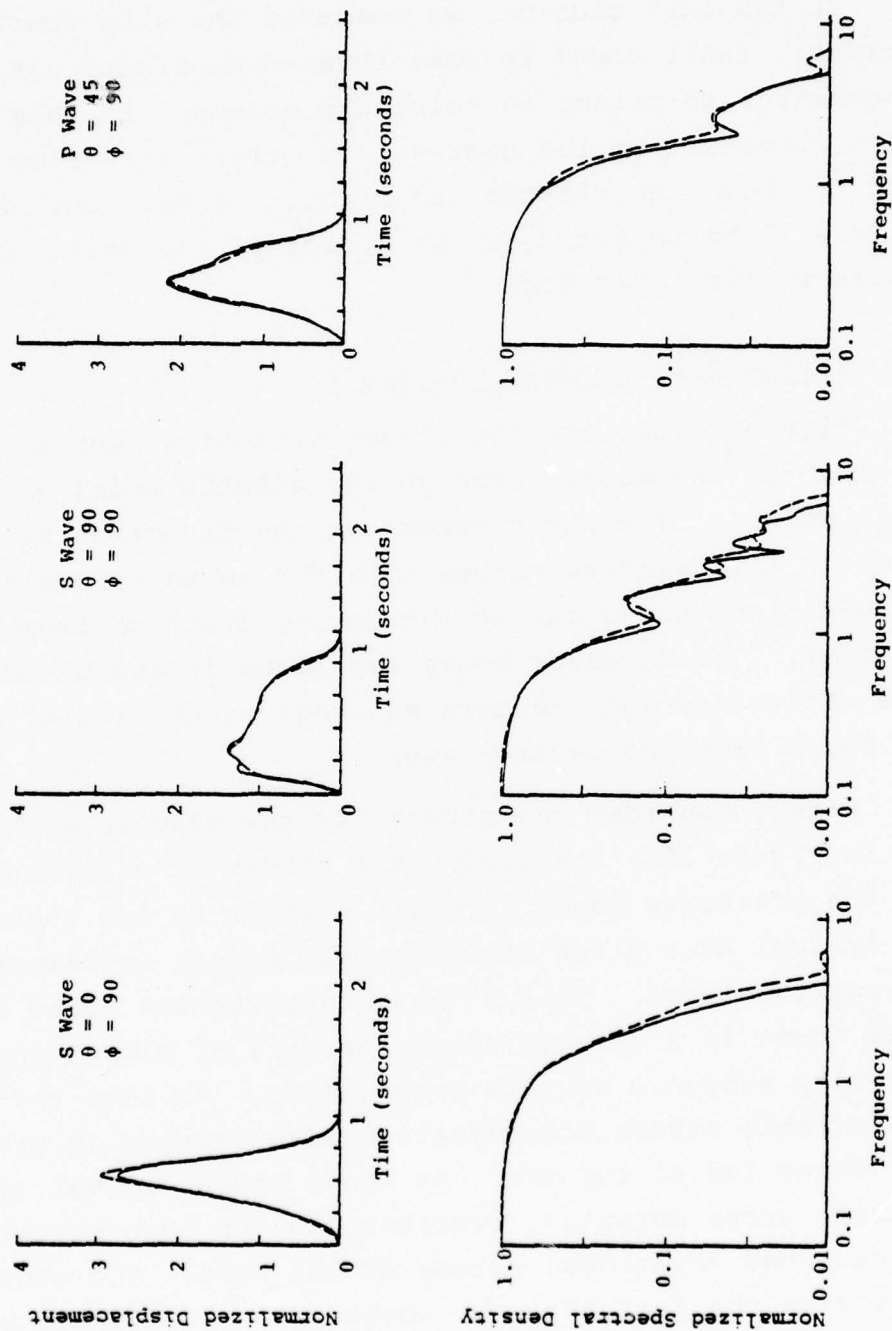is described in the text.

Figure 14. Far-field time histories and spectra at 3 azimuths. The dashed curves were obtained by the angular spectrum method, the solid curves by the multipole expansion method using terms up to order $\ell = 8$. The normalization is described in the text.

65

3.6   NEAR-SOURCE DEFORMATION

In the last section, we compared the slip function for the elastic fault model to some three-dimensional analytical and numerical solutions to related problems. In this section, we look in detail at the near-source stress and velocity fields for both the elastic and plastic cases. Our main objective will be to evaluate the effect of inelastic material response in the fault zone.

3.6.1 Stress History Near the Fault

Figure 15 depicts the stress histories near the fault plane for the two models (the purely elastic model and the plastic model). The shear stress in the direction of pre-stress (σ_{yz}) is plotted versus time for seven points along the fault plane diagonal, at increasing distance from the hypocenter. The stresses shown are actually evaluated at the finite difference zone centers adjacent to the fault, which are 0.05 km from the fault plane.

First, consider the stress for the elastic problem shown in Figure 15. Initially, the stress at a given point is at the prestress level (1 kbar). Prior to the rupture front arrival at a given location, the stress increases above the prestress level. This stress concentration ahead of the rupture front is a general characteristic of elastodynamic cracks with subsonic rupture propagation. We note the amplifi-cation of this stress concentration with increasing distance in the direction of rupture. At the rupture arrival time, the stress drops abruptly, overshooting and then settling at the prescribed frictional stress of 820 bars. The overshoot results from the fact that the observation points are slightly removed from the fault plane itself. The same phenomenon is present in Richard's (1976) analysis of the self-similar ex-panding crack. The stress then remains at the frictional
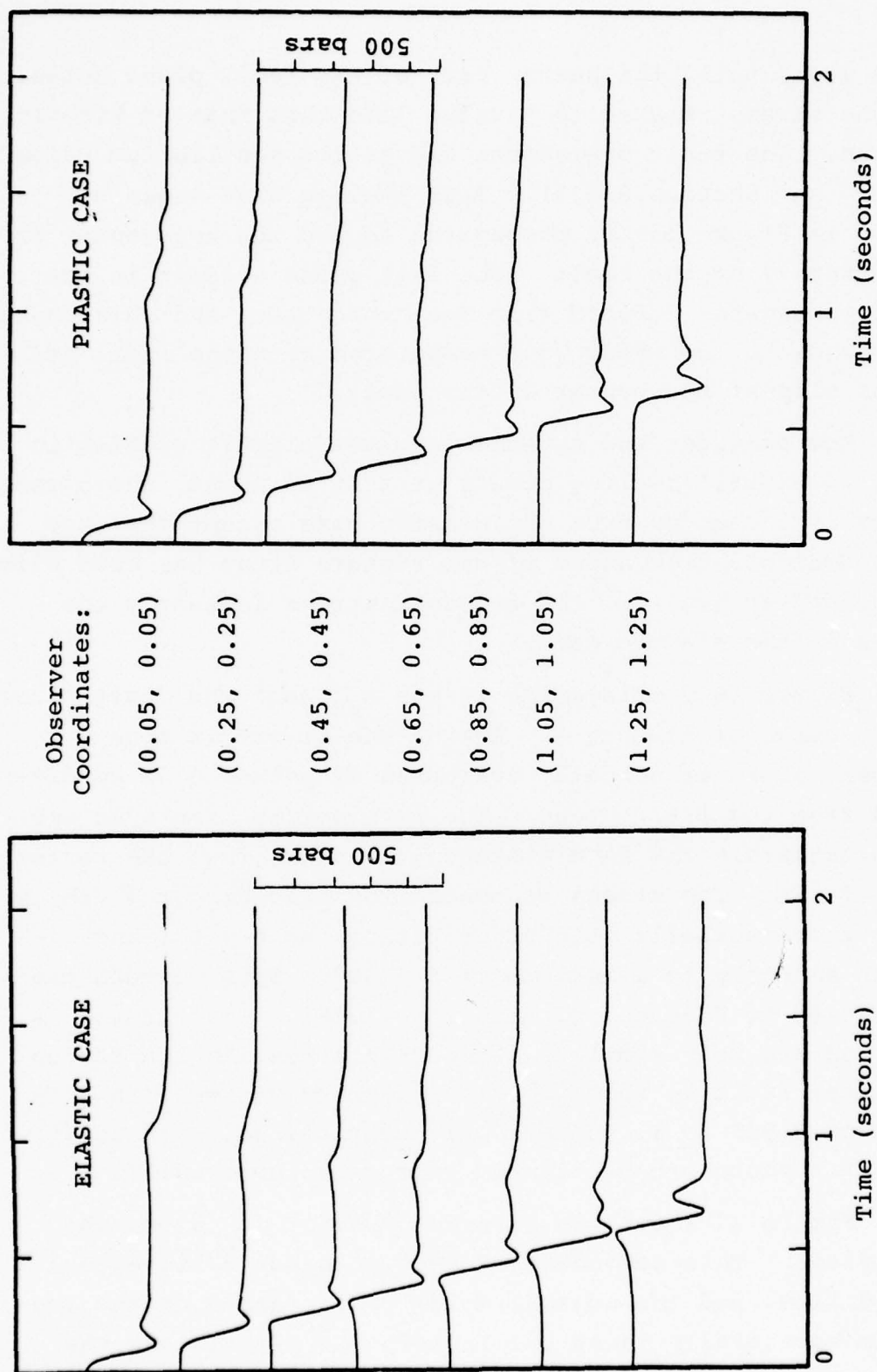
66

Figure 15. Time histories for the stress component σ_{yz} adjacent to the fault plane, for several hypocentral distances. Observation points are at a distance of 0.05 km from the fault plane; x and y coordinates are shown in parentheses.

67

stress level until the nearby part of the fault plane heals. Then the stress relaxes to a value less than that of kinetic friction. The fault overshoots the static equilibrium value of slip (see Section 3.5.3). This healing wave shows up clearly in Figure 15; it propagates toward the hypocenter from the periphery of the fault. The last phase evident in the figure propagates outward from the hypocenter, and this phase corresponds to the shear wave associated with the final arrest of slip at the center of the fault.

Now consider the stresses for the plastic problem in Figure 15. Until healing occurs at a given point, the stress history is unchanged from the elastic case except that the stress concentration ahead of the rupture front has been eliminated. After healing, the residual stress is nearly the same as in the elastic case.

Figure 16 displays the stress σ_{yz} near the fault plane as a function of azimuth ϕ. Again, the stress is zone centered, so it is actually evaluated at points 0.05 km displaced from the fault plane. The five points displayed are at approximately the same distance, 1.15 km, from the center of the fault. The stress concentration preceding rupture is nearly zero (actually slightly negative) at $\phi = 0°$, and increases smoothly to a maximum of $\phi = 90°$. This pattern can be compared to Figure 8 of Richards (1976). The stress histories are very similar, although his results are for an ellipitcal fault in which rupture velocity varies with azimuth from 0.92β to β, whereas our numerical solution is for circular rupture propagation at rupture velocity 0.9β.

Figure 17 shows the stress component σ_{yy} along the fault plane. This component of stress is not relieved by plastic flow, and the concentration of σ_{yy} ahead of the rupture is essentially identical in both the plastic and the elastic cases.
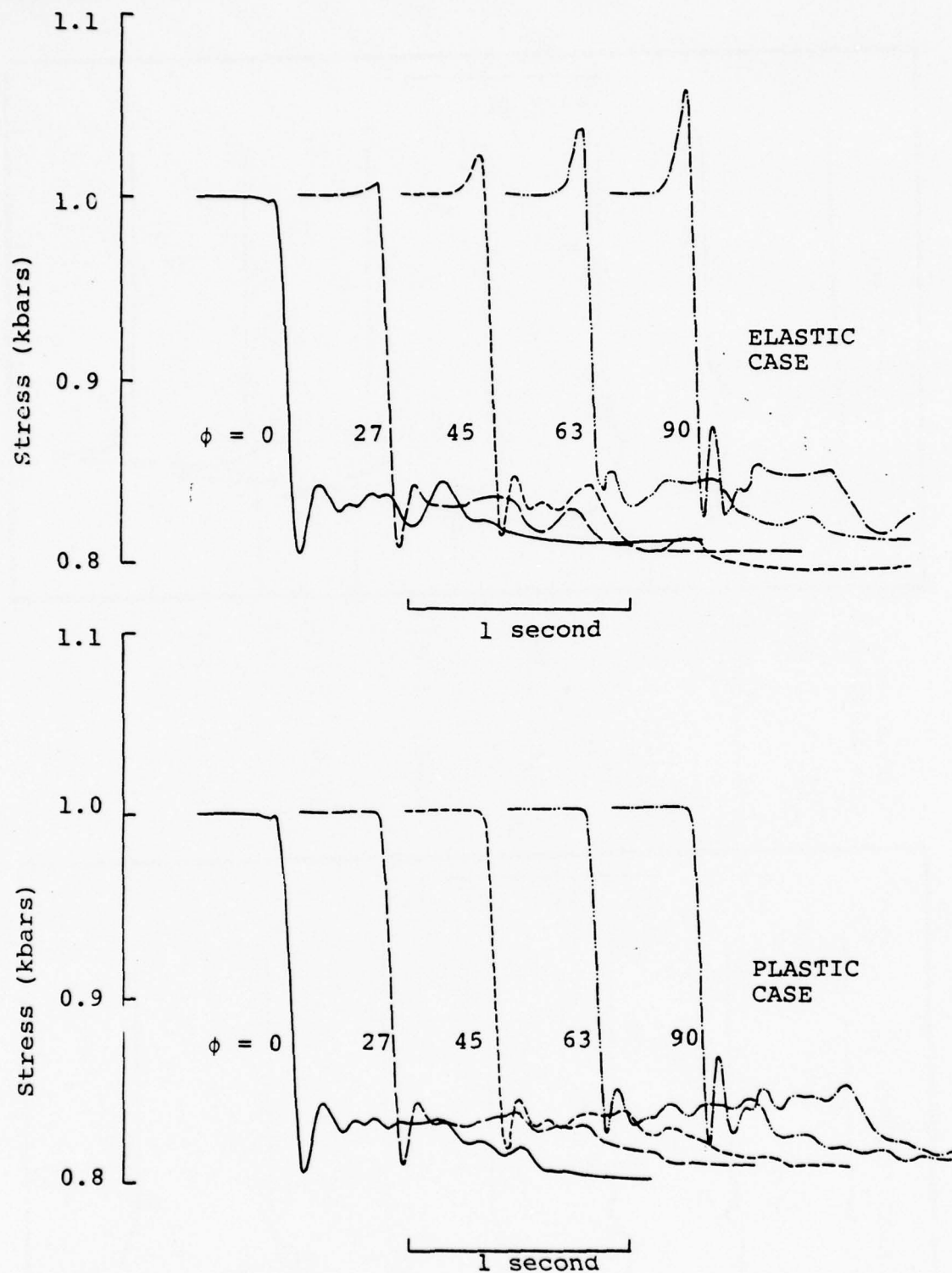
68

Figure 16. Time history of σ_{yz} adjacent to the fault plane for several azimuthal angles ϕ. Each observation point is at a distance of 0.05 km from the fault plane, and a distance 1.15 km from the center of the fault.
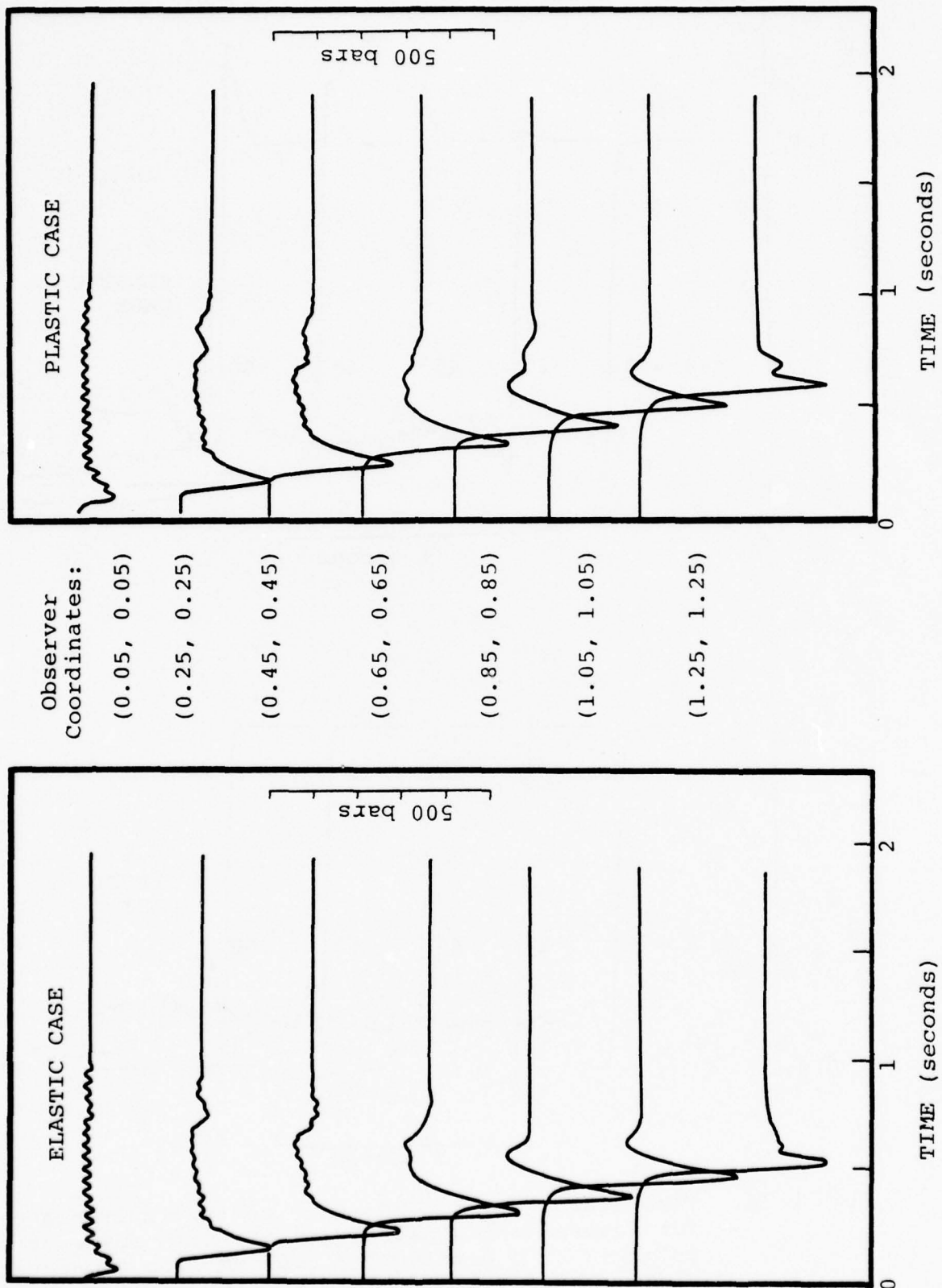
Figure 17. Time history of σ_{yy} along the fault plane. Observation points are as in Figure 15.

70

3.6.2 Particle Velocity on the Fault

Figure 18 shows the particle velocity obtained on the fault plane at increasing distances from the hypocenter along a radial line. The solid curves are for the elastic case, the dashed curves are for the plastic case.

It is evident from Figure 18 that the initial velocity is strongly peaked and the peak value increases with hypocentral distance. We can understand this characteristic of the velocity curves by means of Kostrov's analytic solution, Equation (23). This expression implies a velocity proportional to $t(t^2 - r^2/v_R^2)^{-1/2}$, which is singular at the rupture arrival time (except at the hypocenter $r = 0$). Since a finite difference grid is essentially a low-pass filter, we expect the peak velocities in Figure 18 to be a filtered version of the analytic solution. To approximate the filtering effect of the grid on peak velocity, we find $\tilde{v}$, the average of the velocity over a short time T following the rupture arrival:

$$\tilde{v} = C \frac{\sigma_e}{\mu} \frac{\beta}{T} \int_{\frac{r}{v_R}}^{\frac{r}{v_R} + T} t \left(t^2 - \frac{r^2}{v_R^2}\right)^{-1/2} dt \qquad (26)$$

$$= C \frac{\sigma_e}{\mu} \beta \, T^{-1/2} \left(2 \frac{r}{v_R} + T\right)^{1/2}$$

which, for $r/v_R \gg T/2$ is proportional to $r^{1/2}$. That is, we expect peak velocity to increase as the square root of distance in the direction of rupture. The peak velocities in Figure 19 are in good agreement with Equation (26) if T is assumed to be approximately 0.05 seconds (ten times steps).

71

It is evident from Figure 18 that the initial part of the particle velocity is unaffected by the introduction of plasticity, within the resolution of the finite difference calculation. A large velocity peak occurs at the crack tip, even in the absence of the strong stress concentration associated with the purely elastic problem. The plastic and elastic solutions are indistinguishable until the arrival of the stopping phase.

It is informative to compare this result with Ida's (1972, 1973) analytic study of propagating cracks. That study was an elastodynamic analysis, but finite material strength at the crack tip was modeled by introducing a distribution of "cohesive stress" across the crack which opposes the slip. This approach truncates the shear stress concentration at the crack tip, and in this respect simulates the plastic flow model used here. The spatial distribution of the cohesive stress must be assumed a priori, however. Ida (1973) gives an approximate expression for the peak particle velocity:

$$\dot{U}_{peak} \sim D \frac{\sigma_o}{\mu} V_R , \qquad (27)$$

where V_R is rupture velocity, σ_o is the excess of rock strength over sliding friction. The D is a constant which was found to be about one from numerical experiments with different assumed distributions of cohesive stress. For our plastic crack model, σ_o is 180 bars, V_R is about 3 km/sec, and μ is about 3×10^5 bars, so Equation (27) would suggest a value of about 180 cm/sec for peak velocity. In contrast, the peak velocity for the finite difference solution is twice this value and is a lower limit due to the filtering effect of the grid.

The discrepancy is due to the fact that Ida found D to be of order 1 by considering smoothly varying cohesive
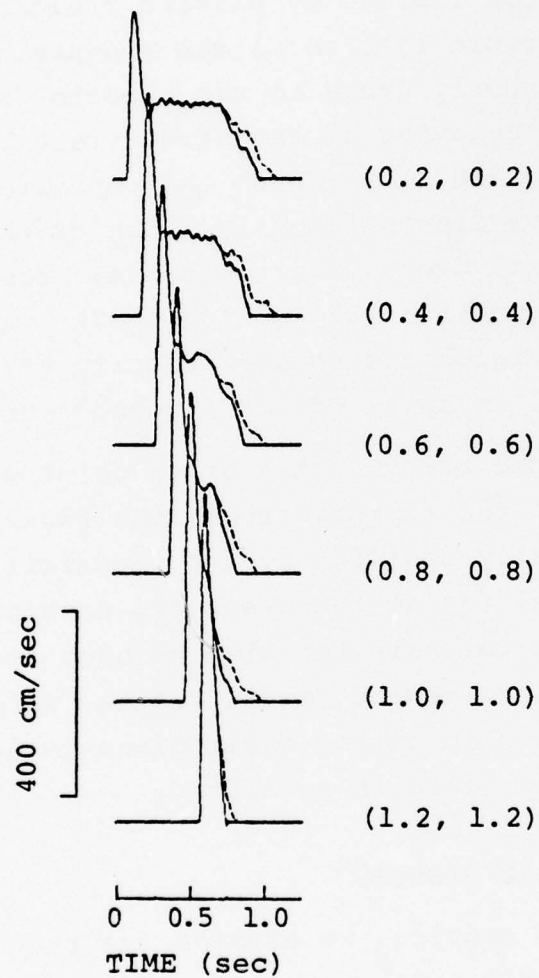
72

Figure 18. Slip velocity in the fault plane. Solid
lines are the elastic case, dashed lines
the elastoplastic case. x,y coordinates
in kilometers are shown in parenthesis.

stress distributions. In the current plastic model, crack tip stresses are limited by plastic yielding to essentially a constant (Figure 15), until the rupture arrival time. Then the stress abruptly drops to the kinetic friction level. This discontinuous behavior of the stress resembles a special case treated by Ida (1972) in which the cohesive stress was assumed to behave discontinuously. The crack tip stress was assumed constant over a short interval, then dropped abruptly to zero. As Equation (22) of Ida (1972) indicates, this special case yields a singular velocity at the point of stress discontinuity, in spite of the imposed finiteness of stress.

After the arrival at a given point of edge effects due to stopping of the rupture front, the fault plane velocities are substantially modified by the plasticity. As Figure 18 indicates, yielding at the crack tip smooths the stopping phase, robbing the slip function of high frequencies and increasing the long-period content of the slip function. The average static slip on the fault plane is increased by about 11 percent when yield is permitted.

3.7   FAR-FIELD RESULTS

In this section, we examine the radiated seismic field for the two fault models. Far-field displacement spectra and time histories are given for P and S waves. The far-field solutions were obtained from the multipolar expansions (Section 4), using terms up to $\ell = 8$.

3.7.1 Elastic Case

Figures 19 and 20 present normalized far-field P and S wave displacement spectra and time histories for the elastic case. Results are shown at 10° intervals in θ; Figure 19 is for $\phi = 90°$, and Figure 20 is for $\phi = 45°$. Solid lines are the P wave displacements, dashed lines are the S wave ones.
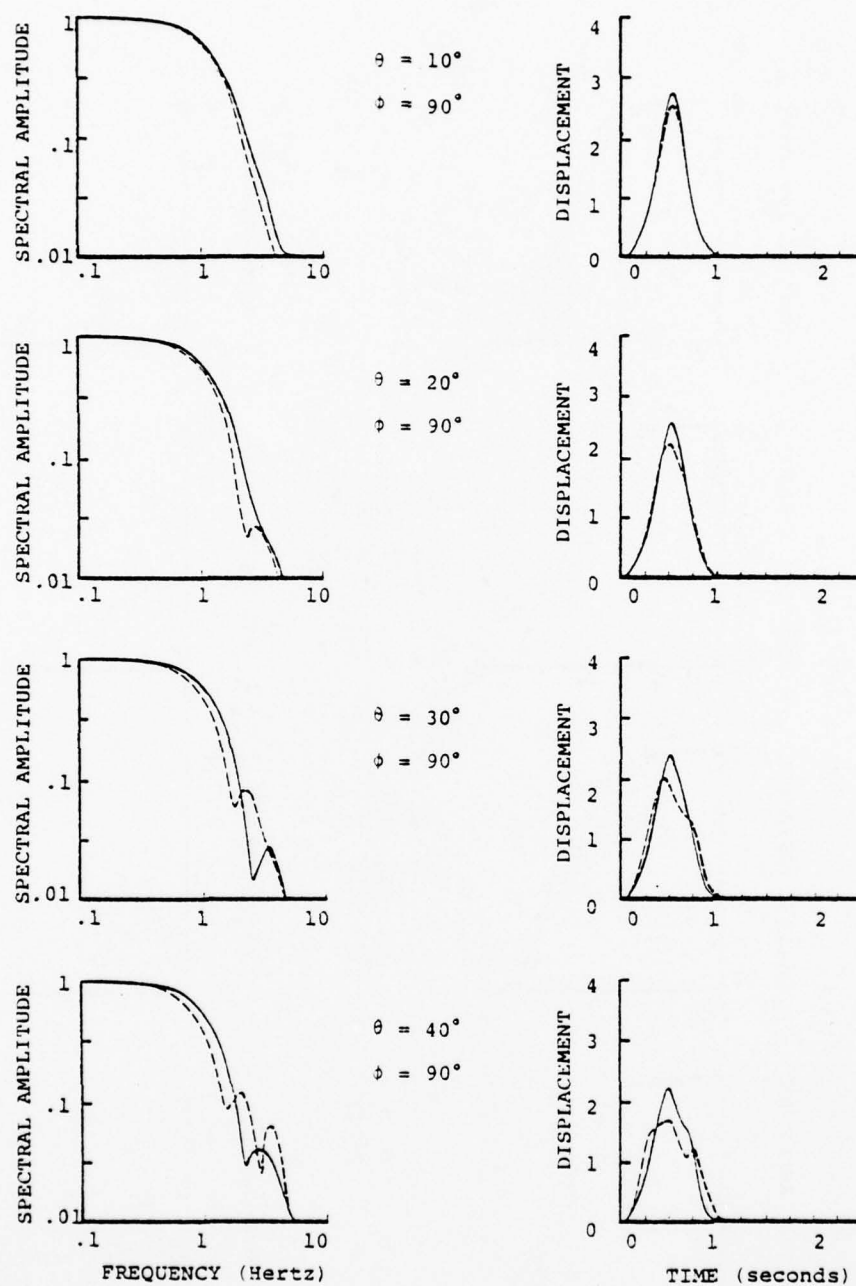
74

Figure 19. Normalized far-field P wave (solid curves) and S wave (dashed curves) displacement spectra and time histories. Displacements are shown at 10° intervals in θ, for φ = 90°.
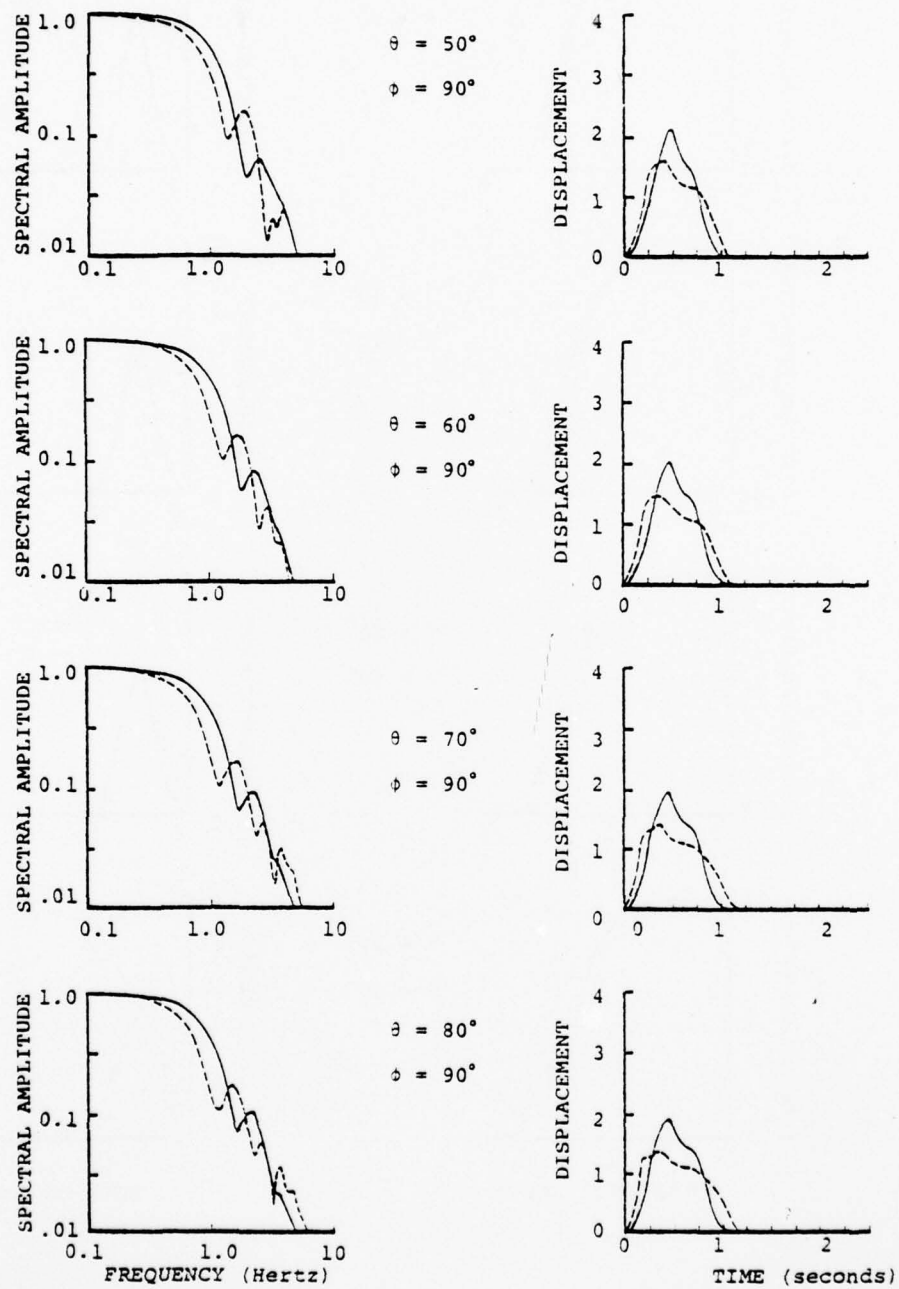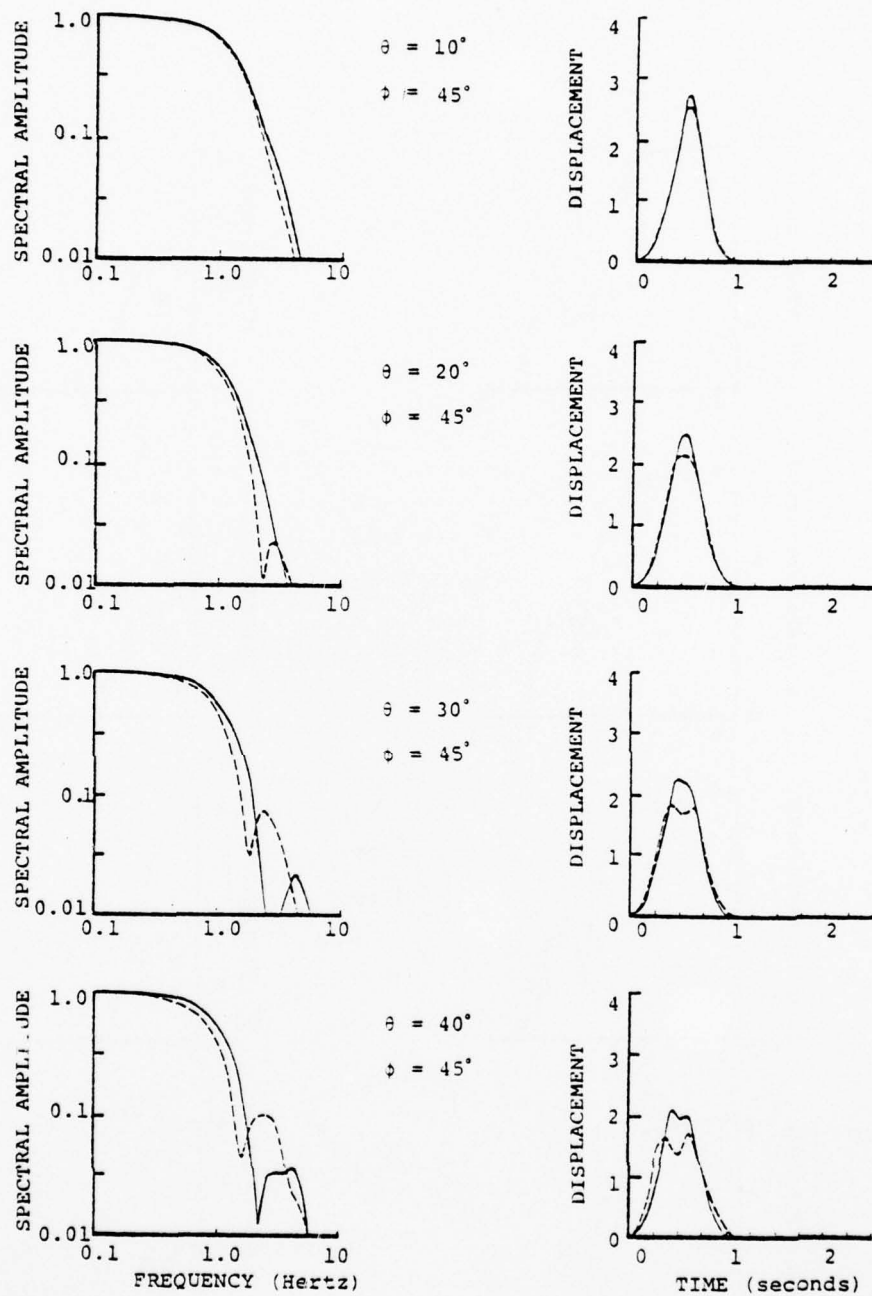
75

Figure 19. Concluded

Figure 20. Normalized far-field wave (solid curves) and S wave (dashed curves) displacement spectra and time histories. Displacements are shown at 10° intervals in θ, for φ = 45°.
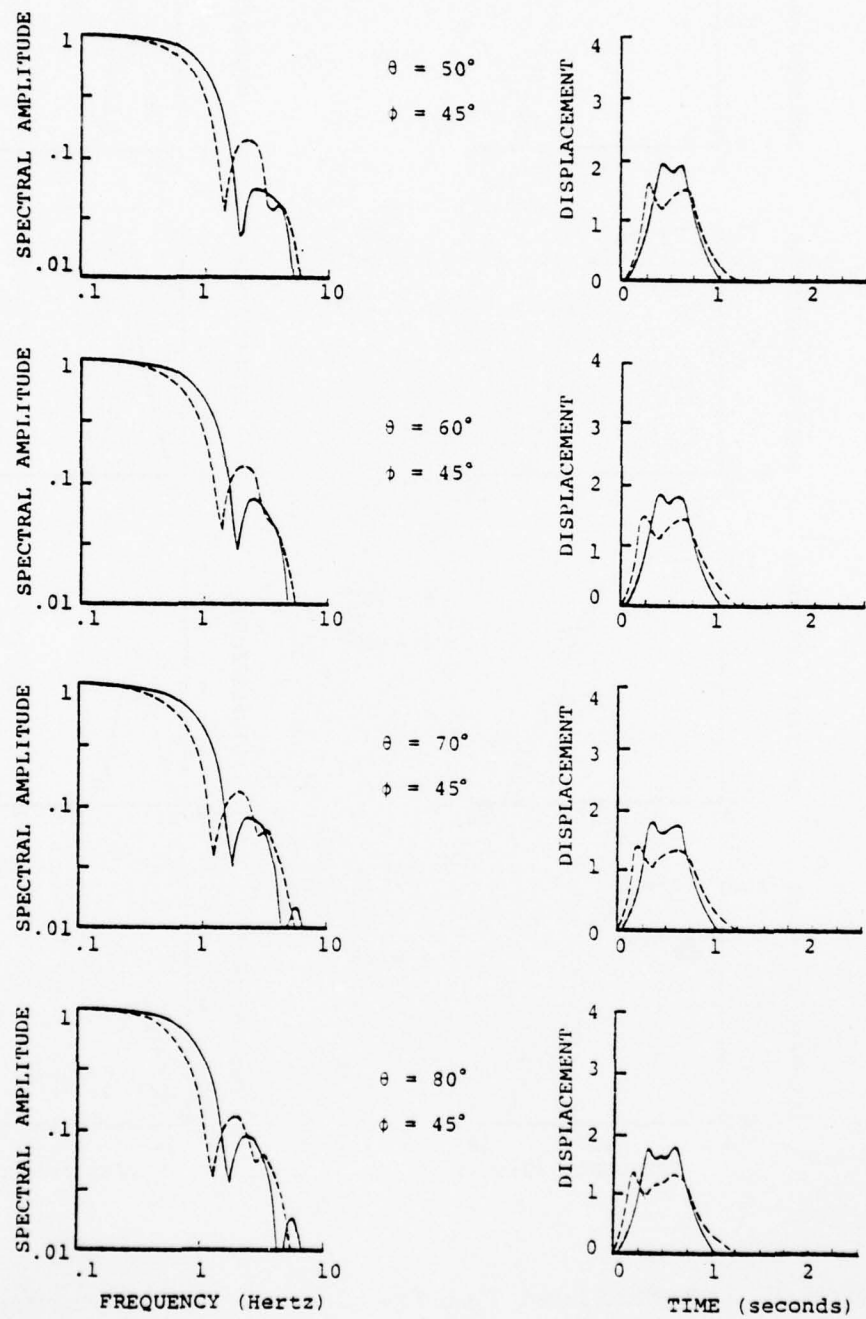
77

Figure 20. Concluded

The curves are normalized by the zero frequency spectral amplitude, derived from the average slip $\tilde{s}$. For P waves, the normlization is $\mu A\tilde{s} \ (4\pi\rho\alpha^3 r)^{-1}R_p$. For S waves, we can interpret the curves either as the θ component of displacement normalized by $\mu A\tilde{s} \ (4\pi\rho\beta^3 r)^{-1}R_{s\theta}$, or as the ϕ component of displacement normalized by $\mu A\tilde{s} \ (4\pi\rho\beta^3 r)^{-1}R_{s\phi}$. The travel times from hypocenter to receiver have been removed from the P and S time histories.

Comparing results at $\phi = 90°$ with those at $\phi = 45°$, we note that pulse width and corner frequency have practically no dependence on ϕ; at higher frequency there is some difference in spectral and time domain detail between the two azimuths. (Results at $\phi = 0°$ are virtually identical to those at $\phi = 90°$, and are now shown.)

Dependence of pulse width and corner frequency on θ and on wave type (P or S) is significant. Our observations concur with those of Madariaga (1976):

(a) S wave corner frequencies are smaller than P wave corner frequencies, except near $\theta = 0°$.

(b) Pulse width and corner frequency are governed by the travel time difference between stopping phases from the near and far edges of the fault. Thus, pulse width increases with θ, being greatest for observers near the plane of the fault and smallest for observers near the fault normal.

(C) P and S wave corner frequencies, for $\theta > 30°$, are expressed very well by Madariaga's Equation (24), replacing the circular fault radius with the square fault-width.

3.7.2 Plastic Case

The average static slip for the plastic fault problem is 88 cm, which exceeds the average slip in the elastic case by 11 percent. This results from the smoothing of the stopping caused by yielding at the fault edge. Actually, this is

79

precisely the percentage increase that would be predicted by
simple scaling of the elastic problem for a fault dimension
occupying the entire length and width of the plastic zone
(the plastic zone extended 0.2 km beyond edge of the fault).

The seismic moment for the plastic problem cannot be
obtained from the slip function, since the plastic deforma-
tion beyond the fault edge contributes to the low-frequency
spectrum of the radiated field. Therefore, we derive the
seismic moment from the zero-frequency limit of the radiated
field, obtained from the multipoles. This gives a seismic
moment of 3.15×10^{24} dyne-cm, which is 38 percent larger
than the moment for the elastic case. Scaling of the elastic
solution as suggested in the last paragraph would predict a
slightly larger increase in moment, 42 percent instead of 38
percent.

Figure 21 shows the effect of plastic yield on the
far-field displacements. Spectra and pulses are shown at
$\phi = 90°$ for three values of θ: S wave solutions are shown at
$\theta = 0°$ and $\theta = 90°$, and P wave solutions are shown at $\theta = 45°$.
Dashed curves are the elastic case, solid curves the plastic
case. In each case, the far-field solution is the sum of
multipolar terms up to $\ell = 8$.

The main influence of plastic yielding is to smooth
the stopping phases, with the result that the low-frequency
part of the spectrum is enhanced at the expense of the high
frequency part of the spectrum. Consider, for example, the
P wave pulse at $\theta = 45°$. Two stopping phases, corresponding
to rupture arrival at the near and far edges of the fault,
respectively, are apparent in the P wave displacement pulse
for the elastic problem. These appear as discontinuities in
slope occurring at about 0.46 seconds and 0.67 seconds. The
P wave pulse for the plastic problem coincides with that for
the elastic problem until the arrival of the first stopping
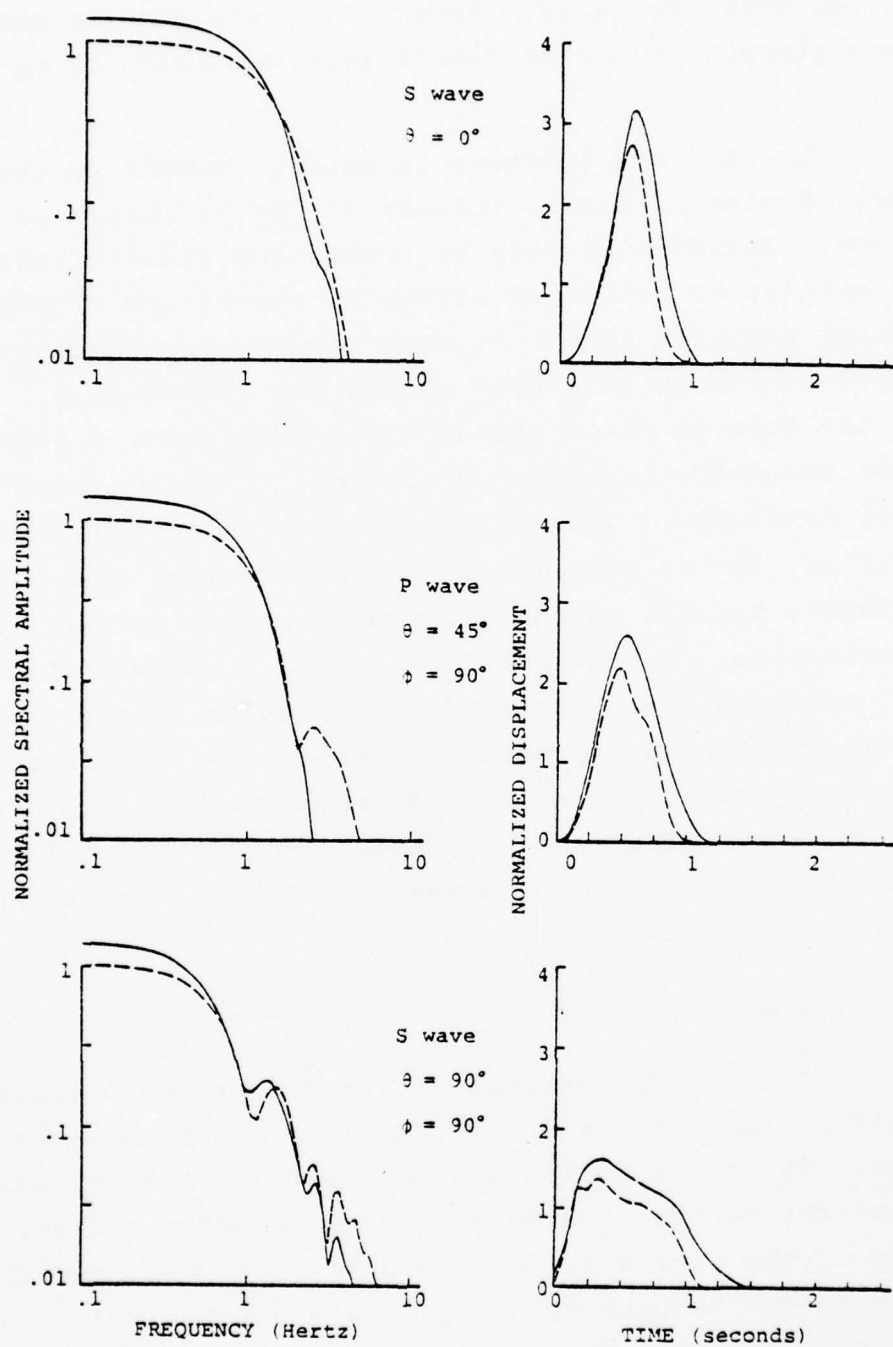phase. The displacement pulse for the plastic case then

80

Figure 21. Comparison of displacement spectra and time
histories from the plastic problem (solid curves)
with those from the elastic problem (dashed curbes).

81

reverses more gradually, overshooting the elastic case; the second stopping phase is almost imperceptible for the plastic case.

Clearly, the increase in seismic moment is the consequence of plastic strain induced at the periphery of the slip surface. Relieving stress by permitting plastic strain is very similar to relieving stress by permitting frictional sliding, but with the frictional stress approximately equal to $Y/\sqrt{3}$ (which in this case equals the prestress σ_T). Outside the zone in which yielding was permitted, a static shear stress concentration about 23 percent in excess of the prestress developed. Thus, if a larger plastic zone had been specified, the seismic moment would have been even greater, as plastic strains extended outward to eradicate the stress concentration. On the other hand, had a somewhat higher yield strength been specified, the results of the plastic problem would have approached those of the elastic case. If the yield parameter $Y/\sqrt{3}$ had exceeded the tectonic stress by $1.44\ (\sigma_T - \sigma_f)$ (that is, if Y had been 26 percent larger), no yielding would have occurred, and the two solutions would have been indistinguishable.

3.8   SUMMARY

Two three-dimensional finite difference calculations, simulating faulting in a uniform whole space, have been performed. The first calculation was for a linearly elastic medium; the second treated an elastic-plastic medium. Accuracy of the finite difference method has been verified by comparing the results to analytical and numerical solutions of crack problems. The far-field displacements associated with the finite difference simulations have been obtained using an elastodynamic representation theorem. This integral representation has been applied in two different forms and the far-field results compared.

82

An important objective was to evaluate the near-field and far-field effect of non-linear deformation in the fault zone. It was found that the initial portion of the slip time-function is unaffected by the admission of a simple form of plasticity. The large velocity peak at the crack tip, characteristic of elastic crack problems, persisted in the inelastic case. The stopping phase was modified somewhat, however. Yielding at the edge of the fault resulted in less abrupt stopping, reducing the high-frequency content of both the slip function and the far-field displacements, and increasing the average slip by 11 percent. Accumulation of plastic strain beyond the fault edge resulted in a 38 percent higher moment than in the elastic case.

These effects of plasticity depend upon our choice of the magnitude of prestress, the yield strength, the frictional stress, and the width of the non-linear zone. The problem treated was an extreme case in the sense that the prestress level everywhere equaled the strength of the medium $(Y/\sqrt{3})$. With a moderate increase in the yield strength (26 percent), or a similar decrease in the prestress, there would have been no yielding, and the solution would have been identical to that of the elastic problem. On the other hand, we arbitrarily limited the extent of the plastic zone. Outside the plastic zone, a static shear stress concentration persisted which was nearly as large as that of the elastic case; had the plastic zone been larger, more plastic strain would have occurred, resulting in an even larger seismic moment.

IV.   COMPARISON OF ANALYTICAL AND FINITE DIFFERENCE
MODELS

4.1   INTRODUCTION

In Section II we developed a model for the Pocatello
Valley earthquake which is expressed in terms of the analyti-
cal relaxation model of Archambeau (1968) and Minster (1973).
This analytical model is convenient to use because it is ex-
pressed in terms of relatively few parameters. However,
interpretation of these parameters in terms of earthquake
physics is quite controversial because of the geometry in
which the source model is formulated. The Archambeau/Minster
source is a spherical volume of reduced shear strength which
grows in a pure shear prestress field. The growth is asym-
metric with a point on the boundary being fixed as shown below.

L
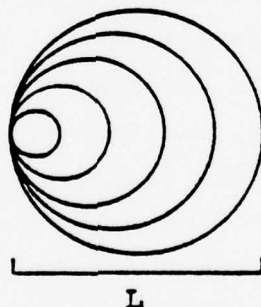
This model does include directionalized rupture, finite source
dimension and finite rupture velocity effects, but in a geometry
unlike conventional ideas of earthquake geometries.

The ILLIAC calculations of earthquake faulting are close
to the most detailed and realistic models of earthquake fault-
ing that are currently available. The disadvantage of using
such calculations to model a particular earthquake is, of
course, the expense of varying the parameters. The parameters
for our two calculations are not entirely fixed, however, be-
cause the fault dimension and stress drop can be scaled.

84

Taken together, the analytic models and the ILLIAC calculations can be used to define the earthquake source with considerable confidence. Questions about the physical significance of parameters of the analytical model can be resolved by comparing to the numerical model results.

In this section we compare the analytical model for the Pocatello Valley earthquake from Section II with the finite difference model. The implications of this comparison for the Pocatello Valley event and for western U.S. earthquakes in general will also be discussed.

4.2   SCALING THE FINITE DIFFERENCE MODEL

In Section 3.3 we listed the parameters for the two ILLIAC earthquake calculations. For the elastic case all parameters could be nondimensionalized and the results could have been presented in that form. The elastoplastic fault zone calculation is not so easily scaled and so we presented all our results in terms of specific parameters.

For the elastic problem, the fundamental parameters are the aspect ratio of the fault (in this case, it is square), Poisson's ratio (0.25), and the ratio V_R/β (in this case 0.9). If these dimensionless parameters are held fixed, the ordinate and abscissa of the far-field displacement spectrum can be scaled with fault dimension a, stress drop $\Delta\sigma$, shear modulus μ, shear speed β, and hypocentral distance r. A nondimensional frequency f' and nondimensional moment M_o' have the form

$$f' = \frac{fa}{\beta}$$

$$(28)$$

$$M_o' = \frac{M_o}{\Delta\sigma a^3}$$

Thus, the far-field spectral displacement scales as $a^3\Delta\sigma/\mu\beta r$ and frequency scales as β/a.

85

The wave velocity parameters α and β and the shear modulus μ are appropriate for the source region of the Pocatello Valley earthquake and, in fact, for a majority of the shallow western U.S. earthquakes. Therefore, we leave these parameters fixed. The rupture velocity is then fixed to be $V_R = 3.08$ km/sec or 0.9β. The parameters we are free to scale are the fault dimension, a, and the stress drop, $\Delta\sigma$.

In order to compare to data, we might wish, for example, to scale the corner frequency without modifying the long period spectral level (the seismic moment). To change the corner frequency by a factor q, we would replace the source dimension a by a/q and replace the stress drop $\Delta\sigma$ by $\Delta\sigma/q^3$. Similarly, to multiply the moment by a factor of q without modifying the corner frequency, we would replace $\Delta\sigma$ with $q\Delta\sigma$, and leave the source dimension a unchanged.

The elastoplastic source is not so easily scaled. Stress drop scaling can only be approximate. Zones that almost yield for one stress drop will yield for a higher stress drop. On the other hand, lowering the stress drop will remove yielding from some zones. It is not known how large an effect this is. However, we note that the stress drop scaling is generally by a large factor since it is proportional to the cube of the length scaling.

What about the length scaling of the elastoplastic case? We can scale exactly with length according to (28) as long as the answers are independent of the size of the plastic zone. That is, if the stresses outside the plastic zone are everywhere less than the yield condition. However, as discussed in Section 3.7.2, the displacement field for this elastoplastic calculation is dependent on the dimensions of the plastic zone. The quantitative extent of this dependence is, however, not known.

There is some difficulty in obtaining a suitable definition of $\Delta\sigma$. The quantity $\sigma_T - \sigma_f$, the difference between tectonic and frictional shear stress, is a well-defined physical parameter in our fault model. However, we would prefer to define $\Delta\sigma$ to represent a static stress drop, since it would then be comparable to the parameter appearing in the analytic fault model. The static stress drop is a well-defined quantity at a given location on the fault plane, namely the difference between the initial and final shear stress. However, this quantity is not a constant, but varies with position on the fault (see Figure 16). Nor is the spatial average of the static stress drop necessarily a meaningful quantity, since a large static stress concentration over a small area can greatly affect this average, with minimal effect on the radiated field. Instead, we shall define $\Delta\sigma$ to be 1.14 $(\sigma_T - \sigma_f)$; this choice of $\Delta\sigma$ gives the correct value of seismic moment when the average slip is estimated from Equation (24) and then the moment obtained from Equation (25) (see Section 3.5.3). With this definition, $\Delta\sigma$ for the elastic finite difference model is 205 bars. We note that the actual static stress drop on the fault varies fairly smoothly; it is 1.29 $(\sigma_T - \sigma_f)$ at the center, decreasing to approximately 1.1 $(\sigma_T - \sigma_f)$ at a distance of 2a/3 from the center, with little azimuthal variation.

4.3 ELASTIC FINITE DIFFERENCE SOURCE COMPARED TO OBSERVATIONS OF THE POCATELLO VALLEY EARTHQUAKE

Bache and Harkrider (1976) describe a technique for representing the output of finite difference source calculations like those in Section III in terms of a multipolar expansion. This technique is summarized in Section 3.4. Once we have computed the expansion coefficients, the multipole coefficients, in the source coordinate system, the coordinate rotation formulae given by Minster (1976) can be used to rotate the source to any desired orientation.

The Archambeau/Minster source used in Section II to develop the analytical model for the Pocatello Valley earthquake is expressed directly in terms of multipole coefficients. Thus, both sources can be represented in the same way and direct comparison is facilitated. Synthetic seismograms are computed using the methods and earth models described in Section 2.4.

The long period body wave seismograms for the finite difference sources are essentially identical to those shown in Figure 7. For these data the only important source parameters are the moment, focal depth and orientation.

Recall from Section 3.5.3 that the moment for the elastic finite difference calculation with the parameters given in Section 3.3 is 2.28×10^{24} dyne-cm. The moment for the Pocatello Valley earthquake inferred from the long period body waves is 7.0×10^{24} dyne-cm. Thus, we need to scale the calculation to a moment that is larger by a factor of 3.1.

The most straightforward way to scale the elastic finite difference source to the moment of the Pocatello Valley event is to increase the stress drop from 205 bars to 630 bars. Let us do so and explore the consequences for the short period seismograms.

In Figure 22 we add the short period seismograms for the elastic finite difference source with $\Delta\sigma = 630$ bars to Figure 8 from Section II. The waveforms and frequency content are rather close to those for Model I, the analytical source with a fault length of 3 km. The main difference is that for the finite difference source the P phase is larger relative to the pP phase. This is a consequence of the bilateral nature of the finite difference source, as we shall see.

The Archambeau/Minster analytical model can be modified to approximate bilateral faulting. We do so by

88

Dist.	33.4	50.4	51.5	56.6	72.5
Azm.	9	17.3	25.5	133.3	50.2
Sta.	RES	DAG	KTG	BOG	PTO

MODEL I

MODEL II
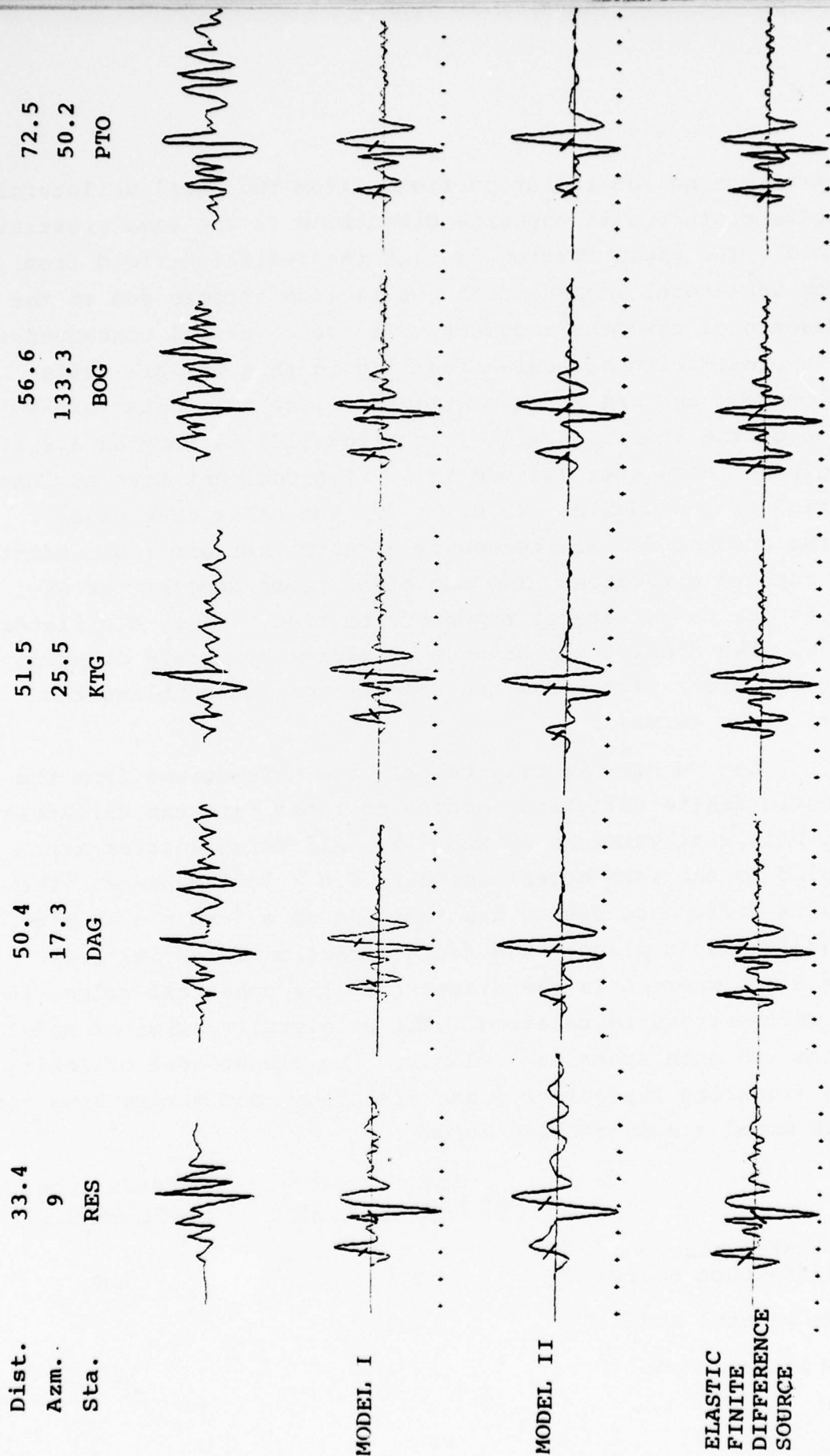
ELASTIC
FINITE
DIFFERENCE
SOURCE

Figure 22. Short period seismograms from the elastic finite difference source are compared to the observations of the Pocatello Valley earthquake and the synthetic records from two analytical source models (Figure 8).

89

superimposing the radiation fields from two equal unilateral faults rupturing in opposite directions in the same prestrain field. The approximation is that the radiation field from each unilateral segment does not include effects due to the presence of the other segment. The mathematical consequences of approximating bilateral faulting in this way are quite elementary and are worth mentioning. The multipolar expansion of the radiation field, Equation (17) in Section 3.4.1, includes terms even and odd in ℓ. The dominant term at long period is the double-couple, $\ell = 2$. The other even order terms account for finite source effects that are independent of rupture direction. The odd order terms account for effects due to unilateral rupture direction. Thus, a unilateral model like Model I can be made bilateral by merely dropping the odd order terms from the calculation and doubling the even order terms.

Let us now directly compare the seismograms from the elastic finite difference source to those from the unilateral and bilateral versions of Model I. All three sources are scaled to the same moment which is 7.0×10^{24} dyne-cm. The finite difference source has faulting on a 3 km × 3 km rectangular fault plane. The fault dimension for Model I is $L = 3$ km, where L is the diameter of the spherical volume into which stress is released. The bilateral version of Model I has two such spherical volumes. The planar area of faulting (ignoring the out-of-plane dimension) and stress drop for each model are summarized below:

	Planar Area of Faulting (km^2)	Stress Drop, $\Delta\sigma$ (bars)
Elastic Finite Difference Source	9	630
Unilateral Model I	7.1	253
Bilateral Model I	14.1	127

A bilateral Archambeau/Minster model with a planar fault area of 9 km^2 would include two sections, each with L = 2.4 km. The stress drop which gives the same $\Delta\sigma$ L^3 as the bilateral Model I is 250 bars. A unilateral Archambeau/Minster model with a planar area of 9 km^2 has L = 3.4 km and $\Delta\sigma$ = 176 bars. These stress drops are factors of 2.5 and 3.6 times smaller than the stress drop associated with the rectangular fault. These factors compare to the value of 3.6 which scales the stress drop of the Archambeau/Minster model to that of a circular fault of the same planar area and same moment (Minster and Suteau, 1976).

In Figure 23 we compare the five short period tele-seisms from the elastic finite difference calculation to those from the unilateral and bilateral versions of Model I. The amplitude (corrected for period dependent instrument response) and period data from these synthetic seismograms are summarized in Table 7. The bilateral Model I is somewhat longer period than the elastic finite difference source, which is expected since it has larger source dimension. The closer agreement of the bilateral Model I with the finite difference source is most apparent in the ratio of pP to P phases, though this is more clear from the records in Figure 23 than from the numbers in the table.

Now let us return to the comparison of the seismograms from the finite difference source with the Pocatello Valley earthquake observations, Figure 22. In Table 8 we compare the amplitudes and periods in the same format used for Tables 5 and 6 in Section II. We see that we have precisely the same problem we had with Model I in Section II. That is, when the finite difference source is scaled to have the correct moment, the short period seismograms are too large by a factor of four or five.
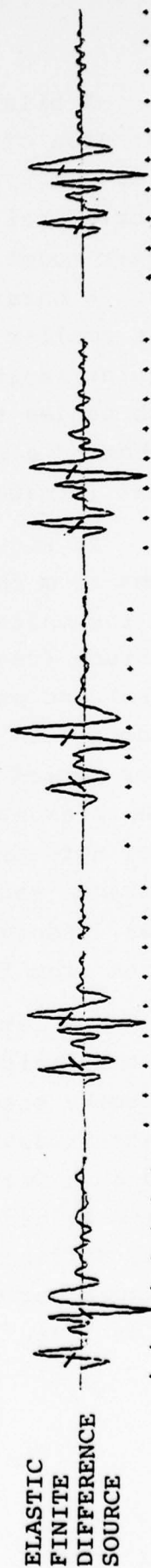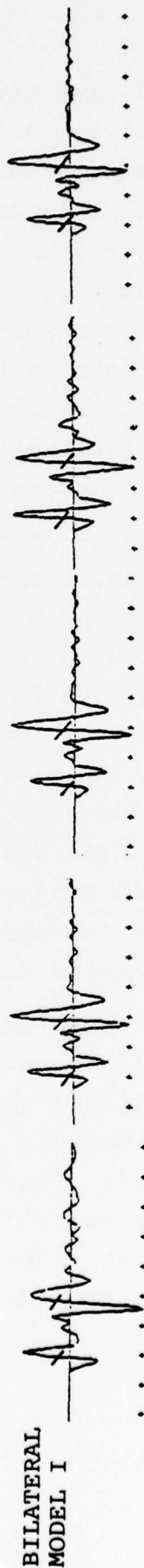
91
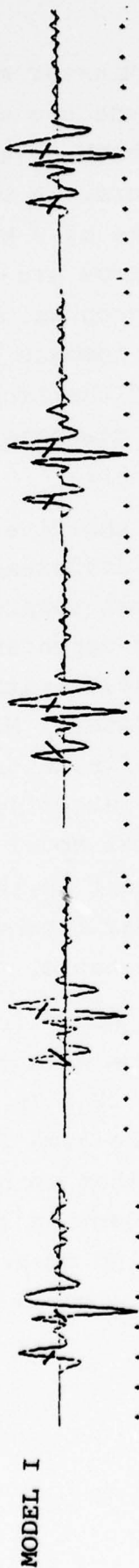
Figure 23. Comparison of synthetic seismograms from the elastic finite difference source to those from the unilateral and bilateral versions of Model I from Section II.

92

TABLE 7

AMPLITUDES AND PERIODS OF THE SEISMOGRAMS OF FIGURE 23

| STATIONS | P PHASE | | MAXIMUM PHASE | | |
	Amplitude (microns)	Period	Amplitude (microns)	Period	A_p/A_{max}
RES					
EFD Source*	2.11	1.1	2.59	1.0	1.23
Uni-Model I	1.80	1.2	2.33	1.0	1.29
Bi-Model I	1.84	1.3	1.96	1.2	1.07
DAG					
EFD Source	1.38	1.1	2.38	1.2	1.73
Uni-Model I	1.14	1.2	2.27	1.2	1.99
Bi-Model I	1.19	1.2	2.12	1.3	1.78
KTG					
EFD Source	1.29	1.1	2.42	1.2	1.88
Uni-Model I	1.07	1.2	2.37	1.2	2.22
Bi-Model I	1.11	1.2	2.24	1.3	2.02
BOG					
EFD Source	0.76	1.1	1.75	1.3	2.30
Uni-Model I	0.72	1.2	1.72	1.2	2.39
Bi-Model I	0.69	1.2	1.53	1.4	2.21
PTO					
EFD Source	0.67	1.1	1.96	1.3	2.93
Uni-Model I	0.72	1.3	2.02	1.3	2.81
Bi-Model I	0.61	1.2	1.88	1.4	3.08

*Elastic Finite Difference Source Model

TABLE 8

**AMPLITUDE AND PERIOD COMPARISONS FOR THE ELASTIC FINITE
DIFFERENCE SOURCE SEISMOGRAMS IN FIGURE 22**

Station	P PHASE		MAXIMUM AMPLITUDE	
	Amplitude Ratio A_O/A_S	Periods T_O/T_S	Amplitude Ratio A_O/A_S	Periods T_O/T_S
RES	0.06	1.2/1.1	0.15	1.3/1.0
DAG	0.07	1.1/1.1	0.20	1.3/1.2
KTG	0.15	1.1/1.1	0.33	1.2/1.3
BOG	0.35	1.4/1.1	0.33	1.2/1.3
PTO	0.20	1.4/1.1	0.18	1.2/1.0
Logarithmic Mean	0.13		0.22	
Standard Deviation	106%		41%	

Can the finite difference source be scaled to have less high frequency energy while retaining the same moment? The appropriate scaling relations are described in Section 4.2. Let us consider three earthquake sources:

1. $a = 1.5$ km, $\Delta\sigma = 630$ bars;

2. $a = 2.25$ km, $\Delta\sigma = 187$ bars;

3. $a = 3$ km, $\Delta\sigma = 79$ bars.

The first is the elastic finite difference source with the original fault dimension (a is defined in Figure 12). The far-field displacement spectra for this source appear in Figure 20. The second and third sources have the same spectra except that the frequency axis is scaled by 1.5 and 2.0, respectively. That is, the corner frequency moves to lower frequency. All three sources have the same moment.

In Figure 24 we compare the seismograms at Station KTG for these three source models. The amplitude and period data from these seismograms are compared in Table 9. We see that the effect of moving the corner frequency to lower frequency is quite large on the period. However, the short period amplitudes do not get much smaller!

In Figure 25 we compare the seismograms at all five stations for the first and third models. The amplitude and period data are compared in Table 10. At all stations we see that the measured periods are 0.4-0.8 seconds longer for the larger source dimension fault. However, the amplitudes (after correction for frequency dependent instrument response) are not much different for the two sources.

The results of this scaling of the elastic finite difference source support our conclusions about earthquake faulting reached earlier for the San Fernando (Bache and Barker, 1978) and Pocatello Valley (Section II) earthquakes following our analysis with the analytical Archambeau/Minster model.

95

a = 1.5 km, $\Delta\sigma$ = 630
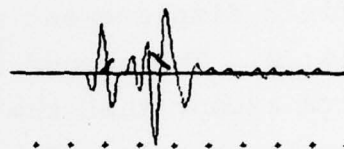
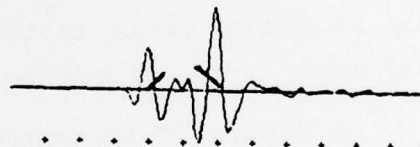a = 2.25, $\Delta\sigma$ = 187
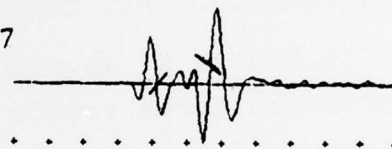
a = 3, $\Delta\sigma$ = 79

Figure 24. Synthetic seismograms are compared at Station KTG
for the elastic finite difference source scaled to
three source dimensions with the source moment
held constant.

TABLE 9

AMPLITUDE AND PERIOD DATA FOR SEISMOGRAMS AT KTG FOR THREE
SCALED VERSIONS OF THE FINITE DIFFERENCE SOURCE (FIGURE 24)

Source	P PHASE		MAXIMUM PHASE	
	Amplitude (microns)	Period (seconds)	Amplitude (microns)	Period (seconds)
$a = 1.5$, $\Delta\sigma = 630$	1.29	1.15	2.42	1.21
$a = 2.25$, $\Delta\sigma = 187$	1.04	1.30	2.21	1.41
$a = 3$, $\Delta\sigma = 79$	0.95	1.56	2.55	1.79

97

DIST.	33.4	50.4	51.5	56.6	72.5
AZM.	9	17.3	25.5	133.3	50.2
STA.	RES	DAG	KTG	BOG	PTO

OBSERVATIONS

a = 1.5,
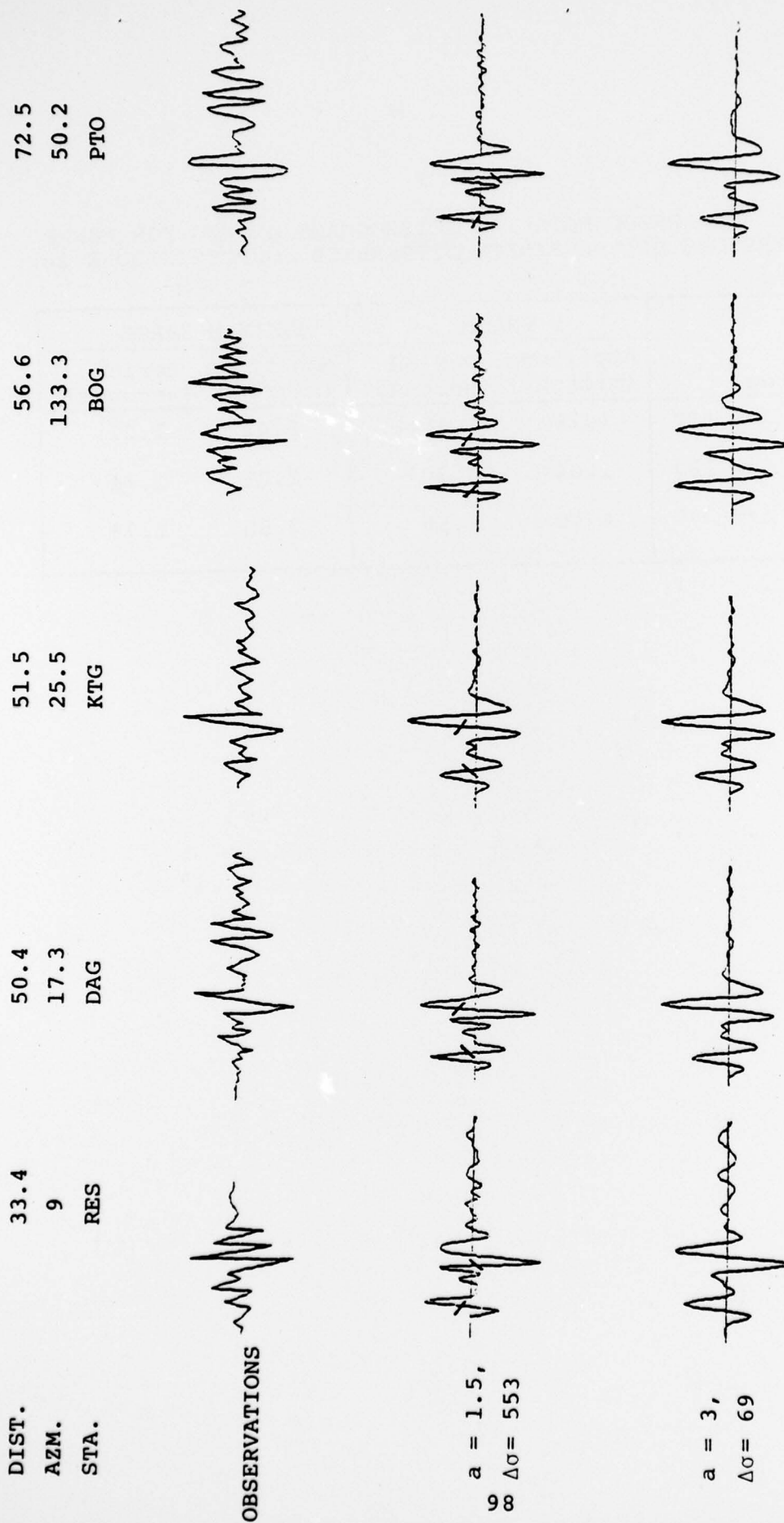Δσ = 553

a = 3,
Δσ = 69

98

Figure 25. The synthetic seismograms from the elastic finite difference source are
compared to the Pocatello Valley observations after scaling to two fault
dimensions with the seismic moment held constant.

TABLE 10

AMPLITUDE AND PERIOD DATA FOR TWO SCALED VERSIONS OF THE
ELASTIC FINITE DIFFERENCE SOURCE (FIGURE 25)

STATIONS	P PHASE		MAXIMUM PHASE	
	Amplitude (microns)	Period (seconds)	Amplitude (microns)	Period (seconds)
RES				
a = 1.5	2.11	1.1	2.59	1.0
a = 3.0	1.55	1.7	1.78	1.7
DAG				
a = 1.5	1.38	1.1	2.38	1.2
a = 3.0	1.04	1.6	2.28	1.7
KTG				
a = 1.5	1.29	1.1	2.42	1.2
a = 3.0	0.95	1.6	2.55	1.8
BOG				
a = 1.5	0.76	1.1	1.75	1.3
a = 3.0	0.81	1.6	2.01	2.1
PTO				
a = 1.5	0.67	1.1	1.96	1.3
a = 3.0	0.50	1.5	2.19	1.9

That is, we cannot simultaneously match the long and short period data with a single rupture velocity/single stress drop source model. In the following section we will see what effect the inclusion of elastoplastic material behavior will have.

4.4 ELASTOPLASTIC FINITE DIFFERENCE SOURCE COMPARED TO OBSERVATIONS OF THE POCATELLO VALLEY EARTHQUAKE

In Section 3.7.2 we compared the far-field displacement spectra from the elastic and elastoplastic finite difference sources. The differences were that the elastoplastic source has larger moment and lower corner frequency. These differences make the elastoplastic source look much like the elastic source scaled to a larger source dimension, at least as far as the amplitude spectra are concerned. Let us now study the seismograms from the elastoplastic source.

The moment of the elastoplastic source as computed is 3.15×10^{24} dyne-cm. This is smaller than the moment of the Pocatello Valley earthquake by a factor of 2.2. We pointed out in Section 4.2 that the elastoplastic calculations can only be scaled approximately. But since comparison is easier if all the synthetic seismograms have the same moment, let us scale the stress drop to 451 bars, i.e., by a factor of 2.2. The scaled source spectra are probably not much different than we would have gotten if we had repeated the calculation with this new stress drop.

In Figure 26 we compare the observations with the synthetic seismograms from the elastic and elastoplastic source calculations with the original source dimension (a = 1.5 km). For the elastoplastic source the amplitudes and periods are compared to the observations in Table 10 in the usual format.

From the seismograms in Figure 26 and the data in Table 11, we see that the addition of elastoplasticity to the

100

DIST.	33.4	50.4	51.5	56.6	72.5
AZM.	9	17.3	25.5	133.3	50.2
STA.	RES	DAG	KTG	BOG	PTO

OBSERVATIONS

ELASTIC
FINITE
DIFFERENCE
SOURCE

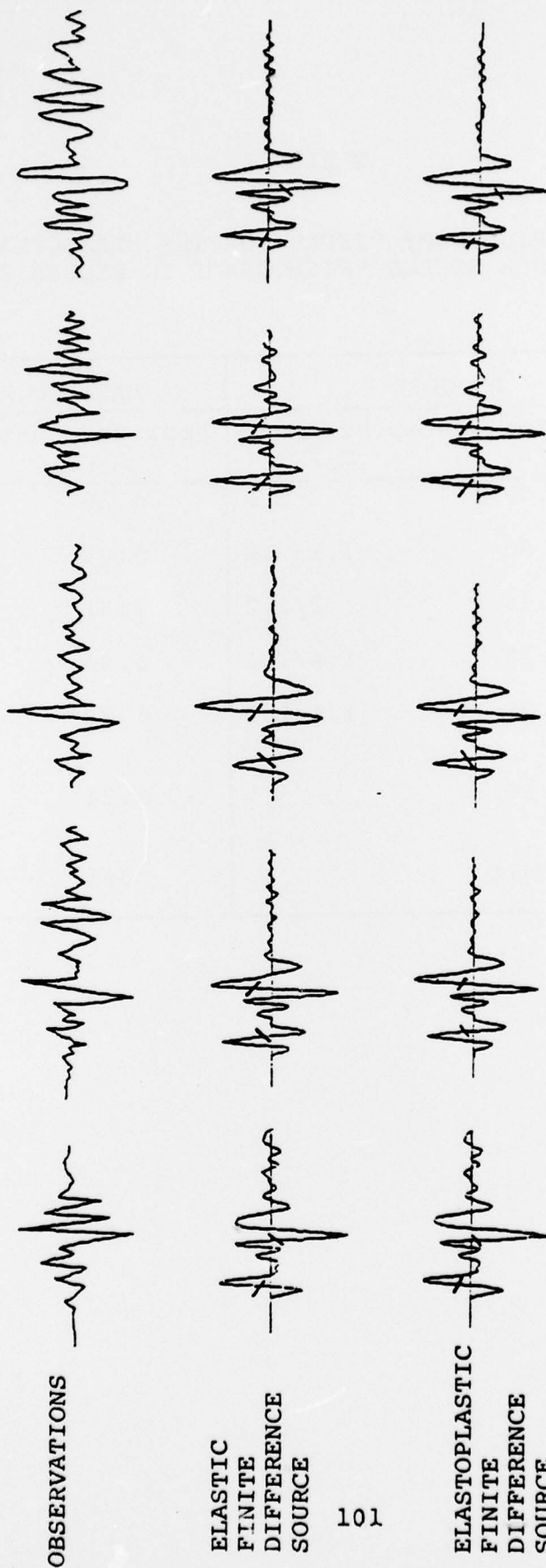ELASTOPLASTIC
FINITE
DIFFERENCE
SOURCE

Figure 26.   Seismograms from the two finite difference source calculations (scaled by stress drop to the correct moment) are compared to observations of the Pocatello Valley earthquake.

101

TABLE 11

AMPLITUDE AND PERIOD COMPARISONS FOR THE ELASTOPLASTIC FINITE
DIFFERENCE SOURCE SEISMOGRAMS IN FIGURE 26

Station	P PHASE		MAXIMUM AMPLITUDE	
	Amplitude Ratio A_O/A_S	Periods T_O/T_S	Amplitude Ratio A_O/A_S	Periods T_O/T_S
RES	0.07	1.2/1.2	0.16	1.3/1.1
DAG	0.07	1.1/1.2	0.21	1.3/1.3
KTG	0.16	1.2/1.2	0.31	1.3/1.3
BOG	0.36	1.4/1.1	0.36	1.2/1.3
PTO	0.21	1.4/1.1	0.20	1.2/1.0
Logarithmic Mean	0.14		0.24	
Standard Daviation	104%		39%	

model causes the dominant periods to be a bit larger, about 0.1 seconds in most cases. With the moment at the right level the synthetic short period seismograms are still too large by a factor of four or more.

4.5   CONCLUSIONS

The comparison of the analytical and finite difference models confirms our most important conclusion in Section II. The long and short perior data cannot be simultaneously fit with a single rupture velocity, single stress drop model. Variable rupture velocity, variable stress drop effects are important.

In this section we have studied two finite difference earthquake simulations. Since these are for simple events, they are not able to match the long and short period data simultaneously. When we scale them to the right moment, the short period radiation is too large by a factor of four or more.

Comparing seismograms from the analytical and finite difference models we see the importance of source directivity for matching the data. The finite difference sources are bilateral and give poorer agreement with the data than the unilateral analytical source.

Another important and interesting facet of the comparison is that it gives an opportunity to study the physical meaning of the parameters of the Archambeau/Minster model which is cast in terms of an unrealistic spherical geometry. The radiation pattern of P and S waves from the analytical model is not the same as from a planar carck, but the differences do not appear to be too important.

The physical meaning of the important parameter stress drop is made more clear after comparing the analytical and

103

finite difference models. We can scale the analytical model to have the same planar area as the finite difference fault plane. For the two models to have the same area, the stress drop for the analytical source is a factor of 2.5 (bilateral) or 3.6 (unilateral) times smaller than for the finite difference source. Thus, stress drops are underestimated by about this amount if they are based on the Archambeau/ Minster model. This confirms the stress drop estimate for the initial faulting of the Pocatello Valley event from Model II given at the end of Section II; that is, 162 bars.

V. ACKNOWLEDGEMENT

REFERENCES

Aki, K. (1968), "Seismic Displacements Near a Fault," J. Geophys. Res., Vol. 73, pp. 5359-5376.

Anderson, D. L. and R. S. Hart (1976), "An Earth Model Based on Free Oscillations and Body Waves," J. Geophys. Res., Vol. 81, pp. 1461-1475.

Arabasz, W. J., W. D. Richins and C. J. Langer (1975a), "Detailed Characteristics of March 1975 Idaho-Utah Border Earthquake Sequence," EOS, Vol. 56, p. 1022.

Arabasz, W. J., W. D. Richins, A. J. Katrinsky and R. E. Estill (1975b), "The Idaho-Utah Border (Pocatello Valley) Earthquake," University of Utah Preliminary Seismological Report.

Archambeau, C. B. (1968), "General Theory of Elastodynamic Source Fields," Rev. Geophys., Vol. 6, pp. 241-288.

Archuleta, R. J. (1976), "Experimental and Numerical Three-Dimensional Simulations of Strick-Slip Earthquakes," Ph.D. Dissertation, University of California, San Diego.

Archuleta, R. J. and G. A. Frazeri (1978), "Three-Dimensional Numerical Simulations of Dynamic Faulting in a Half-Space," Bull. Seism. Soc. Am., Vol. 68, pp. 541-572.

Archuleta, R. J. and J. N. Brune (1975), "Surface Strong Motion Associated with a Stick-Slip Event in a Foam Rubber Model of Earthquakes," Bull. Seism. Soc. Am., Vol. 65, pp. 1059-1071.

Bache, T. C. and T. G. Barker (1978), "The San Fernando Earthquake -- A Model Consistent with Near-Field and Far-Field Observations at Long and Short Periods," Systems, Science and Software Report SSS-R-78-3552, January.

Bache, T. C., J. T. Cherry, D. G. Lambert, J. F. Masso and J. M. Savino (1978), "A Deterministic Methodology for Discriminating Between Earthquakes and Underground Nuclear Explosions," Systems, Science and Software Report SSS-R-76-2925, July.

Bache, T. C. and D. G. Harkrider (1976), "The Body Waves Due to a General Seismic Source in a Layered Earth Model: 1. Formulation of the Theory," Bull. Seism. Soc. Am., Vol. 66, pp. 1805-1819.

Bache, T. C., J. T. Cherry, N. Rimer, J. M. Savino, T. R. Blake, T. G. Barker and D. G. Lambert (1975), "An Explanation of the Relative Amplitudes Generated by Explosions in Different Test Areas at NTS," Systems, Science and Software Final Report, DNA 3958F, October.

Battis, J. C. and K. J. Hill (1977), "Analysis of Seismicity and Tectonics of the Central and Western United States," Interim Scientific Report No. 1, Texas Instruments, Inc., April.

Bracewell, R. (1965), The Fourier Transform and Its Applications, McGraw-Hill, p. 279.

Brudick, L. J. (1978), "t* for S Waves with a Continental Ray Path," Bull. Seism. Soc. Am., Vol. 68, pp. 1013-1030.

Burridge, R. and L. Knopoff (1964), "Body Force Equivalent for Seismic Dislocation," Bull. Seism. Soc. Am., Vol. 54, pp. 1875-1888.

Cherry, J. T. (1977), "Users' Manual for the TRES Code," Systems, Science and Software Report SSS-R-77-3128, January.

Cherry, J. T., E. J. Halda and K. G. Hamilton (1976), "A Deterministic Approach to the Prediction of Free Field Ground Motion and Response Spectra from Stick-Slip Earthquakes," Earthquake Engineering and Structural Dynamics, Vol. 4, pp. 315-332.

Dahlen, F. A. (1974), "On the Ratio of P-Wave to S-Wave Corner Frequencies for Shallow Earthquake Sources," Bull. Seism. Soc. Am., Vol. 64, pp. 1159-1180.

Das, S. and K. Aki (1977), "A Numerical Study of Two-Dimensional Spontaneous Ruptuer Propagation," Geophys. J. R. Astr. Soc., Vol. 50, pp. 643-668.

Day, S. M. (1977), "Finite Element Analysis of Seismic Scattering Problems," Ph.D. Dissertation, University of California, San Diego.

Der, Z. and T. W. McElfresh (1977), "The Relationship Between Anelastic Attenuation and Regional Amplitude Anomalies of Short-Period P Waves in North America," Bull. Seism. Soc. Am., Vol. 67, pp. 1303-1317.

Haskell, N. A. (1964), "Total Energy and Energy Spectral Density of Elastic Wave Radiation from Propagating Faults," Bull. Seism. Soc. Am., Vol. 54, pp. 1811-1841.

Husseini, M. I., D. B. Jovanovich, M. J. Randall and L. B. Freund (1975), "The Fracture Energy of Earthquakes," *Geophys. J. R. Astr. Soc.*, Vol. 43, pp. 367-385.

Ida, Y. (1973), "The Maximum Acceleration of Seismic Ground Motion," *Bull. Seism. Soc. Am.*, Vol. 63, pp. 959-968.

Ida, Y. (1972), "Cohesive Force Across the Tip of a Longitudinal-Shear Crack and Griffith's Specific Surface Energy," *J. Geophys. Res.*, Vol. 77, pp. 3796-3805.

Keller, G. R., R. B. Smith and L. R. Braile (1975), "Crustal Structure Along the Great Basin-Colorado Plateau Transition from Seismic Refraction Profiling," *J. Geophys. Res.*, Vol. 80, pp. 1093-1098.

Kostrov, B. V. (1968), "The Inverse Problem of the Theory of Earthquake Foci," *Izv. Earth Physics*, Vol. 9, pp. 18-29.

Kostrov, B. V. (1964), "Self-Similar Problems of Propagation of Shear Cracks," *J. Appl. Math. Mech.*, Vol. 28, pp. 1077-1087.

Madariaga, R. (1976), "Dynamics of an Expanding Circular Fault," *Bull. Seism. Soc. Am.*, Vol. 66, pp. 639-666.

Minster, J. B. (1973), "Elastodynamics of Failure in a Continuum," Ph.D. Thesis, California Institute of Technology, Pasadena, California.

Minster, J. B. and A. M. Suteau (1977), "Far-Field Waveforms from an Arbitrarily Expanding Transparent Spherical Cavity in a Pre-Stressed Medium," *Geophys. Roy. Astr. Soc.*, Vol. 50, pp. 215-233.

Neuber, H. (1937), *Kerbspannungslehre*, Springer-Verlag, Berlin; Theory of Notch Stresses: Principles of Exact Calculation of Strength with Reference to Structural Form and Material, The Office of Tech. Info., AEC-TR-4547, 1958 (English Translation).

Richard, P. G. (1976), "Dynamic Motions Near an Earthquake Fault: A Three-Dimensional Solution," *Bull. Seism. Soc. Am.*, Vol. 66, pp. 1-32.

Rodi, W. L., T. G. Barker, T. C. Bache and H. J. Swanger (1979), "Synthesis of Regional Ground Motion from Western U.S. Earthquakes," Systems, Science and Software Final Contract Report to AFGL (in preparation).

Smith, R. B. and M. L. Sbar (1974), "Contemporary Tectonics and Seismicity of the Western United States with Emphasis on the Intermountain Seismic Belt," Geol. Soc. Am. Bull., Vol. 85, pp. 1205-1218.

Stewart, G. A. (1977), Personal Communication, California Institute of Technology, Pasadena, California.

Strick, E. (1970), "A Predicted Pedestal Effect for Pulse Propagation in Constant-Q Solids," Geophysics, Vol. 35, pp. 387-403.